

AEROACOUSTIC AND WAKE MEASUREMENTS ON A ROTATING  
CONTROLLED DIFFUSION BLADE

By

Behdad Davoudi

A THESIS

Submitted to  
Michigan State University  
in partial fulfillment of the requirements  
for the degree of

Mechanical Engineering – Master of Science

2014

## ABSTRACT

### AEROACOUSTIC AND WAKE MEASUREMENTS ON A ROTATING CONTROLLED DIFFUSION BLADE

By

Behdad Davoudi

Aeroacoustic and hot-wire wake measurements have been made for Rotating Controlled Diffusion Blades (RCDBs) configured as a 3 and a 9 blade axial fan. Six cases were identified for the three blade configuration based on its performance curve. Also, six cases corresponding to 6 distinct operating conditions: i) an attached flow, ii) a slightly separated flow, iii) deeply separated flow and three cases in the stall region have been selected for the nine blade configuration. These were examined using a detailed data acquisition program. The detailed results include the wake flow patterns and the associated noise radiation. Turbulence intensities and phase averaged velocity magnitudes have been obtained in the downstream region of the fan to represent the basic flow features for each defined case. A beamforming technique has been utilized to properly measure the radiated sound pressure level (SPL) created by the axial fan. Self-noise signatures of the propagated sound (auto-spectral density), corresponding to the defined cases, have been obtained in the range of 200-8000 Hz. Acoustic data and their links to: i) the physics of the flows, ii) aerodynamic loading and iii) fan rotational speed are presented. A semi-empirical model for trailing edge noise (a portion of the axial fan self-noise) was examined. Wake data (mean velocity and turbulence intensity downstream from the fan blades) were used as experimental inputs to these models. The experimental acoustic data and the semi-empirical results have been compared.

Copyright by  
BEHDAD DAVOUDI  
2014

To my mother and father, who are the reasons of any success and delight in my life  
To my wife Atra, who could not be more supportive and kind to me

## ACKNOWLEDGMENTS

I wish to extend my special thanks to my advisor, Professor John Foss and my committee members, Professors Abraham Engeda and Brian Feeny. Professor Foss has had a great deal of positive influence in my life. It was him who picked me to come to MSU for my Master's studies, and I have always enjoyed working with him and learning invaluable lessons in both Fluid Mechanics and English.

I would also like to thank Mrs. Jacqueline Foss who has been truly supportive from a family standpoint during the 20 month presence of me at MSU.

I have been really fortunate to have exceptional advice from Professor Scott Morris from the University of Notre Dame during this work. Without his unending contributions, this work would not have been possible. I am also thankful to Professor Ahmed Naguib of MSU who has always helped me by answering my questions.

My thanks to Dr. Douglas Neal who spent time discussing with me and teaching me valuable points. I also thank David Barrent, the current TSFL graduate student who provided the performance data presented in this work. Thank you to Alan Lawrenz, the TSFL research technician who has been a great help in constructing equipment and electronics as well as productive research discussions.

I also would like to express my appreciation to Brian Cobus, the undergraduate professorial assistant who has been really helpful in providing figures and editing of this document as well as a portion of data processing. Thanks to all folks and officials that have assisted me during these 20 months that I did not have room to mention their names.

# TABLE OF CONTENTS

LIST OF TABLES.....	viii
LIST OF FIGURES.....	ix
KEY TO SYMBOLS AND ABBREVIATIONS .....	xiii
1 INTRODUCTION.....	1
1.1 Motivation .....	1
1.2 The present investigation .....	1
1.3 Rotating Controlled Diffusion Blades (RCDB) characteristics .....	2
1.4 Aerodynamic sound.....	3
1.4.1 Non-rotating self-noise .....	3
1.4.2 Rotating self-noise .....	5
1.4.3 Lighthill analogy.....	7
1.5 Goody wall pressure model.....	9
1.6 Blake’s estimated radiated pressure for trailing edge sound source .....	10
1.7 Rotating flow field .....	13
2 EXPERIMENTAL EQUIPMENT AND PROCEDURE.....	17
2.1 Axial Fan Research and Development (AFRD) Facility description.....	17
2.2 AFRD modification.....	19
2.3 Fan description .....	20
2.4 Data acquisition.....	22
2.5 Wake measurements.....	23
2.5.1 Hot-wire calibration .....	25
2.6 Aeroacoustic measurements.....	28
2.6.1 Panasonic microphone development and calibration.....	28
2.6.2 Beamforming .....	36
3 EXPERIMENTAL RESULTS AND DISCUSSIONS.....	44
3.1 Performance curves .....	44
3.2 Wake results .....	48
3.2.1 9 blade fan.....	48
3.2.2 3 blade fan.....	56
3.3 Aeroacoustics results.....	62
3.3.1 9 blade fan.....	62
3.3.2 3 blade fan.....	69

3.4	Comparison between 9 and 3 blade fans .....	74
3.5	Semi-empirical acoustic model results.....	77
3.5.1	9 blade fan.....	77
3.5.2	3 blade fan.....	84
4	SUMMARY AND CONCLUSIONS .....	87
	APPENDICES.....	90
	Appendix A: Signal processing .....	91
	Appendix B: Convergence.....	92
	Appendix C: Fan “laws” .....	94
	Appendix D: Ambient noise concern.....	95
	Appendix E: Microphones technical specifications.....	97
	REFERENCES.....	99

## LIST OF TABLES

Table 1-1 Blade passing frequency values for target RPM conditions.....	6
Table 3-1 $\psi$ and $\varphi$ values of Case 1 through Case 6 - 3 and 9 blade fans.....	47
Table 3-2 Radial locations for hot-wire anemometry .....	53
Table 3-3 Wake thickness approximations – 9 blade fan .....	81
Table 3-4 Wake thickness approximations - 3 blade fan.....	85

## LIST OF FIGURES

Figure 1-1 Description of the laminar separation bubble on low-speed airfoils.....	3
Figure 1-2 Non-rotational airfoil self-noise .....	5
Figure 1-3 Geometry of a dipole source near a rigid half-plane.....	12
Figure 1-4 Flow geometry schematic .....	14
Figure 1-5 RCDB cross sections from hub to tip.....	16
Figure 2-1 The Axial Fan Research and Development (AFRD) Facility. ....	17
Figure 2-2 Driver motor and RPM sensor .....	18
Figure 2-3 a) Lead screw adjustment on the AFRD personnel door. b) Cover hatch location on the east wall of the AFRD facility. ....	20
Figure 2-4 Nine and three blade fan description.....	21
Figure 2-5 Data path schematic for both aeroacoustic and wake measurements .....	23
Figure 2-6 Schematic and image of Single probe hot-wire .....	24
Figure 2-7 Wake measurements setup (3 blade fan is shown).....	24
Figure 2-8 Trailing edge hot-wire location.....	25
Figure 2-9 Hot-wire calibration box schematic .....	27
Figure 2-10 TSFL hot-wire calibration facility .....	27
Figure 2-11 a) Panasonic microphone – front and back view. b) A hanging microphone .....	28
Figure 2-12 Microphone calibration schematic .....	29
Figure 2-13 Panasonic calibration setup.....	30
Figure 2-14 Coherence function for Panasonic microphone # 8 .....	31
Figure 2-15 Calibration procedure.....	32

Figure 2-16 The Volt-to-Pascal transfer functions of a representative microphones .....	33
Figure 2-17 Phase delay between Panasonic microphones and LD reference mic.....	34
Figure 2-18 ASD Comparison between the calibrated and uncelebrated Panasonic mic and LD reference mic.....	35
Figure 2-19 Schematic of circle arrays above the fan plane. a) top view, b) side view .....	37
Figure 2-20 Beamforming technique description .....	38
Figure 2-21 Photo of microphones arrays measurement setup .....	41
Figure 2-22 Acoustic measurements and data processing schematic .....	42
Figure 3-1 Non-dimensional performance curves - 9 blade Fan. ....	45
Figure 3-2 Non-dimensional performance curves - 3 blade Fan. ....	46
Figure 3-3 Phase averaged mean velocity, Case 1 - 9 blade fan.....	49
Figure 3-4 Phase averaged mean velocity, Case 2 - 9 blade fan.....	50
Figure 3-5 Phase averaged mean velocity, Case 3 - 9 blade fan.....	50
Figure 3-6 Phase averaged mean velocity, Case 4 - 9 blade fan.....	51
Figure 3-7 Phase averaged mean velocity, Case 5 - 9 blade fan.....	51
Figure 3-8 Phase averaged mean velocity, Case 6 - 9 blade fan.....	52
Figure 3-9 Incidence angles for different span locations - 9 blade fan.....	54
Figure 3-10 Turbulence intensity contours, Case 1 through Case 6 - 9 blade fan .....	55
Figure 3-11 Incidence angle - 3 blade fan .....	57
Figure 3-12 Phase averaged mean velocity, Case 1 - 3 blade fan.....	57
Figure 3-13 Phase averaged mean velocity, Case 2 - 3 blade fan.....	58
Figure 3-14 Phase averaged mean velocity, Case 3 - 3 blade fan.....	58
Figure 3-15 Phase averaged mean velocity, Case 4 - 3 blade fan.....	59

Figure 3-16 Phase averaged mean velocity, Case 5 - 3 blade fan.....	59
Figure 3-17 Phase averaged mean velocity, Case 6 - 3 blade fan.....	60
Figure 3-18 Turbulence intensity contours, Case 1 through Case 6 - 3 blade fan.....	61
Figure 3-19 ASDs for Case 1 - 9 blade fan.....	63
Figure 3-20 ASDs for Case 2 - 9 blade fan.....	64
Figure 3-21 ASDs for Case 3 - 9 blade fan.....	64
Figure 3-22 ASDs for Case 4 - 9 blade fan.....	65
Figure 3-23 ASDs for Case 6 - 9 blade fan.....	65
Figure 3-24 ASDs for Case 5 - 9 blade fan.....	66
Figure 3-25 ASDs for Case 1 with normalized abscissa - 9 blade fan .....	67
Figure 3-26 ASDs for Case 2 with normalized abscissa - 9 blade fan .....	67
Figure 3-27 ASDs for Case 3 with normalized abscissa - 9 blade fan .....	68
Figure 3-28 SPLs vs flow coefficient - 9 blade fan. ....	69
Figure 3-29 ASDs for Case 1 - 3 blade fan.....	70
Figure 3-30 ASDs for Case 2 - 3 blade fan.....	70
Figure 3-31 ASDs for Case 3 - 3 blade fan.....	71
Figure 3-32 ASDs for Case 4 - 3 blade fan.....	71
Figure 3-33 ASDs for Case 5 - 3 blade fan.....	72
Figure 3-34 ASDs for Case 6 - 3 blade fan.....	72
Figure 3-35 SPLs vs flow coefficient - 3 blade fan .....	73
Figure 3-36 ASD for Case 1 through Case 6 at 1000 RPM - 9 blade fan.....	75
Figure 3-37 ASD for Case 1 through Case 6 at 1000 RPM - 3 blade fan.....	75
Figure 3-38 Turbulence intensity of the second blade wake region, $r/r_{tip} = 0.707$ - 9 blade fan	79

Figure 3-39 Turbulence intensity of the second blade wake region, $r/r_{tip} = 0.77$ - 9 blade fan ..	79
Figure 3-40 Turbulence intensity of the second blade wake region, $r/r_{tip} = 0.83$ - 9 blade fan ..	80
Figure 3-41 Turbulence intensity of the second blade wake region, $r/r_{tip} = 0.89$ - 9 blade fan ..	80
Figure 3-42 Turbulence intensity of the second blade wake region, $r/r_{tip} = 0.96$ - 9 blade fan ..	81
Figure 3-43 Semi-empirical results vs experiment, Case 1- 9 blade fan .....	82
Figure 3-44 Semi-empirical results vs experiment, Case 2 - 9 blade fan .....	83
Figure 3-45 Semi-empirical results vs experiment, Case 3 - 9 blade fan .....	83
Figure 3-46 Turbulence intensity in the wake region of the first blade, Cases 1 - 3 blade fan .....	84
Figure 3-47 Semi-empirical results vs experiment, Cases 1- 3 blade fan.....	85
Figure B-1 Convergence history of $\langle V(\theta) \rangle$ at 1000 RPM - 9 blade fan.....	94
Figure D-1 Lab ambient noise.....	96
Figure E-1 Larson Davis manufacture specifications.....	98
Figure E-2 Panasonic manufacture specifications.....	99

## KEY TO SYMBOLS AND ABBREVIATIONS

### Notations

$[\ ]^*$ .....	Complex Conjugate of the $[\ ]$
$E\{ \}$ .....	Ensemble average of quantity $\{ \}$
$\langle \rangle$ .....	Phase-averaged of $\langle \rangle$
$\bar{[\ ]}$ .....	Time average of $[\ ]$
$[\ ]_{rms}$ .....	Root mean squared of $[\ ]$
$[\ ]_0$ .....	Reference value for $[\ ]$
$[\ ]_m$ .....	measured value of $[\ ]$
$[\ ]_t$ .....	Target value of $[\ ]$

### Abbreviations

AFRD.....	Axial Flow Research and Development
ASD.....	Auto Spectral Density
CDB.....	Controlled Diffusion Blade
CSD.....	Cross Spectral density
LD.....	Larson Davis reference microphone
LE.....	Leading Edge
Pana.....	Panasonic
PS.....	Pressure Side
RCDB.....	Rotating Controlled Diffusion Blade
SS.....	Suction Side

TE..... Trailing Edge

### **Roman symbols**

a, b..... random signal

$A$ .....Annulus area between the hub and outer shroud

$A_1$ .....Pre-calibration coefficient for a hot-wire sensor, see Eq. 2.3

$B$ .....Number of blades

$B_1$ .....Pre-calibration coefficient for a hot-wire sensor, see Eq. 2.3

$BPF$ .....Blade passing frequency (Hz), see Eq. 1.1

$c_0$ .....Sound speed

$C$ ..... Blade Chord length, see Fig. 1.4

$d$ ..... Panasonic microphone diameter

$D_H$ ..... Hub diameter

$D_S$ .....Shroud diameter

$drift_{1-2}$ .....Hot-wire calibration drift, see Eq. 2.4

$E_1$ .....Hot-wire output voltage in pre-calibration, see Eq. 2.3

$E_2$ .....Hot-wire output voltage in post-calibration, see Eq. 2.4

$f$ ..... Frequency

$FFT(a)$ ..... Fast Fourier Transform applied on signal “a”

$f_s$ ..... Sampling frequency

$H$ ..... Shape factor

$j$ ..... index number

$L$ .....Height differential between upper and lower arrays, see Fig. 2.18

$L_3$ ..... Blade span, see Fig. 1.3

$\dot{m}$ .....	Mass flow rate
$M$ .....	Number of data points to be inserted in FFT
$M_c$ .....	Convective Mach number
$mic(j)$ .....	Signal of Panasonic microphone # “j”, see Eq. 2.10
$mic_{shifted}(j)$ .....	Shifted Signal of Panasonic microphone # “j”, see Eq. 2.10
$N$ .....	Sample size
$N_r$ .....	Number of revolutions
$n_1$ .....	Pre-calibration coefficient for a hot-wire sensor, see Eq. 2.3
$n_d$ .....	Number of the data blocks, see Eq. A.2
$N_d$ .....	Sample delay, see Eq. A.3
$p$ .....	Pressure
$P_{atm}$ .....	Atmospheric pressure
$P_R$ .....	Reservoir pressure, see Fig. 2.1
$r_{obs}$ .....	Distance of an observer to the trailing edge, see Fig. 1.3
$r$ .....	Radial direction
$r_{root}, r_{mid}, r_{tip}$ .....	Blade hub, mid-span, tip radius
$R$ .....	Specific gas constant
$R_{ab}$ .....	Cross-correlation function between “a” and “b”, see Eq. A.3
$Re_C$ .....	Reynolds number based on the blade chord = $W_\infty C/\nu = U_\infty C/\nu$
$Re_{\delta^{**}}$ .....	Momentum Reynolds number = $U_e \delta^{**}/\nu$
$R_T$ .....	Inner-layer to outer layer time scale, see Eq. 1.13
$S1, S2, S3$ .....	Direction of lateral sound sources 1, 2 and 3, see Fig. 2.20

$t_{delay-lateral}$ ..... Lateral time delay between a pair of microphone, see Eq. 2.8  
 $t_{delay-vertical}$ .....Vertical time delay between a pair of microphone  
 $T$ .....Temperature [ $^{\circ}K$ ]  
 $T_{ij}$ .....Lighthill Tensor, see Eq. 1.11  
 $TF_{avg}$ .....Averaged transfer function over frequency, see Eq. 2.7  
 $TF(f)$ .....Transfer function, see Eq. 2.6  
 $U$ .....Uniform background velocity  
 $\bar{U}$ ..... Spatially and temporally mean axial velocity  
 $U_e$ .....Velocity at the boundary layer edge  
 $U_{\infty}$ ..... Incidence velocity (for stationary airfoils)  
 $u_{\tau}$ ..... Friction velocity  
 $u_i', v_i', v'$ ..... Velocity fluctuations  
 $V$ .....Velocity magnitude  
 $\overrightarrow{V_{a/b}}$ .....Velocity of the air w.r.t. blade, see Eq. 1.20  
 $\overrightarrow{V_{b/g}}$ .....Velocity of the blade w.r.t. ground, see Eq. 1.20  
 $\overrightarrow{V_{a/g}}$ .....Velocity of the air w.r.t. ground, see Eq. 1.20  
 $V_{cal}$ .....Hot-wire calibration velocity, see Eq. 2.2  
 $V_{tip}$ .....Blade tip velocity  
 $W_{\infty}$ .....Incidence velocity (for rotating airfoils)  
 $w(M)$ .....Hanning function for M data points, see Eqs. A.1-2  
 $x_1, x_2, x_3$  or  $x, y, z$ .....Cartesian coordinates

## GREEK SYMBOLS

$\alpha_1$ .....	Angle between the stream-wise direction and $r_{sin} \alpha_2$ , see Fig. 1.3
$\alpha_2$ .....	Angle between the span-wise direction and $r_{obs}$ , see Fig. 1.3
$\alpha_g$ .....	Geometric angle of attack, see Fig. 1.4
$\alpha_i$ .....	Incidence angle, see Fig. 1.4
$\gamma$ .....	Ratio of specific heats (adiabatic index)
$\gamma_{ab}^2$ .....	Coherence between signal “a” and “b”, see Eq. 2.5
$\delta$ .....	Boundary layer thickness
$\delta^*$ .....	Displacement Thickness
$\delta^{**}$ .....	Boundary layer momentum thickness
$\Delta x'$ .....	Lateral distance, see Eq. 2.8
$\Delta P$ .....	Pressure differential across the fan = $P_R - P_{atm}$
$\theta$ .....	Spatial phase
$\Theta$ .....	Angle between $S1$ and $S2$ , see Fig. 2.20
$\Lambda_3$ .....	Frequency dependent Spanwise integral length scale
$\nu$ .....	Kinematic viscosity of air
$\rho$ .....	Air density
$\sigma$ .....	Blade solidity, see Eq. 2.1
$\sigma_{ij}$ .....	Shear stress tensor, see Eq. 1.5
$\tau_w$ .....	Wall shear stress, see Eq. 1.14
$\phi$ .....	Flow coefficient, see Eq. 3.1
$\Phi_{P,rad}$ .....	Radiated acoustic auto spectral density
$\Phi_{PP}$ .....	Wall pressure auto spectral density, see Eq. 1.12

- $\Phi_{aa}$ .....Auto spectral density of signal “a”, see Eq. A.1
- $\Phi_{ab}$ .....Cross spectral density between signals “a” and “b”, see Eq. A.2
- $\Psi$ .....Head rise coefficient, see Eq. 3.1
- $\omega$ .....Angular frequency =  $2\pi f$
- $\Omega$ .....Rotational speed

# 1 INTRODUCTION

## 1.1 Motivation

Aeroacoustics have recently become an important aspect in engineering design. Engineers' concerns have grown over noise pollution in the industrial contemporary world. The objective is to make mechanically efficient and acoustically quiet equipment. One of the important sound sources is present when there is a Fluid-Structure Interaction (FSI). Trailing edge noise is an example of this source. Specific examples include: i) a helicopter blade-vortex interaction (Ilie, 2009) and ii) a wind turbine (Hubbard & Shepherd, 1991). There are numerous applications where the flow-induced noise has an important contribution in noise production such as fans, compressors, vehicle side mirrors (Morris *et al*, 2007) and HVAC systems (Leite *et al*, 2009). For example, in some cases the noise level produced by cooling fan even exceeds the engine noise level (Cudina, 2001). The flow-induced noise indeed increases for larger and faster equipment. Thus, understanding the flow-induced noise is important in the efforts to reduce noise levels.

## 1.2 The present investigation

This research work has explored aeroacoustics and wake aspects of an axial fan for different operating conditions corresponding to distinct flow behaviors over the blades. Models studies of the aeroacoustics have been established using wake measurements in the region downstream from the fan. The axial fan is located in the Axial Flow Research and Development (AFRD) facility which will be discussed in detail in Chapter 2. The fan incorporates Controlled Diffusion

blades. This work follows the investigations carried out by Neal (2010) and Cawood (2012) on the rotating controlled diffusion blades (RCDB). Both of those investigators have worked on a three blade configuration.

Microphones, placed at some distance from the rotating blades were used for the aeroacoustic measurements in this investigation. The specific objective is to record the magnitudes and frequency content of the self-noise generated by the fan. This is a challenging problem in a non-anechoic environment. The beamforming technique, wherein the time delay between different microphone signals is used to recover the net sound produced in a given region of space, was used to represent the acoustic output from the fan plane. This technique is shown to be distinctly successful.

### **1.3 Rotating Controlled Diffusion Blades (RCDB) characteristics**

Controlled diffusion airfoils are a cambered type of airfoil. They are designed such that the flow remains attached over the suction side of the airfoil (Gelder et al., 1987) which is achieved by controlling boundary layer growth.

Laminar separation bubble phenomenon is another special characteristic of the RCDB that Neal (2010) has investigated. One can conclude that for a low Reynolds number based on the chord ( $Re_C = W_\infty C / \nu = U_\infty C / \nu < 500,000$ ), the laminar separation near the leading edge of RCDB can be expected provided that the airfoil is exposed to an appropriate incidence flow. (Longhouse, 1976). The flow reattachment will be accompanied with a turbulent flow (Lissaman, 1983), and flow is more likely (cf without laminar separation bubble) to remain attached over the entire suction side of the airfoil. That is, it will be attached to the trailing edge.

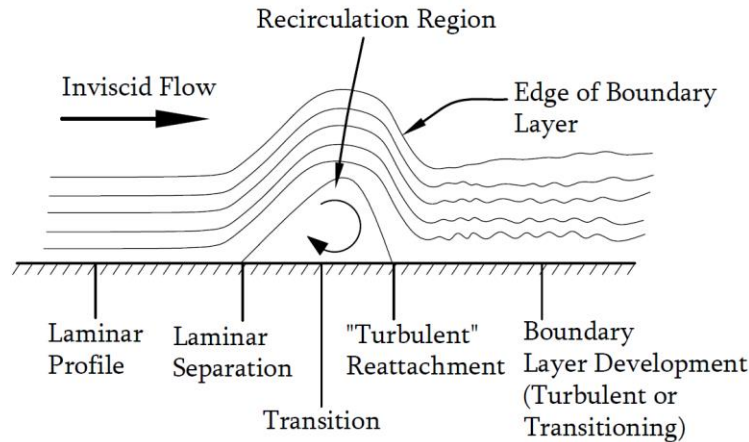


**Figure 1-1 Description of the laminar separation bubble on low-speed airfoils (Neal, 2010).**

Note: Vertical scale is exaggerated

The controlled diffusion blades studied here have a chord length of 133.9 mm, a 4% thickness-to-chord ratio and a camber angle of  $12^\circ$ . Blade shape is identical through the entire span length ( $L_3 = 126 \text{ mm}$ ).

## 1.4 Aerodynamic sound

### 1.4.1 Non-rotating self-noise

Brooks et al (1989) classified airfoil self-noise sources. He performed experiments on seven NACA 0012 airfoils of different sizes ( $2.5 < C < 61 \text{ cm}$ ) tested in a wind tunnel for  $Re_c < 3 \times 10^6$  and  $0 < \alpha_g < 25.2^\circ$ . His experiments covered all possible physics of flow around an airfoil for  $M_c < 0.5$ . As indicated in Fig. 1.2, he has classified the self-noise associated with airfoils as follows:

1. Turbulent boundary layer – trailing edge (TBL-TE) noise

At high Reynolds numbers ( $Re_c$ ), a turbulent boundary layer can develop over most of the span. The interaction of the developed turbulent flow and trailing edge generates noise. This mechanism is one of the most well-known and prominent in the field of

aeroacoustics. It is often modeled by a semi-empirical approach based on the surface pressure spectra. These models were, however, found to be inaccurate in terms of their capability to demonstrate correct trends with respect to angle of attack.

## 2. Separation stall noise

Flow separation causes considerable noise generation compared with TBL-TE noise. It is interesting to note that a mildly separated flow radiates sound from the TE (Paterson et al, 1974) due to shed vorticity of the turbulent flow, whereas deep stall radiates relatively low frequency noise from the whole suction side surface (Fink and Bailey, 1980).

## 3. Laminar boundary layer – vortex shedding noise

If a laminar boundary layer does not transition to a turbulent boundary layer before arriving at TE, the shed vorticity in relatively regular vortex motions occurs. The vortex shedding formation was found to be associated with an acoustic feedback from the origin of the acoustic waves at the TE to the point of the instability in the laminar boundary layer (Longhouse, 1977). This source type does not scale with velocity. According to Longhouse, the vortex shedding noise can occur with a negative incidence angle and a low Reynolds number based on the chord. It is instructive to note that laminar vortex shedding noise generation can be eliminated by transitioning to turbulent flow. For example, Longhouse used serrations located at the LE to trigger the desired transition. Similarly the use of a cambered airfoil as in the case of RCDB can eliminate the generation of this sound source by action of the LE region separation and re-attachment.

## 4. Trailing edge bluntness – Vortex shedding noise

This sound source is a relatively high-frequency broadband noise (Grosveld, 1984). This source can be important especially when the ratio of TE thickness to the boundary layer displacement thickness is large. For rotor blades or typical wings, this may not be an issue since the blades are thin at the TE.

#### 5. Tip vortex formation noise

A tip vortex is formed for a lifting surface when the flow from the pressure side transits to the suction side. Tip noise has been determined to be associated with turbulence in the local separated flow, and it has been identified as high-frequency source of noise.

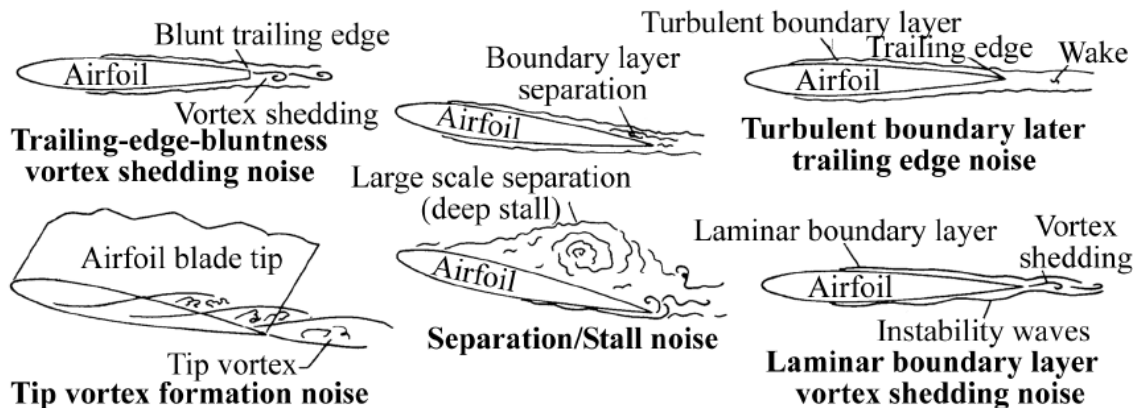


Figure 1-2 Non-rotational airfoil self-noise (Brooks et al. 1989).

Adopted from Cawood (2012)

#### 1.4.2 Rotating self-noise

Airfoil Self-noise mechanisms have been discussed in the previous section. When airfoils are configured next to each other i.e. in an axial fan or a compressor, another sound source will be present. This source of sound often occurs at integer multiples of the blade passing frequency of a fan, and it is gradually attenuated for higher frequencies. Blade passing frequency (BPF) is defined as:

$$BPF = \frac{\Omega B}{2\pi} \quad (1.1)$$

where,  $\Omega$  (*rad/sec*) is the fan rotational speed, and B is the number of blades.

This sound source is present because of the blades interaction with inflow distortion. (Longhouse, 1976). Stephens and Morris (2011) suggested that the blade passing noise might be because of either a sensitivity to the inflow distortion or a correlated unsteady lift caused by local potential fluctuations.

Table 1-1 provides blade passing frequency values (based on Eq. 1.1) for target RPM conditions:

**Table 1-1 Blade passing frequency values for target RPM conditions**

9 blade fan	RPM	437	540	600	710	900	1000
	BPF (HZ)	65	81	90	106.5	135	150
3 blade fan	RPM	540	600	655	710	930	1000
	BPF (Hz)	27	30	32	35.5	46.5	50

The natural frequency of the AFRD is understood to lie approximately between 700 to 900 RPM. Because of structural noise and vibration, data were not acquired for this range of rotational speed.

### 1.4.3 Lighthill analogy

Lighthill (1952) made a connection between Navier-Stokes and wave equations. If one starts with conservation of mass, and then subtracts the divergence of the momentum equation from the time derivative of conservation of mass, the Lighthill's acoustic analogy will be obtained. Note that in this derivation, the isotropic condition is assumed for acoustic pressure, that is:

$$P' = c_0^2 \rho' \quad (1.2)$$

Conservation of mass:

$$\frac{\partial \rho}{\partial t} + \frac{\partial}{\partial x_i} (\rho u_i) = 0 \quad (1.3)$$

Navier-Stokes equations:

$$\frac{\partial}{\partial t} (\rho u_i) + \frac{\partial}{\partial x_j} (\rho u_i u_j) = \frac{\partial}{\partial x_j} (-\delta_{ij} P + \sigma_{ij}) \quad (1.4)$$

In which,  $\sigma_{ij}$  is the viscous stress tensor and is defined as:

$$\sigma_{ij} = \mu \left( \frac{\partial u_i}{\partial x_j} + \frac{\partial u_j}{\partial x_i} - \frac{2}{3} \left( \frac{\partial u_k}{\partial x_k} \right) \delta_{ij} \right) \quad (1.5)$$

The derivation follows by taking the time derivative of the continuity equation:

$$\frac{\partial}{\partial t} (\text{cons. of Mass}) = \frac{\partial^2 \rho}{\partial t^2} + \frac{\partial}{\partial x_j} \left( \frac{\partial}{\partial t} (\rho u_j) \right) = 0 \quad (1.6)$$

And then, taking the divergence of the momentum equation results in:

$$\frac{\partial}{\partial x_i} \left( \frac{\partial}{\partial t} (\rho u_i) \right) + \frac{\partial^2}{\partial x_i \partial x_j} (\rho u_i u_j) = \frac{\partial^2}{\partial x_i \partial x_j} (-\delta_{ij} P + \sigma_{ij}) \quad (1.7)$$

Now, if one subtracts Eq. 1.6 from Eq. 1.7, the result would be:

$$\frac{\partial^2 \rho}{\partial t^2} - \frac{\partial^2}{\partial x_i \partial x_j} (\rho u_i u_j) = \frac{\partial^2}{\partial x_i \partial x_i} P + \frac{\partial^2}{\partial x_i \partial x_j} (-\sigma_{ij}) \quad (1.8)$$

Assuming  $p' = p - p_0$  and  $\rho' = \rho - \rho_0$ , and let null subscripts be mean quantities at large distance from the source flow (Howe, 2001). Subtracting the term  $C_0 \nabla^2 \rho'$  from both r.h.s. and l.h.s. leads to:

$$\frac{\partial^2 \rho'}{\partial t^2} - C_0 \nabla^2 \rho' = \frac{\partial^2}{\partial x_i \partial x_j} (\rho u_i u_j - \sigma_{ij} + (P' - C_0^2 \rho') \delta_{ij}) \quad (1.9)$$

$$T_{ij} = \rho u_i u_j - \sigma_{ij} + (p' - C_0^2 \rho') \delta_{ij} \quad (1.10)$$

$T_{ij}$  is the Lighthill tensor.

Eq. 1.9 is an exact hyperbolic partial differential equation. It describes a wave propagating at the speed of sound in a medium at rest. Fluctuating forces are externally applied in the form described by the r.h.s. of the equation.

As indicated by Khalighi (2010), if a spatially uniform background velocity  $U$  is assumed such that  $u = U + u'$ , Eq. 1.9 can be manipulated by substituting for  $u$ , and it will lead to the following equation for the Lighthill tensor:

$$T_{ij} = \rho u_i' u_j', -\sigma_{ij} + (\dot{P} - C_0^2 \dot{\rho}) \delta_{ij} \quad (1.11)$$

The first term is the Reynolds stress which is a predominant quantity in turbulent flows. In a fluid of uniform mean density, Lighthill showed that the principle source is a quadrupole type, and its strength is quantified by the Reynolds stress (Howe, 2001). Curle (1955) made an extension to Lighthill's analogy, and added a dipole term to the Lighthill's tensor to incorporate the effect of the solid boundaries on the generated sound. Later, Ffowcs Williams and Hawkings (1969) extended the Lighthill-Curle theory to include arbitrary convective motion. Howe (2001) also indicated that the monopole component of sound can be associated with an unsteady volume flux caused by an aerodynamic source. (A police siren is a good example of this acoustic source.)

## 1.5 Goody wall pressure model

Goody (2004) proposed an empirical model for surface pressure spectra underneath a turbulent boundary layer with zero pressure gradient. His model is basically a curve fit on several experimental results adopted from a large range of Reynolds number,  $1.4 \times 10^4 < Re_\theta < 2.34 \times 10^4$ . His model follows as:

$$\frac{\Phi_{pp}(\omega)U_e}{\tau_w^2} = \frac{3 \left(\frac{\omega\delta}{U_e}\right)^7}{\left[\left(\frac{\omega\delta}{U_e}\right)^{0.75} + 0.5\right]^{3.7} + \left[R_T^{-0.57}\left(\frac{\omega\delta}{U_e}\right)\right]^7} \quad (1.12)$$

In equation 1.12,  $\delta$  is the boundary layer thickness,  $U_e$  is the velocity at the edge of the boundary layer,  $\omega$  is the angular frequency, and  $\tau_w$  is the wall stress.  $R_T$  is the ratio of the timescales of the outer to inner boundary layer and is defined as:

$$R_T = \frac{\delta/U_e}{\nu/u_\tau^2} \quad (1.13)$$

where  $u_\tau$  is the friction velocity. It is worth to note that the time scale ratio also contains effect of Reynolds number (Goody, 2004).

Goody (2004) proposed  $R_T = 0.11(U_e \delta^{**}/\nu)$ . Spalart and Watmuff (1993) reported shape factors ( $H = \delta^*/\delta^{**}$ ) in the range  $1.5 < H < 1.65$  having obtained boundary layer measurements for low Reynolds number in the presence of an adverse pressure gradient.

Stephan and Morris (2011) assumed  $H=1.45$  and  $\delta^* = \delta/8$  as the general boundary layer characteristic of an axial ducted fan. As an estimation of the boundary layer spectra of a rotating blade, they suggested that  $U_e$  can be approximated with blade relative velocity ( $W_\infty$ ). They also assumed that the wall stress can be approximated with the maximum of the RMS of velocity fluctuations squared in the wake region of a blade. Namely:

$$\tau_w = \rho[\tilde{u}^2]_{max} \quad (1.14)$$

For axial fan applications, if one obtains the wake measurements the Goody model can be utilized to establish surface pressure spectra. It is noted that wake characteristics close to the trailing edge (TE) of a blade are essentially similar to the upstream boundary layer characteristics because of the upstream flow momentum.

## 1.6 Blake's estimated radiated pressure for trailing edge sound source

Blake (1986) has presented a self-noise prediction model for the flow passing over one side of a semi-infinite half plane (i. e., TE) as shown in Fig.1.3. His model accounts for turbulent

boundary layer – Trailing edge (TBL-TE) noise which is mainly represented by dipole sound sources. Basically, his model is for the unsteady lift based on the unsteady surface pressure in the boundary layer (Stephens and Morris, 2011). For the observer located at the distance “ $|r_{obs}|$ ” from the TE, the model provides the radiated pressure auto-spectra ( $\Phi_{P_{rad}}$ ) of a convecting flow passing over the TE. The predicted spectra is function of unsteady surface pressure spectra ( $\Phi_{PP}$ ), plane span ( $L_3$ ), observer location with respect to flow direction and TE, and other turbulence quantities. His model follows as:

$$[\Phi_{P_{rad}}(f)]_{edge} = \Phi_{PP}(f) \frac{1}{4\pi^2} \frac{L_3 \Lambda_3(f)}{|r_{obs}|^2} M_c \sin^2 \frac{\alpha_1}{2} |\sin \alpha_2| \quad f > \frac{c_0}{C} \quad (1.15)$$

where,  $M_c$  is the convective Mach number ( $M_c = U_c/c_0$ ).  $c_0$  is the sound velocity ( $c_0 = \sqrt{\gamma RT}$ ).  $\Lambda_3(f)$  is the span-wise integral length scale of the unsteady wall measure. Blake (1986) suggested  $\Lambda_3(f) = U_c/2\pi f$  as it is difficult to measure. He also suggested that  $U_c/U_\infty = 0.7$  and  $\gamma_3 = 0.7$ . Having these assumption, one can obtain  $\Lambda_3 = U_\infty/2\pi f$ . The angles  $\alpha_1$  and  $\alpha_2$  account for the observer position with respect to flow and TE directions. As shown in Fig. 1.3, The angle of  $\alpha_1$  is defined between the stream-wise direction and  $r \sin \alpha_2$ . The angle of  $\alpha_2$  is defined between the span-wise direction and  $r_{obs}$ .

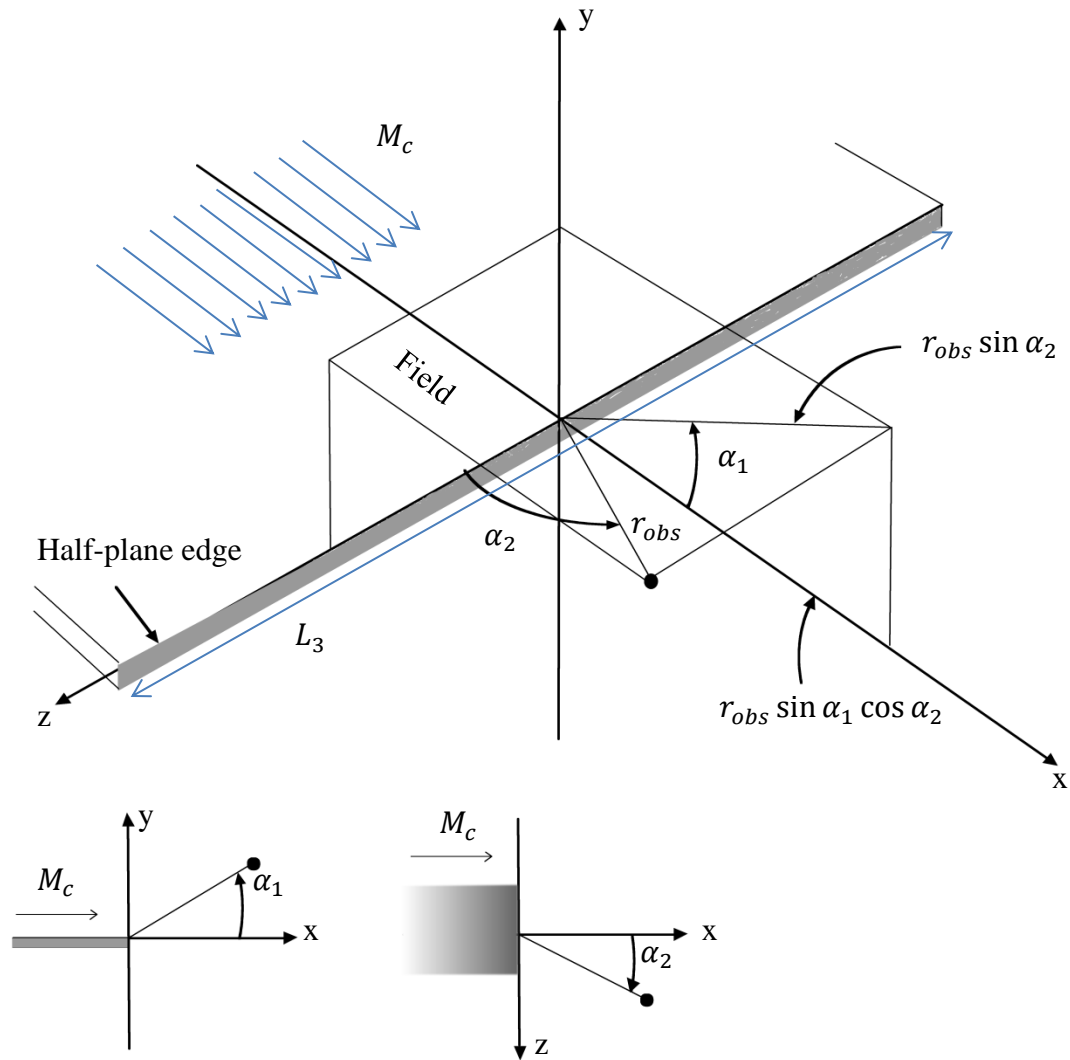


**Figure 1-3 Geometry of a dipole source near a rigid half-plane.**

This is an idealization of the TE sound for non-compact radiation. The concept of this figure is taken from Fig. 11.3 of Blake, 1986.

The Eq. 1.15 holds for a semi-infinite half-plane edge. In other words, the Eq. 1.15 is valid when the chord length is larger the acoustic wave length ( $c_0/f$ ) which follows for the frequency greater than  $C/c_0$  (i. e.,  $f > c_0/C$ ). In this condition, the airfoil is called a non-compact airfoil. Blake (1986) has also presented a relation that can provide the acoustic radiation from a compact airfoil based on the predicted radiated TE spectra ( $[\Phi_{P_{rad}}(f)]_{edge}$ ). If one neglects the directivity effects, there results:

$$\frac{[\Phi_{P_{rad}}(f)]_{edge}}{[\Phi_{P_{rad}}(f)]_{compact}} \simeq \frac{8}{\pi \left(\frac{\omega C}{c}\right)} \quad (1.16)$$

where, Eq. 1.16 is valid for compact airfoil. Neglecting the directivity effects in this study, and accounting for compactness of an airfoil in the frequency range of interest, the Eq. 1.15 and Eq. 1.16 follows as:

$$[\Phi_{P_{rad}}(f)]_{edge/non-compact} = \Phi_{PP}(f) \frac{1}{4\pi^2} \frac{L_3 \Lambda_3(f)}{|r_{obs}|^2} M_c \quad f > \frac{c_0}{C} \quad (1.17)$$

$$[\Phi_{P_{rad}}(f)]_{compact} = \Phi_{PP}(f) \frac{fC}{16c_0} \frac{L_3 \Lambda_3(f)}{|r_{obs}|^2} M_c \quad f < \frac{c_0}{C} \quad (1.18)$$

The  $c_0/C$  ratio is about 2.5 KHz for the RCDB, given that the RCDB chord length is 133.9 mm. We can then conclude that the RCDB can be considered to be a compact airfoil below 2.5 KHz, but not beyond this frequency. For the frequency above the limit, we can use the half edge noise principle which is an extended dipole source noise.

As discussed,  $\Phi_{PP}$  is the auto-spectral density of the surface pressure fluctuations and it can be either obtained by time resolved surface pressure measurements or semi-empirical models. The latter requires flow measurements to obtain boundary layer characteristic. In this work, it is intended to use the Goody's semi-empirical surface spectra given that wake measurements have been obtained.

## 1.7 Rotating flow field

Consider a cross section of the RCDB at distance “ $r$ ” with respect to the fan axis as shown in Fig. 1.4. Then, assume an inertial reference frame (ground) and a rotating reference frame

attached to the blade, rotating with the rotational velocity  $\Omega$  around the axis of the fan. The relationship between two vectors  $\overline{V_{a/g}}$  and  $\overline{V_{a/b}(r)}$  (where a=air, g=ground and b=blade), measured in the inertial and rotating reference frames respectively, can be found as follows:

$$\overline{V_{a/g}} = \overline{\Omega} \times \overline{r} + \overline{V_{a/b}(r)} \quad (1.19)$$

where,  $\overline{\Omega} \times \overline{r} = \overline{V_{b/g}} = -\overline{V_{g/b}}$ . Thus,

$$\overline{V_{a/b}(r)} = \overline{V_{g/b}} + \overline{V_{a/g}} \quad (1.20)$$

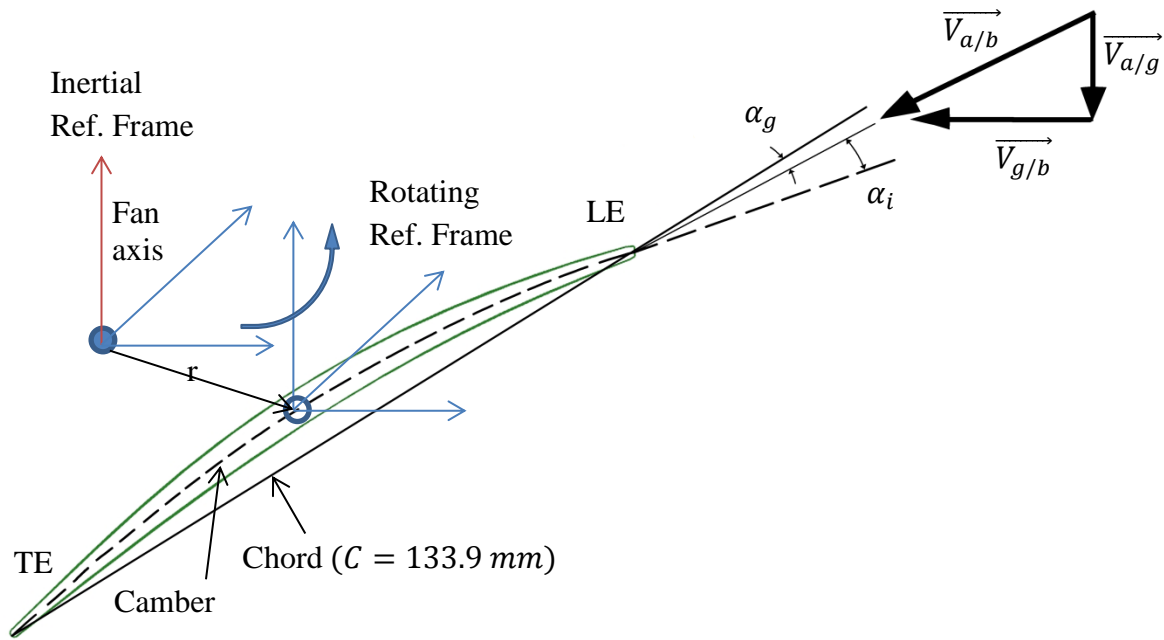


Figure 1-4 Flow geometry schematic

Following the conventions,

$$|\overline{V_{a/g}}| = \overline{U} \text{ is the mean axial velocity}$$

$$|\overline{V_{a/b}(r)}| = W_\infty(r) \text{ is the blade relative velocity}$$

The angle between the  $\overrightarrow{V_{a/b}}$  and the chord direction is called geometric angle of attack  $\alpha_g$ . This angle is often used for stationary airfoils in aerodynamic community. The angle between  $\overrightarrow{V_{a/b}}$  and the tangent to the camber at the LE is called angle of incidence  $\alpha_i$ , which is often used for rotating airfoils (i.e. a fan) in the turbomachinery community.

It is instructive to note that, these angles are essentially the same for a symmetric airfoil. Also, noting that the incidence angle (IA) is a good measure to predict where the stagnation point in the LE is formed. It is typical to assume that a flow with a negative AoI or positive AoI impinges on the suction or pressure side of the LE respectively.

For a blade with a constant cross section, the relationship between angle of attack ( $\alpha_g$ ) and incidence ( $\alpha_i$ ) angle is maintained. For the RCDB:

$$\alpha_g = 12^\circ + \alpha_i \quad (1.21)$$

The RCDB is a twisted blade with the same airfoil cross section (see Fig. 1.5). The stagger angle (the angle between the chord and axis of the fan) is approximately between  $61.5^\circ$  at the hub to  $31.5^\circ$  at the tip. A schematic of the blade cross sections is presented in Fig. 1.5. Generally, the airfoil twist is performed to maintain the AoA or IA. Note that, the velocity of the air to the blade ( $\overrightarrow{V_{a/b}}$ ) is a function of radial location.

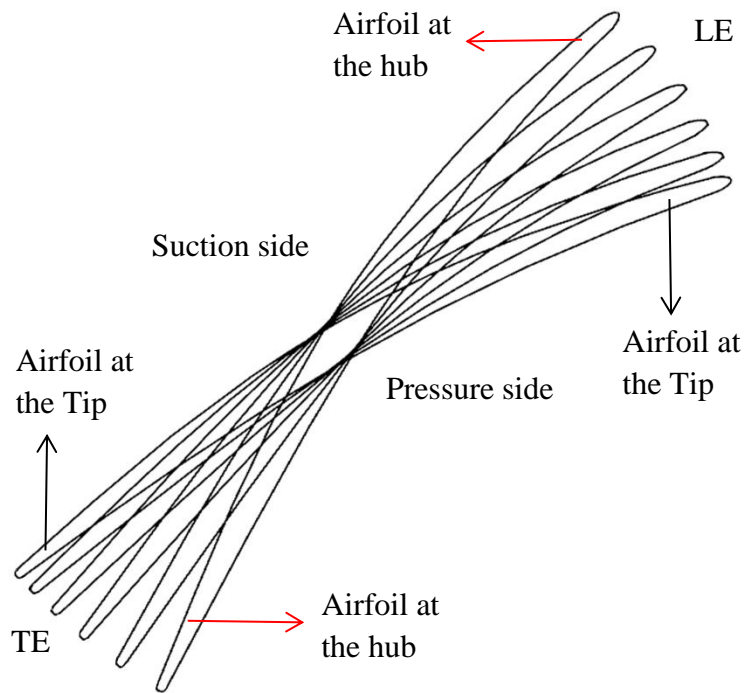


**Figure 1-5 RCDB cross sections from hub to tip**

## 2 EXPERIMENTAL EQUIPMENT AND PROCEDURE

### 2.1 Axial Fan Research and Development (AFRD) Facility description

The Axial Fan Research and Development (AFRD) facility is a research apparatus to study axial flow turbomachines. This facility is capable of: i) accommodating test fans with different sizes and ii) establishing different operating conditions. It can provide accurate flow measurements.

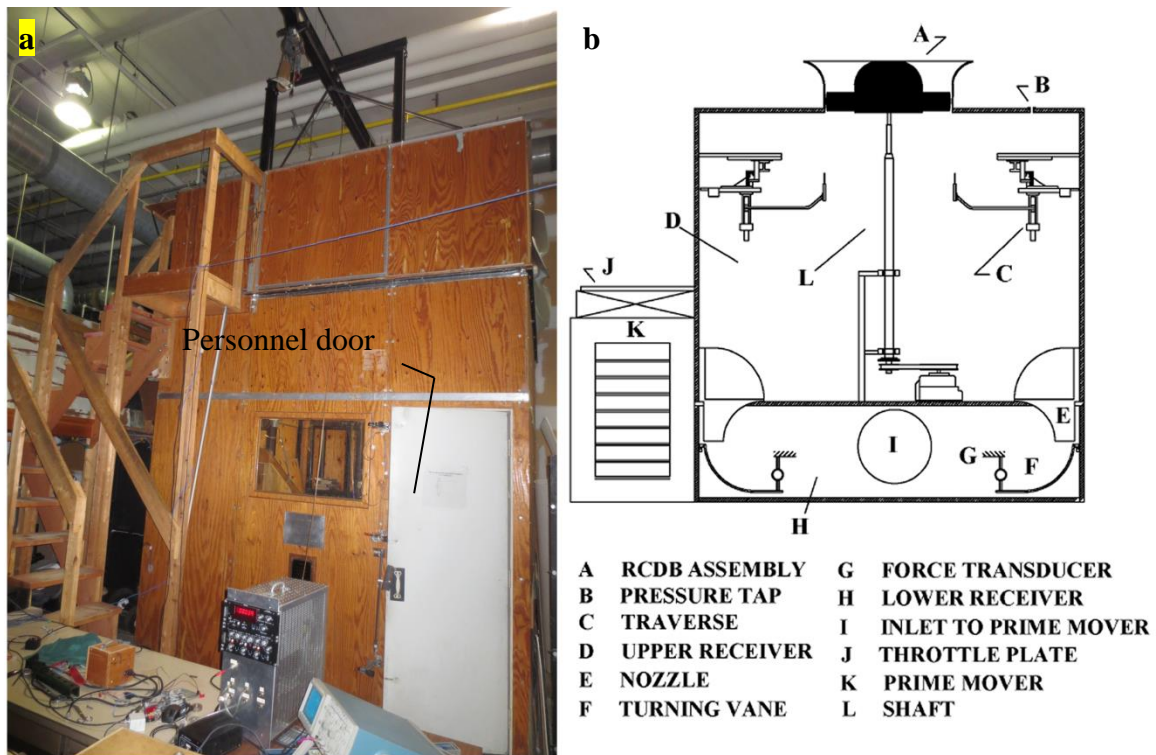
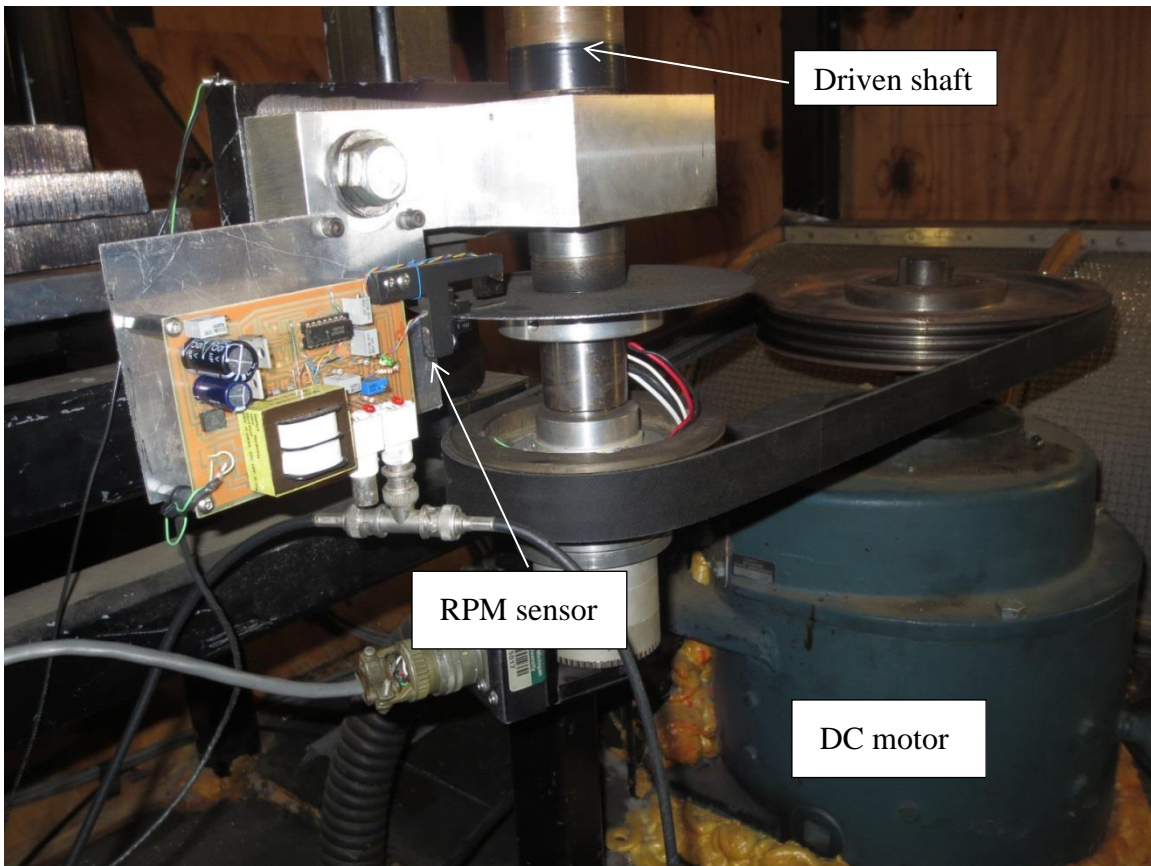


Figure 2-1 The Axial Fan Research and Development (AFRD) Facility. (b: Neal 2010)

The AFRD facility is located at the Turbulent Shear Flows Laboratory (TSFL) at Michigan State University. The schematic and a photograph of the facility are presented in Fig. 2.1. The test fan is installed at the inlet to the AFRD (see Part A of the schematic). As described in (Morris and Foss, 2001), the flow, before exiting the facility and discharging to lab ambient,

passes through a turning vane (Part F of the schematic) from which the mass flow rate through the fan is found. A calibrated force transducer (Part G of the schematic) measures the net moment-of-momentum flux, and from that the mass flow rate is obtained. The prime mover (Part K of schematic) is a helper blower to permit higher flow rates to be obtained. The flow will leave the facility from Part J of the schematic. The pressure differential across the fan is measured using a pressure tap embedded on the ceiling of the AFRD facility. Note that since the AFRD facility is considered a plenum, the upper receiver pressure measured at the part B of the schematic is essentially equal to the static pressure of flow downstream of the fan. The test fan rotational velocity is set by a 15 horse power DC motor (see Fig. 2.2).



**Figure 2-2 Driver motor and RPM sensor**

A traverse mechanism to support and to position a hot-wire anemometer probe downstream of the fan is available; see Fig. 2.1, part c. The traverse can move in three dimensions and be placed at any desired location.

## 2.2 AFRD modification

Because of the “helper” blower intrusive noise, it was decided to not operate it while acoustic data were acquired. Removing the “helper” blower as one of the active flow inducers required modifications to the AFRD in order to obtain an “as-large-as-possible” flow rate. Also, the pressure drop associated with the turning vane flow meter limited the flow rate as provided by the test fan operating as the sole prime mover.

These two factors led to the following modification:

1. Removal of the cover hatch ... such that a “return to the lab ambient” flow path was opened ... was carried out as shown in Figs. 2.3 b.
2. The system flow rate ( $\dot{m}$ ) is now obtained using the receiver pressure ( $P_R$ ). This pressure is used to identify  $\dot{m}$  using the performance data as described in Chapter 3 of this document.

A further issue was how to control  $\dot{m}$  (the mass flow rate). This issue was addressed by using the personnel door (Fig 1.1 a) to the AFRD as a “throttle”. Fig. 2.3 shows the mechanical adjustment for the door position. The  $\Delta P \approx 0$  condition is obtained with the Chicago Blower throttle plate and the personnel door fully open. Progressively closing the personnel door followed by progressively closing the Chicago throttle permits well controlled ( $P_R - P_{atm}$ ) flow states to be obtained.



**Figure 2-3 a) Lead screw adjustment on the AFRD personnel door. b) Cover hatch (now removed) location on the east wall of the AFRD facility.**

Note: the lead screw adjustment provides a “fine” adjustment of the operating point.

### **2.3 Fan description**

The Fan hub is capable of accommodating multiple RCDB configurations. Nine and three blade configurations have been examined in this study. Among the possible blade configurations, the flow field of a RCDB in the 3-blade fan was found to have the most similar pressure distribution over the blade as that of the single stationary blade flow (Neal, 2010). The three blade fan has a low solidity ( $\sigma = 0.209$ ), and the blades are far from each other. Blade-to-blade interaction was minimized for this configuration. This was particularly true for high mass flow rates in which the interaction is generally the least. In contrast, the 9-blade configuration is representative of a relatively high solidity ( $\sigma = 0.628$ ) axial fan. Selecting these two configurations has covered two distinct situations as discussed in the following chapters.

Blade solidity ( $\sigma$ ) is defined as:

$$\sigma = \frac{C}{S} \quad (2.1)$$

where,  $C$  is the chord length ( $= 133 \text{ mm}$ ) and  $S$  is the blade pitch defined as  $2\pi r_{mid}/B$ . Note that,  $r_{mid} = 303 \text{ mm}$  which is the radius of the mid-span.

The fan hub radius ( $r_{root}$ ) is 240 mm, and the tip radius ( $r_{tip}$ ) is 366 mm. The tip clearance is 4 mm as shown in Fig. 2.7.

The inflow to the fan is guided by an inner hub and an outer shroud. It is expected to lead to an approximately uniform axial inlet velocity ( $\bar{U}$ ). The CAD pictures of each configuration have been provided in Fig. 2.4.

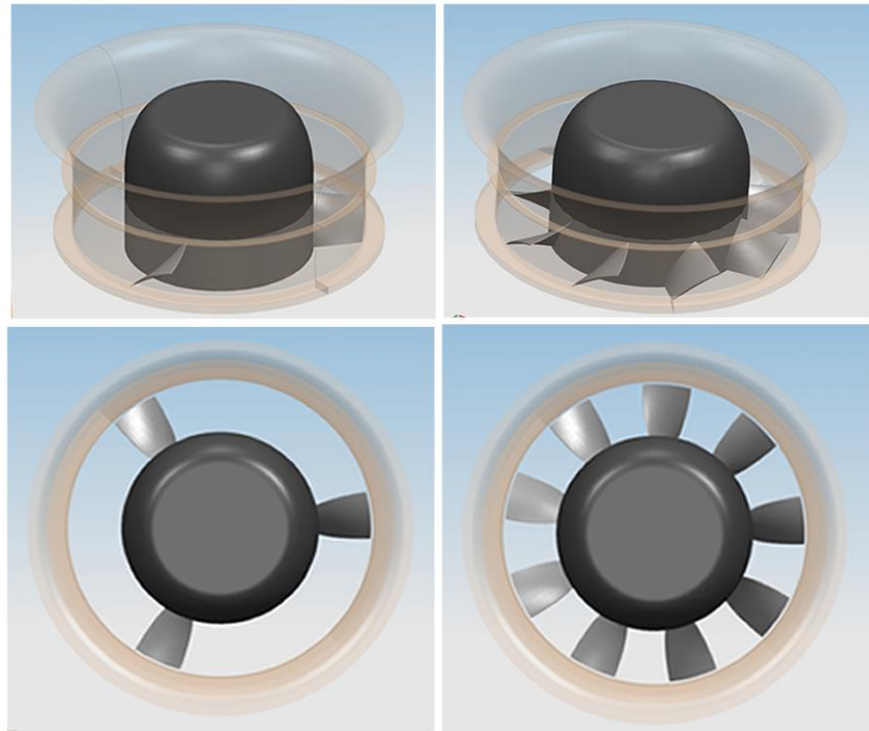


**Figure 2-4 Nine and three blade fan description**

## 2.4 Data acquisition

Data acquisition has been performed using two distinct Analog to Digital (A/D) boards: Daqboard 3035 and Wave-Book 516E. The Wave-Book can sample up to 1 MHz for 16 distinct channels. Similarly, the Daqboard is capable to sample up to 1 MHz rate, but for 64 distinct channels. The Wave-Book was used to measure: i) the temperature inside the AFRD facility, ii) hot-wire output voltages, iii) pressure differential across the fan, and iv) the RPM signal. The Daqboard 3035 was used to record microphone output signals above the fan plane as well as the RPM signal – the RPM signal was measured by both boards.

The Daqboard was positioned on an existing I beam above the fan plane (as shown in Fig. 2.19) in order to avoid using lengthy wiring for the microphones. The boards were not synchronized during data acquisition. However, it was managed to run both of the boards nominally at the same time. The Wavebook was sampled at 70 KHz for 95 seconds, and the Daqboard was sampled at 40 KHz for the same amount of time. A data path schematic has been provided in Fig. 2.5.

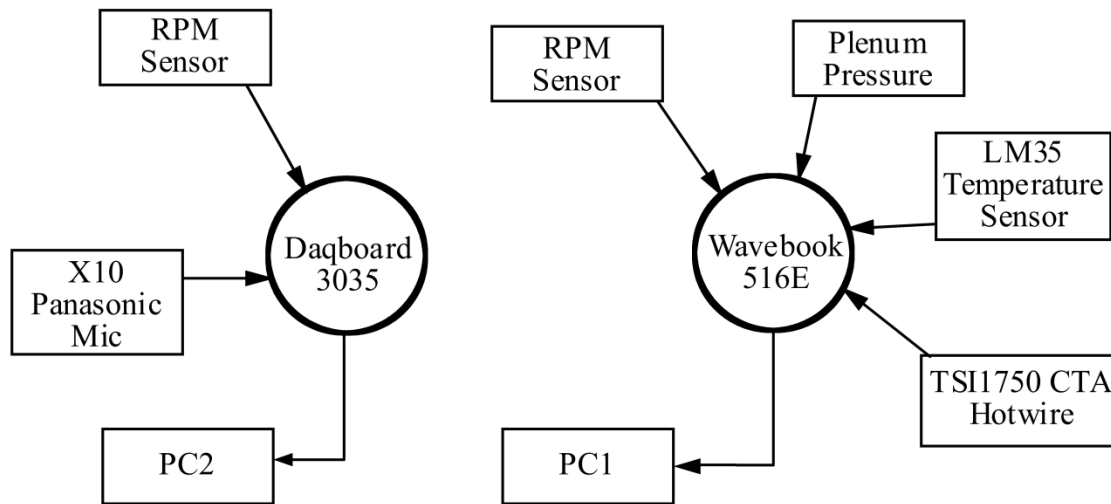


Figure 2-5 Data path schematic for both aeroacoustic and wake measurements

## 2.5 Wake measurements

Wake measurements were obtained using a single hot-wire probe for the constant temperature anemometer system. The hot-wire sensor was located 2 – 3 *mm* from the trailing edge downstream of the fan blade (see Fig. 2.8). A simple tuft experiment was used to establish the dominant flow direction and the hot-wire probe body was established in that direction in order to have the least effect on the measurement (see Fig. 2.7). Because of the unsteady nature of the measurements, especially for the separated flow cases, a convergence evaluation has been utilized to ensure that the statistics are converged (see Appendix B). It is noted that data were recorded for the highest possible capacity of the boards.

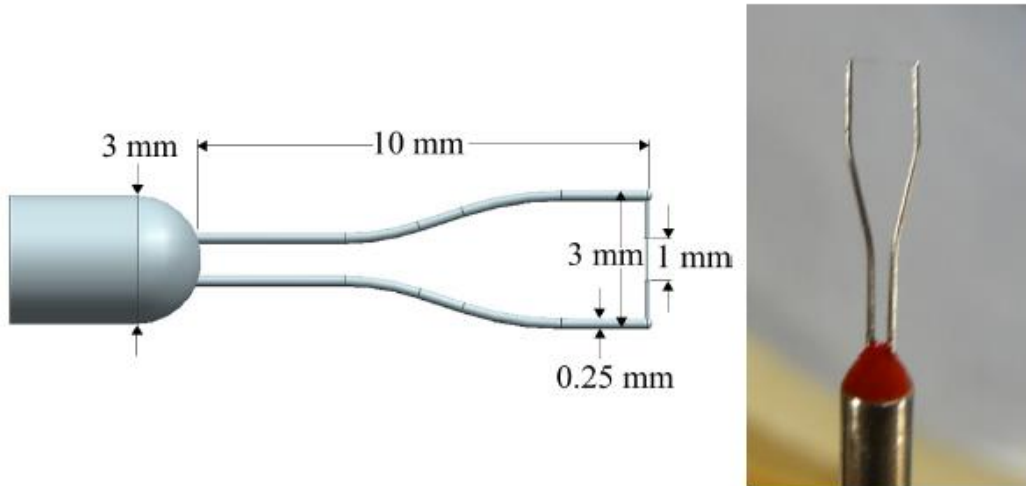


Figure 2-6 Schematic and image of Single probe hot-wire (Cawood, 2012)

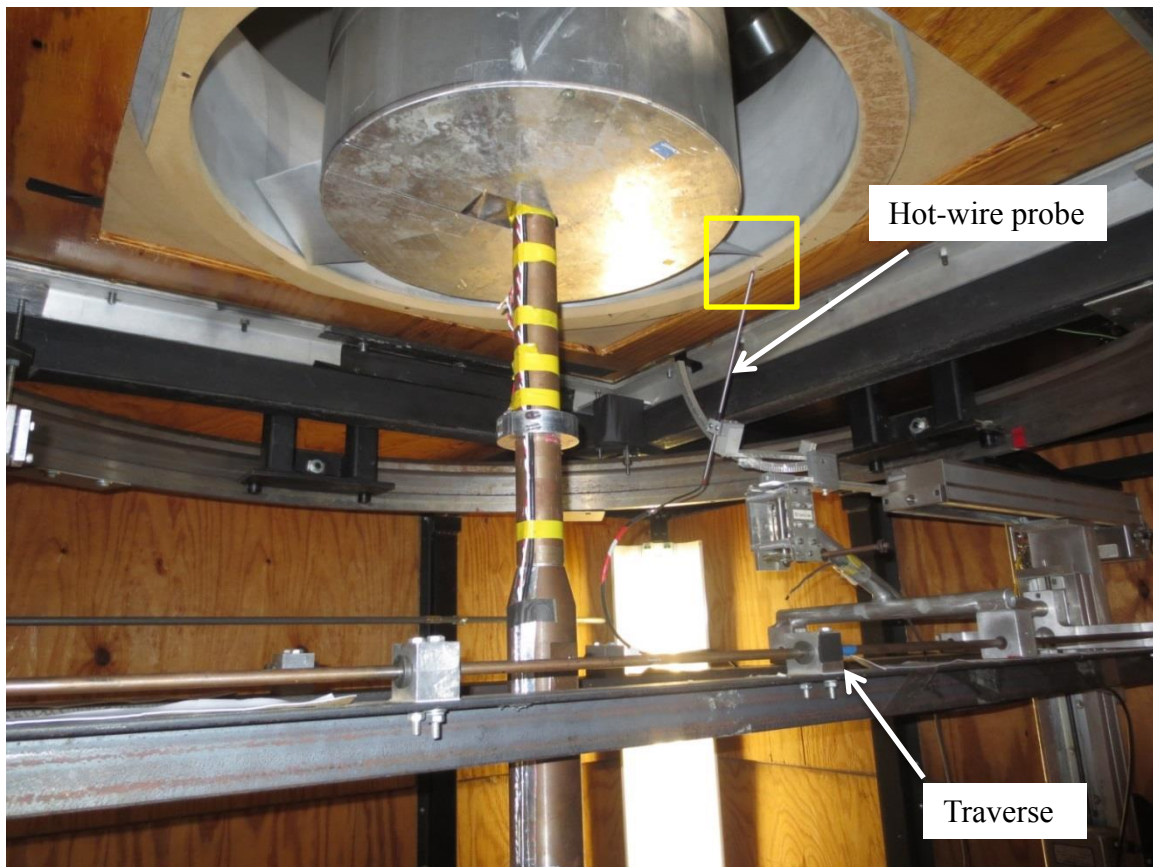
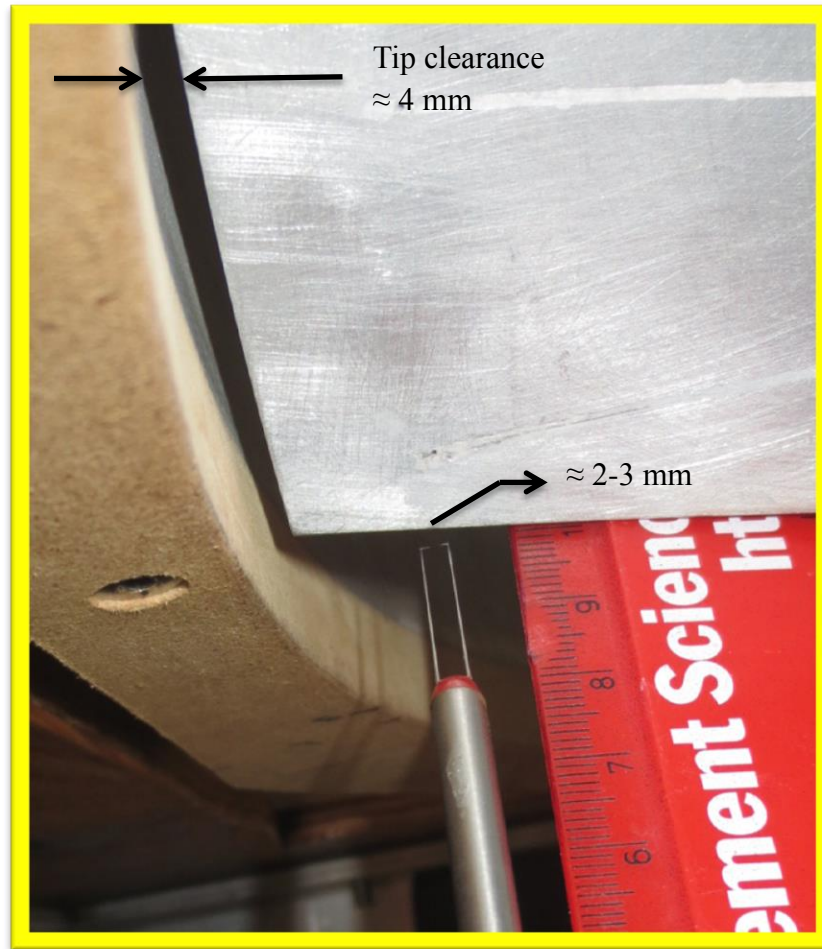


Figure 2-7 Wake measurements setup (3 blade fan is shown).  
 Note that a close-up of the yellow window is provided in the following figure.



**Figure 2-8 Trailing edge hot-wire location**

### **2.5.1 Hot-wire calibration**

Hot wire calibration using the TSFL “calibration facility” was performed. Hot-wire calibrations may be altered by time. Hence, calibrations were obtained preceding and following the wake measurements. The calibration facility is attached to a vacuum cleaner to derive the flow through the system. A pressure differential is measured (corresponding to the desired range of velocity) which is the pressure difference between pressure taps 1 and 2 as shown in Fig. 2.10. (See also part 9 in the Schematic of Fig. 2.9). The calibration velocity is obtained by Bernoulli’s equation as follows:

$$V_{cal} = \sqrt{2 \frac{P_2 - P_1}{\rho}} \quad (2.2)$$

For the single sensor hot-wire anemometer, the calibration velocity ( $V_{cal}$ ), which is obtained by Bernoulli's equation, is proportional to the squared of the output voltage of the hot-wire as follows:

$$E_1^2 = A_1 + B_1 V_{cal,1}^{n_1} \quad (2.3)$$

The  $A_1, B_1$  and  $n_1$  variables can be found such that Eq. 2.3 holds the best for the velocity range of interest.

Once the wake measurements were obtained, the hot-wire must be recalibrated to make certain that the calibration (pre-calibration) is still valid. To this end, the same calibration procedure is carried out (post-calibration). To make a comparison between pre and post calibrations, one can use the Pre-calibration  $A_1, B_1$  and  $n_1$  quantities and then obtain the corresponding velocity based on the post-calibration. The estimated velocity can be compared with the corresponding Bernoulli's velocity ( $V_{cal,2}$ ) in the post-calibration and an average drift evaluation in squared sense follows as:

$$drift_{1-2} = \frac{\sqrt{E \left\{ \left[ \left( \frac{E_2^2 - A_1}{B_1} \right)^{1/n_1} - V_{cal,2} \right]^2 \right\}}}{V_{cal,2}} \quad (2.4)$$

In general, the pre and post calibrations will be in adequate agreement ( $drift_{1-2} < 3\%$ ) if the data acquisition period lasts less than 2.5 hours.

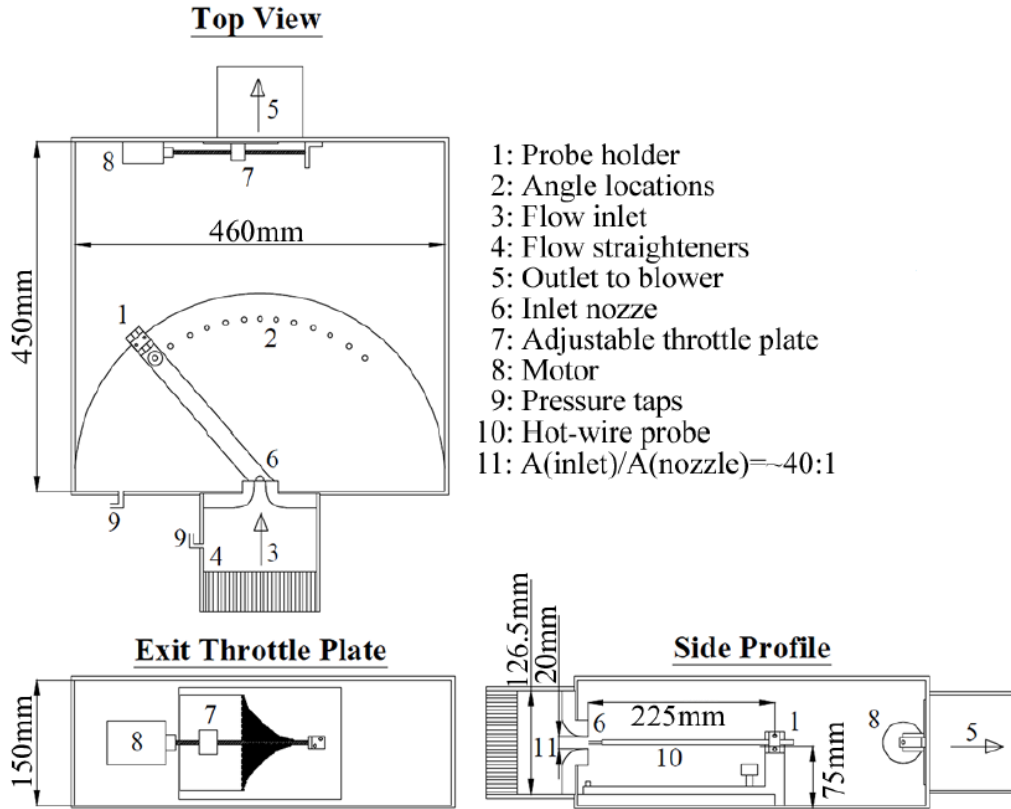


Figure 2-9 Hot-wire calibration box schematic (Cawood, 2012)

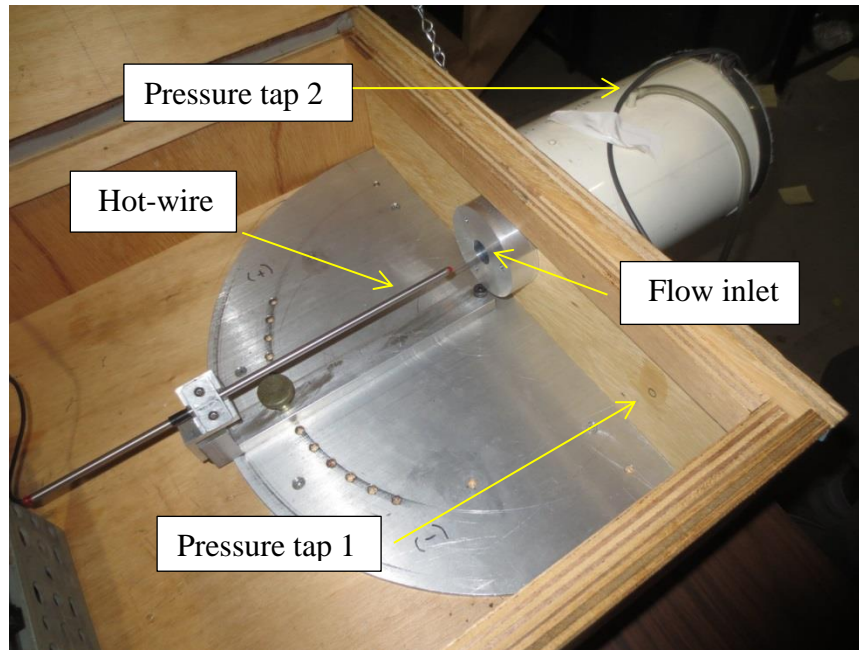
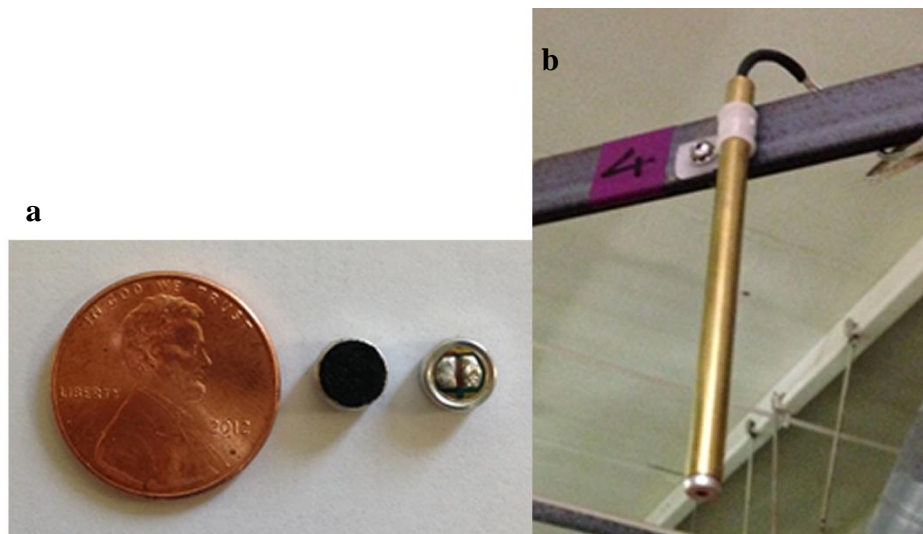


Figure 2-10 TSFL hot-wire calibration facility

## 2.6 Aeroacoustic measurements

### 2.6.1 Panasonic microphone development and calibration

The Panasonic microphones<sup>1</sup> represent a low-cost (\$2.20/mic) high quality microphone. Their physical size is shown in Fig. 2.11 which makes use of a one-cent coin to emphasize the small dimension ( $d = 6.32 \text{ mm}$ ) of this simple pressure-to-voltage conversion device.



**Figure 2-11 a) Panasonic microphone – front and back view. b) A hanging microphone**

Twenty microphones were acquired and their circuits were prepared. Brass tubes, to support the microphones and to guide and secure the electrical cables were fabricated; see Fig. 2.11 for a photo of an installed microphone in the experiment.

Calibration has been obtained using a “Master” Larson Davis (LD) Microphone. The LD microphone is able to provide an exact pressure signal representing the sound source. The manufacture description of that has been provided in Appendix E.

---

<sup>1</sup> See Appendix E for Panasonic microphone specifications

After examining different set-up configurations, the Larson Davis (LD) microphone was then used with the “face-to-face” orientation and a sound field delivered from complementary (woofer and tweeter) speakers. The LD reference microphone and each of the Panasonic microphones were exposed to white noise produced by a function generator as illustrated in Fig. 2.12. The Calibration rig was placed about 1 m away from the speakers, and the LD and the Panasonic microphones were placed about 1 mm away from each other as depicted in the photo of the calibration configuration; see Fig. 2.13. Data have been acquired for 20 seconds and with sampling frequency of 40 KHz.

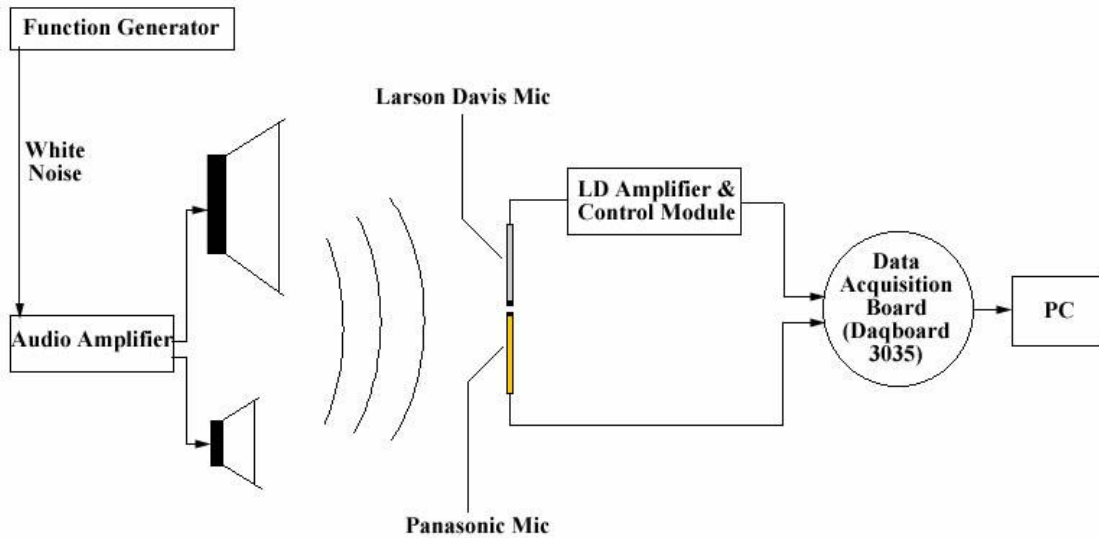


**Figure 2-12 Microphone calibration schematic**



**Figure 2-13 Panasonic calibration setup**

The larger speaker excited the low frequencies, and the smaller speaker (tweeter) excited the high frequencies. It is worth to note that, the wave-tube experiment, which is a typical method for calibration, was not used to calibrate the microphones. The reason is, once microphones are placed in a wave tube, the surrounding surface around a microphone might affect the calibration. In this study where the microphones are finally planned to freely hang in space for acoustic measurements, the wave tube experiment does not seem appropriate. A wave tube experiment is often used to calibrate microphones which are planned to be embedded on a surface for surface pressure measurement.

Once the test microphone is demonstrated to have an appropriate response, the coherence function examines whether the test and reference microphones were exposed to a same input signals (i. e., a white noise). Having an acceptable coherence is required to have a satisfactory calibration. As indicated by Bendat and Piersol (1986), the coherence function between two random signals “*a*” and “*b*” is defined as:

$$\gamma_{ab}^2 = \frac{|\Phi_{ab}(f)|^2}{\Phi_{aa} \times \Phi_{bb}} \quad (2.5)$$

where,  $\Phi_{ab}$  is the cross spectral density between “a” and “b”, and  $\Phi_{aa}$  is auto-spectral density of signal “a” and similarly for “b”.

Coherence > 98 % is considered to be a satisfactory calibration. To this end, speakers should have an acceptable excitation for the whole frequency range of interest. Also, a calibration setup (i. e., test microphone position with respect to the reference microphone or distance of microphones from the speakers) may have a significant effect on the coherence function.

A coherence function for a representative (mic # 8) follows in Fig. 2.14.

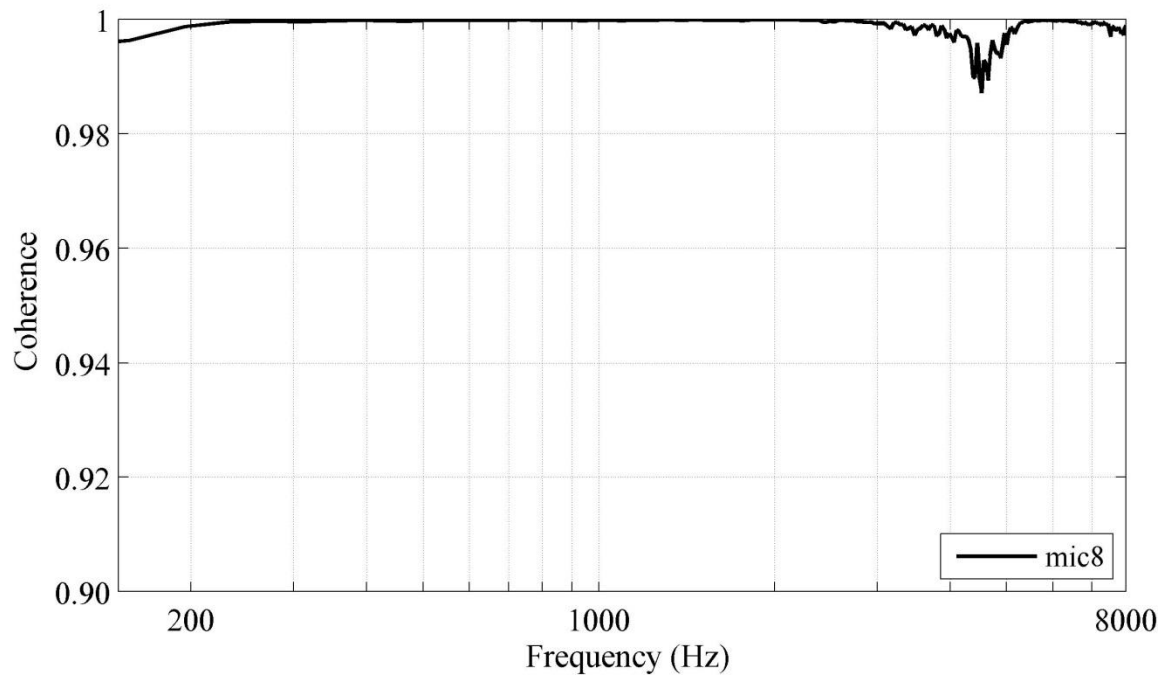


**Figure 2-14 Coherence function for Panasonic microphone # 8**

As noted, a quite satisfactory coherence was obtained for frequency band of interest: 200-8,000 Hz.

The LD microphone is able to provide an exact magnitude and phase for a pressure signal, and the objective is to establish a transfer function (TF) by which exact Pascal values using the inexpensive microphones can be obtained. The calibration procedure schematic is provided in Fig. 2.15.

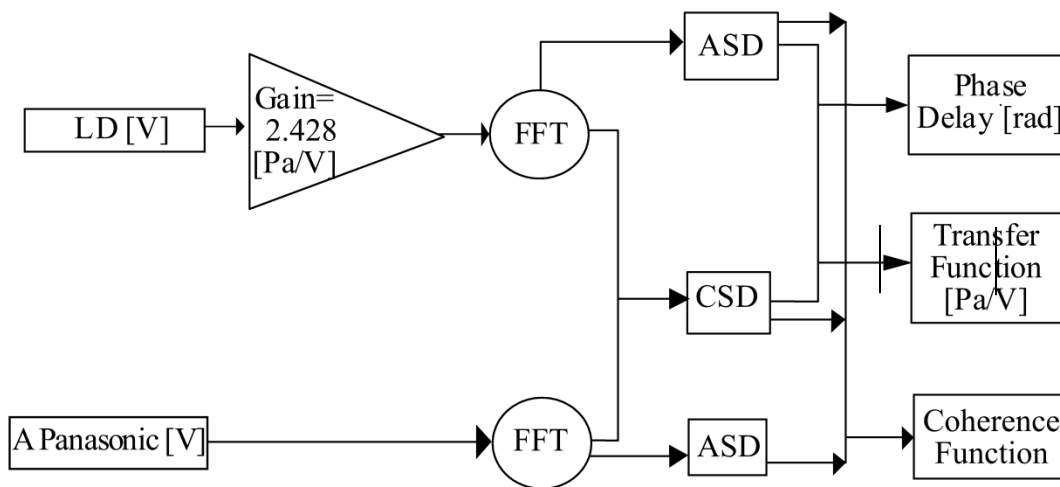


**Figure 2-15 Calibration procedure**

A complex transfer function is typically defined as ratio of the cross spectral density (CSD) between reference and test sensor over the auto-spectral density (ASD) of the reference (Bendat and Piersol, 1986). However, it is defined here as the inverse quantity which has the [Pa/Volt] unit.

$$TF = \frac{ASD \text{ of } LD}{CSD \text{ between } Pana \text{ and } LD} = \frac{\Phi_{LD LD}}{\Phi_{LD Pana}} \quad (2.6)$$

Fig. 2.16 illustrates the magnitude of the transfer function as a function of frequency for the mic # 8. As noted, the  $|TF(f)|$  is quite flat and almost frequency independent. Ten Panasonic microphones were identified through the calibration procedure that had the most frequency independent transfer functions in the targeted range of 200-8000 Hz. The adequately high quality of a microphone is represented by the flatness of its  $|TF(f)|$ .

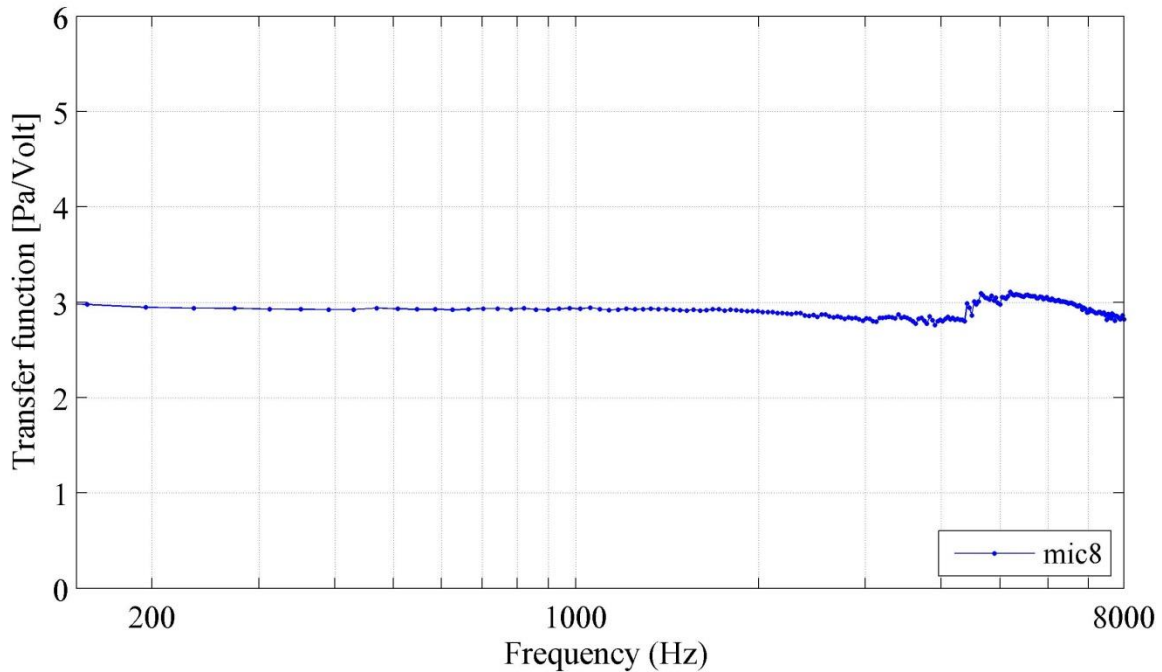


**Figure 2-16 The Volt-to-Pascal transfer functions of a representative microphones**

Based on the satisfactory flatness of the resultant  $|TF(f)|$ , one can obtain a constant for  $|TF(f)|$  by averaging over the frequency ( $f$ ) range as:

$$|TF_{avg}| = \frac{1}{8000 - 200} \int_{200}^{8000} |TF(f)| df \quad (2.7)$$

For simplicity,  $TF_{avg}$  or  $TF$  are used instead of  $|TF_{avg}|$  or  $|TF|$  respectively in the following descriptions. It is worth to mention that, the satisfactory quality of the inexpensive Panasonic microphone would essentially allow the use of Beamforming technique.

Frequency dependent phase delay between the Master LD microphone and each Panasonic microphone has been investigated. Phase delay is defined as the angle of the complex transfer function established in Eq. 2.7. Phase delays of the ten selected microphones were examined, and it was found that the phase delays are approximately close to zero as shown in Fig. 2.17.

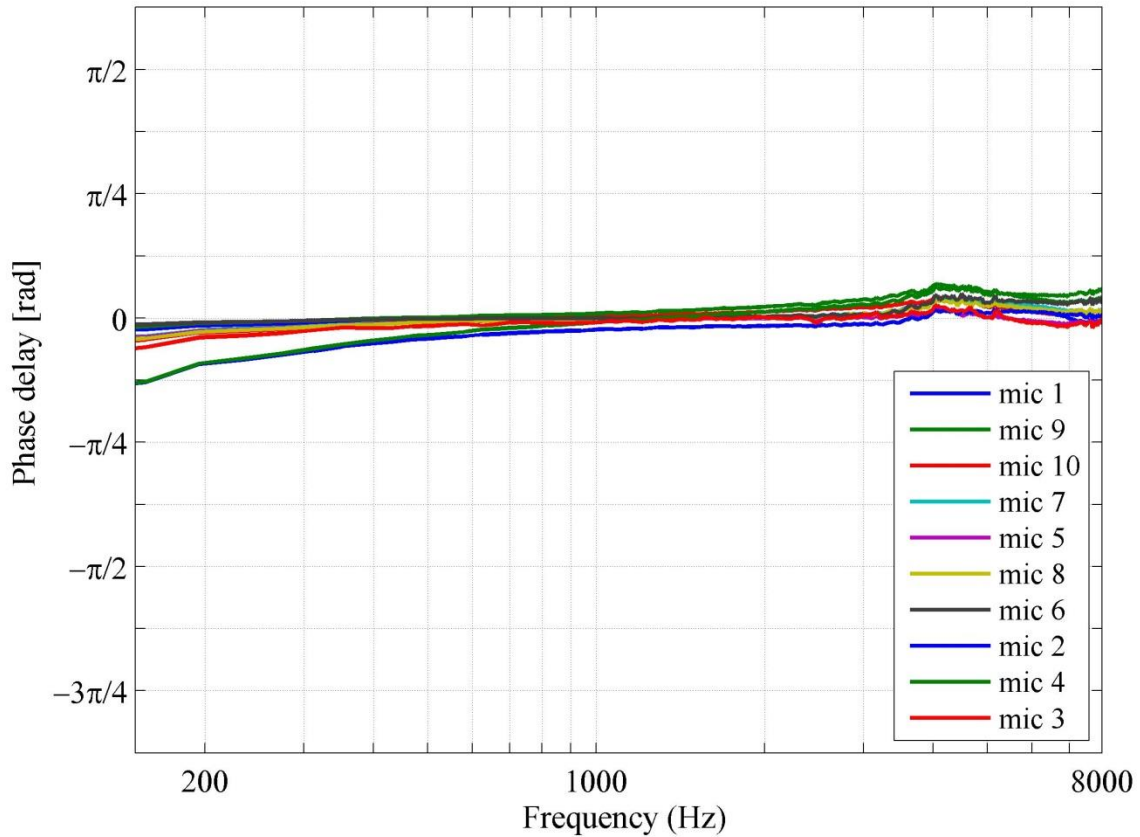
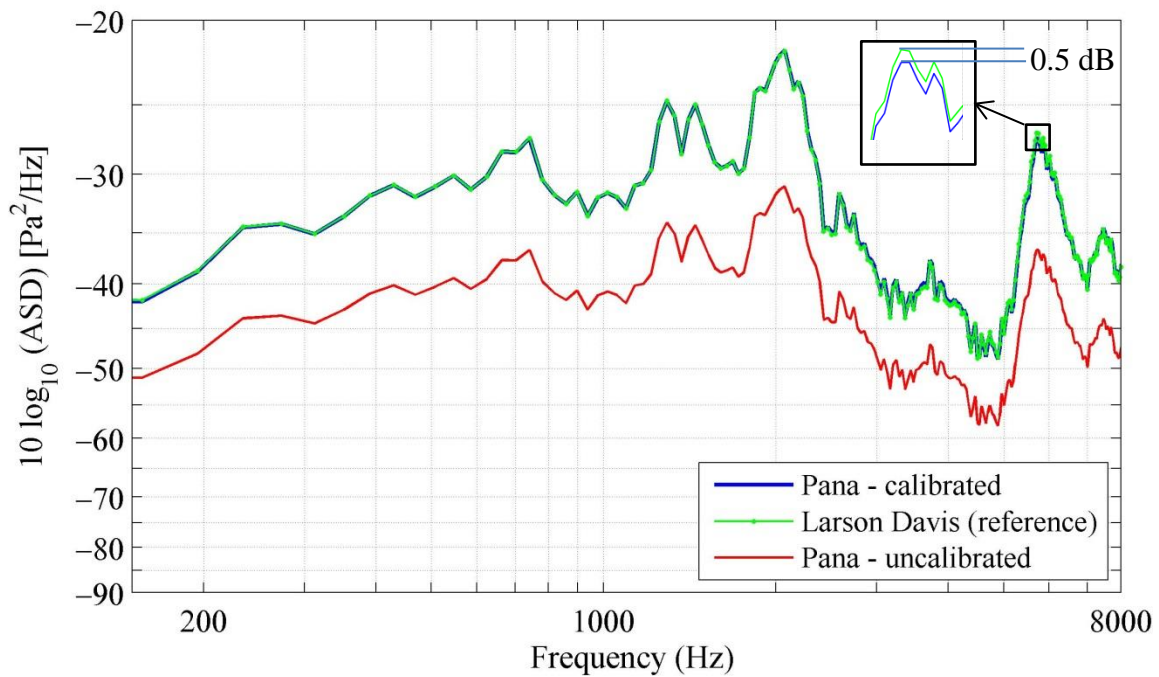


Figure 2-17 Phase delay between Panasonic microphones and LD reference mic

Applying the averaged transfer function  $TF_{avg}$  on the Panasonic uncalibrated signal, one can obtain a conversion from the Panasonic voltage to the corresponding Pascal values. Fig. 2.18 indicates the auto-spectra density of an un-calibrated Panasonic microphone (in volts) versus the corresponding calibrated spectrum and the LD reference microphone spectrum. Note that, all of test microphones and the reference microphone have been exposed to the same noise intensity throughout the calibration.



**Figure 2-18 ASD Comparison between the calibrated and uncalibrated Panasonic mic and LD reference mic.**  
 Note that LD and calibrated Panasonic spectra have well overlapped. Note also, the Panasonic - uncalibrated spectrum is in  $[Volt^2/Hz]$

As shown in Fig. 2.18, the assumed average transfer functions, have properly calibrated the Panasonic signals. Also, the difference between a calibrated Panasonic and LD reference microphones signal is at most 0.5 dB.

## 2.6.2 Beamforming

Beamforming is a general term that refers to an array of transducers whose independently received signals can be used to gain quantitative information about the signal strength from an isolated region. This generic approach is best described in the context of the present experimental approach.

The objective is to provide auto-spectral density acoustic data for the 3 and 9 blade fan configurations with various operating conditions. The challenge is to separate the fan self-noise from other noise sources in the non-anechoic laboratory environment.

Microphones have been arranged in two circular arrays and placed at two separate heights above the mid-span of the blades ( $r_{mid} = 303 \text{ mm}$ ); see Fig. 2.19 a and b. It is recognized that each microphone in the arrays will receive the target sound (from the blades) plus the ambient noise in the laboratory. The majority of the extraneous background noise comes laterally from the air conditioning fans of the building facilities. Reflection from the walls of the AFRD facility as well as the walls of the laboratory adds to the noise levels recorded by the microphones as can be seen in Fig. 2.19. It has been assumed that noise in the direction of the fan axis would be created only by the test fan while operating.

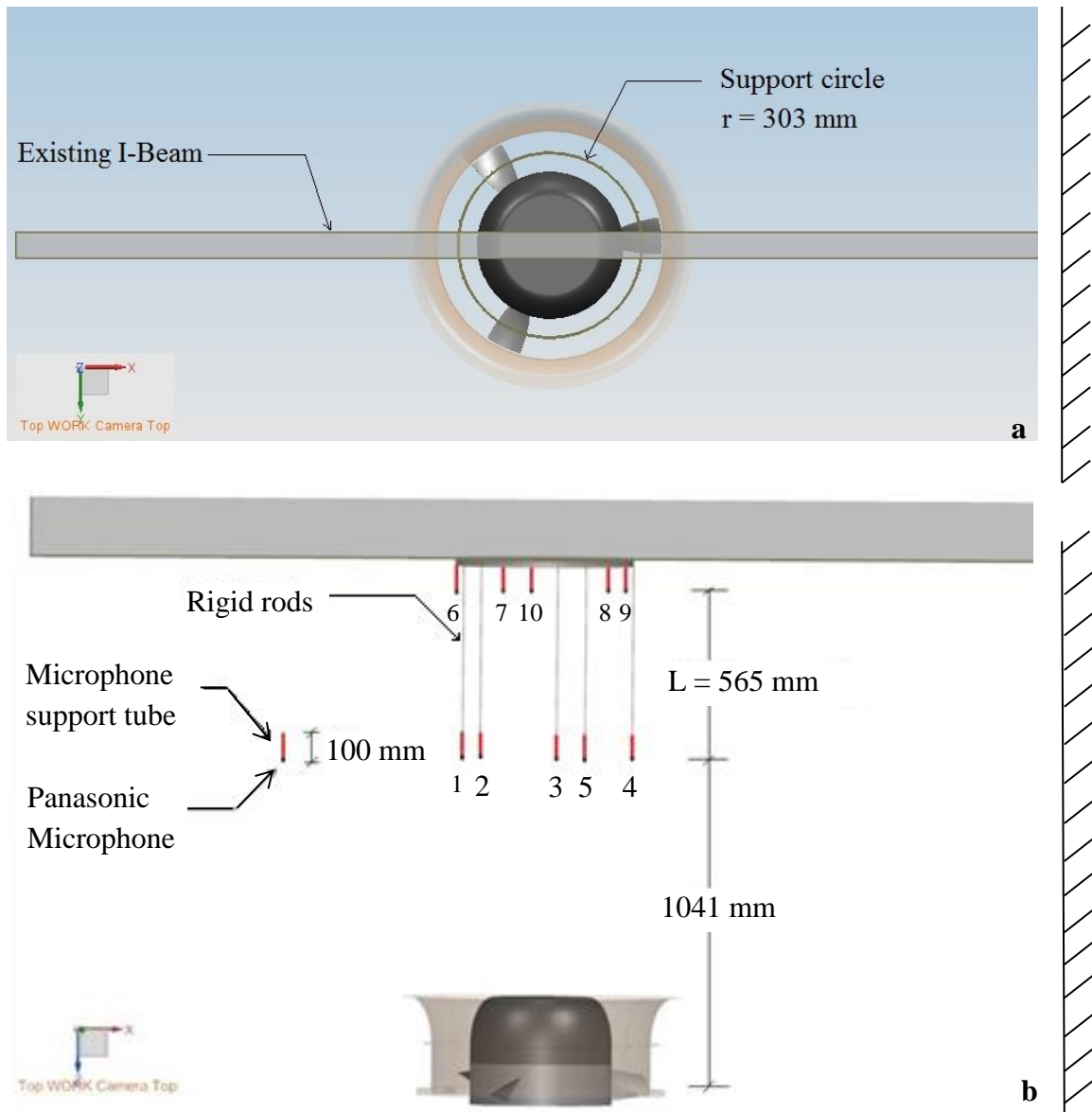


**Figure 2-19 Schematic of circle arrays above the fan plane. a) top view, b) side view**

A method to employ the beamforming technique for the present study has been developed; it is schematically described in Fig. 2.20.

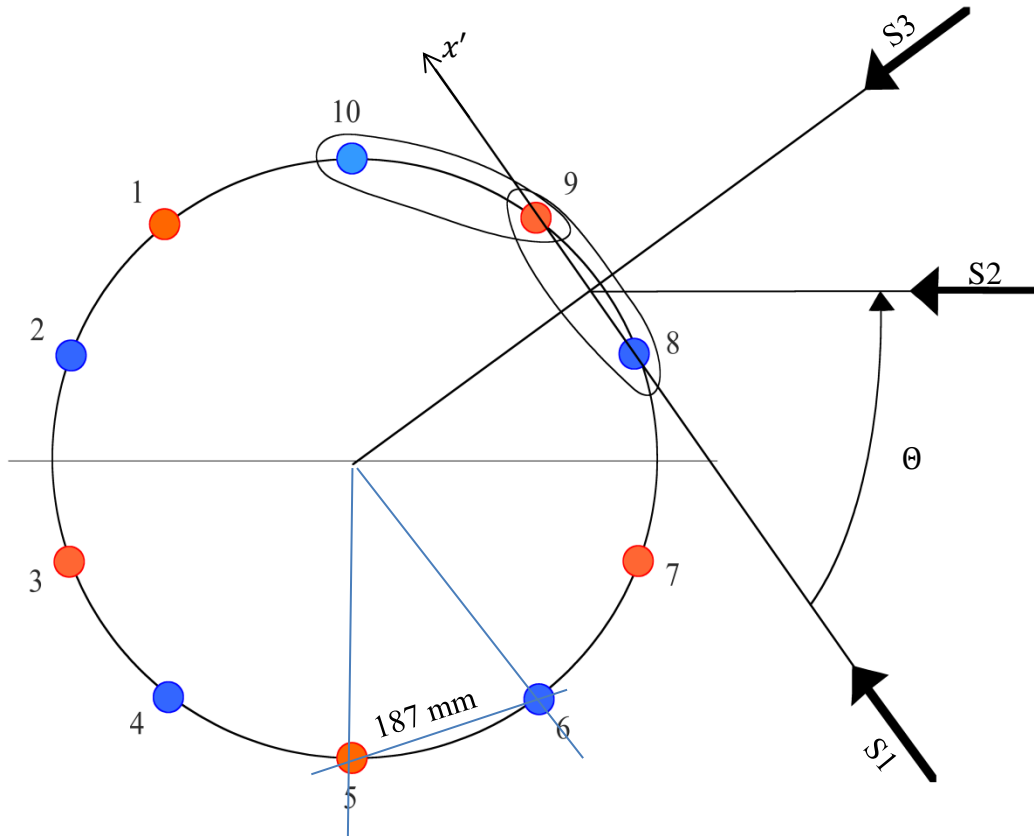


**Figure 2-20 Beamforming technique description.**

Note that, blue mics (6 to 10) are located in the upper circle and red mics (1 to 5) are located in the lower one. (see also Fig. 2.19)

Let  $S_1$  be a laterally propagating acoustic disturbance at the upper and lower circle arrays. Mic # 8 and mic # 9 will respond to this sound source. As noted,  $S_1$  among all possible lateral sound sources ( $0 < \theta < 2\pi$ ) requires the most time to reach to mic # 9 from mic # 8. This delay in time, which is the time a sound wave needs to reach from one mic to another mic, follows as:

$$t_{\text{delay-lateral}} = \frac{\Delta x'}{c_0} \quad (2.8)$$

where  $c_0$  is the sound velocity and  $\Delta x'$  is the lateral distance (the chord of the circle) between two adjacent microphones. Obviously,  $S_1$  and  $S_3$  correspond to maximum and minimum time

lag respectively for these two microphones. Any sound source with the direction of S2 is between the corresponding S1 and S3 time lags. Note that, mic # 8 and mic # 9 experience the S3 sound source simultaneously which results in a zero time lag. Thus, it can be concluded that the time lag associated with a lateral extraneous noise between two adjacent microphones is:

$$0 < t_{delay} < 0.543 \text{ ms.}$$

Given the objective of isolating the fan self-noise from the other acoustic sources, it is logical to begin the processing by developing new “paired” time series in which a lower microphone (e.g., mic #8 in Fig. 2.20) is delayed in time by ( $t_{delay-vertical} \approx L/c_0 \approx 1.67 \text{ ms}$ ) and combined with an upper microphone (9 for this example). Considering the long-term data acquisition, it is apparent that the “long” time delay and the long averaging time for this new signal will suppress the laterally arriving signals such as S1, S2, S3 in Fig. 2.20 as  $0 < t_{delay-lateral} < 0.543 \text{ ms}$ . Similarly, the signal at mic #9 can be combined with that of mic #10 with the same time delay to make a second “new” signal. Continuing this pattern, the five microphones of the top row will produce 10 new time series.

One of the new time series can be selected as the “master” and cross correlations with a time delay =  $\delta t_1$ , can be formed to determine the delay that best aligns the other 9 new signals to that of the master. It was determined that a small number of sample steps = 2 – 8 or 50 – 200  $\mu s$  accomplished the final alignment. The combined ten time series were then used to represent the self-noise of the fan. To recapitulate, one can magnify the fan self-noise while any other sound source, which is not in the direction of fan axis, will be attenuated

The corresponding number of samples (sample delay) that is corresponding to the time delay can be obtained as follows:

$$N_d = \lceil f_s \times t_{delay} \rceil = \lceil 40000 \times 1.64 \times 10^{-6} \rceil = 65 \quad (2.9)$$

where,  $f_s$  is the sampling frequency. The computing formula to combine the array averaged signals from the two arrays can be written as shown in Eq. 2.10 where  $mic(j)$  is the signal of mic # j, and  $mic_{shifted}(j)$  is the shifted signal of mic # j.

$$\frac{1}{10} \left\{ \sum_{j=1}^5 [mic(j) + mic_{shifted}(j + 5)] + \sum_{j=2}^5 [mic(j) + mic_{shifted}(j + 4)] + mic(1) + mic_{shifted}(10) \right\} = p' \quad (2.10)$$

It is instructive to mention that the cross correlation technique has been used to establish the sample delay between a lower-array mic and an upper-array mic instead of using theoretical sample delay ( $N_d$ ) obtained by Eq. 2.9 as height differentials cannot be measured accurately, and also sound directivity of the moving sound sources (i. e., blades) is very complicated, and is not ideally vertical. It was also later perceived that the sample lag is also dependent on the inflow axial velocity, and the noise demanded slightly more time to travel between lower and upper arrays for higher inflow velocity. Overall up to 5 sample delays ( $125 \mu s$ ) difference was seen between different inflow conditions. A photo of the array measurement setup has been provided in Fig. 2.21.

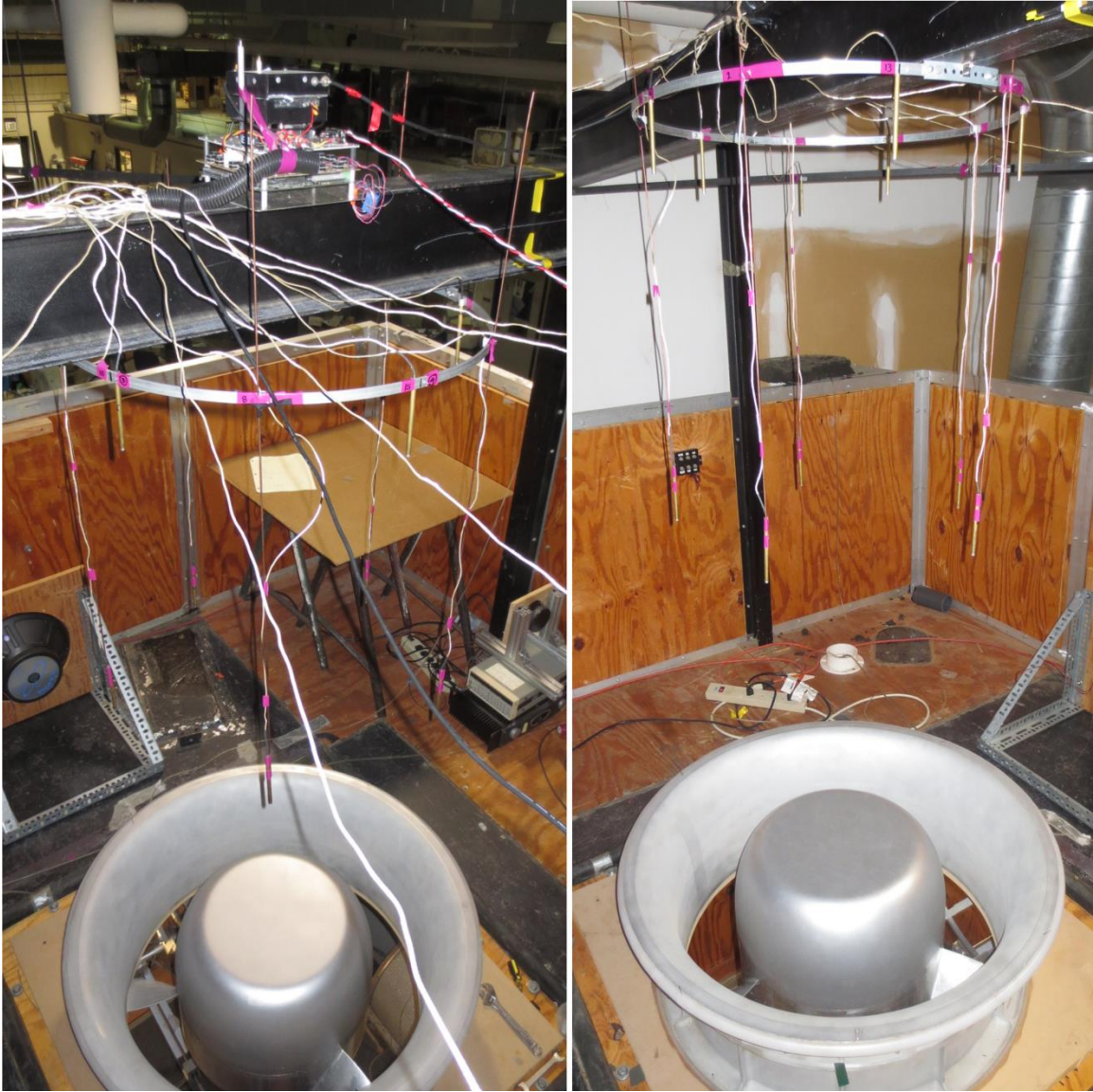


**Figure 2-21 Photo of microphones arrays measurement setup**

After finding the final pressure signal, one can apply the Fourier transform and determine the ASD of the fan self-noise. Note that the beam forming technique is essentially performed in the time domain, and the TF is applied before FFT processing. Fig. 2.22 demonstrates the acoustic measurements and processing.

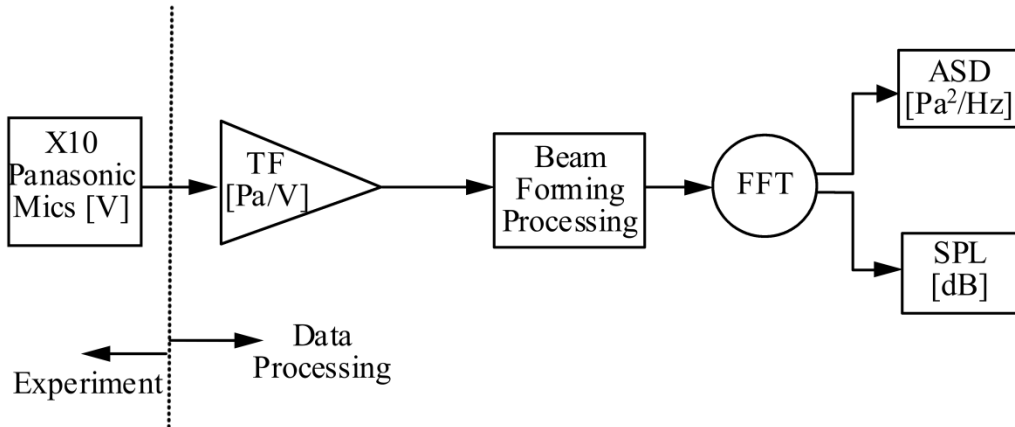


**Figure 2-22 Acoustic measurements and data processing schematic**

Sound pressure level (SPL) is an appropriate non dimensional reference to address how loud a sound is perceived. SPL is scaled with dB and is defined as:

$$SPL [dB] = 10 \log \left( \frac{\overline{p'^2}}{P_{ref}^2} \right) \quad (2.11)$$

where,  $P_{ref}$  is a reference pressure, and  $20 \mu Pa$  is used in this document as the reference pressure. It is more accurate to find the SPL in the range of calibration (200-8000 Hz). To this end, one needs to integrate the ASD over the range of interest.

$$SPL [dB] = 10 \log \left( \frac{\int_{200}^{8000} \Phi_{P,rad}(f) df}{P_{ref}^2} \right) \quad (2.12)$$

It is instructive to compare some known sound intensities with the presented data in chapter 3. For instance, a normal conversation at 1 m or the sound of an oncoming car at 10 m are

corresponding to 40-60 dB or 60 – 80 dB respectively. Note that, 85 dB is deemed to cause hearing damage if exposed to the human ear for a long time.

### 3 EXPERIMENTAL RESULTS AND DISCUSSIONS

#### 3.1 Performance curves

Following common conventions,  $\psi$  and  $\varphi$  are the non-dimensionalized pressure rise and mass flow rate respectively. They are often called the head rise coefficient and flow coefficient. They are obtained as follows:

$$\psi = \frac{2 \Delta P}{\rho V_{tip}^2} \quad (3.1)$$

$$\varphi = \frac{\bar{U}}{V_{tip}} \quad (3.2)$$

$\Delta P$  is the pressure rise across the fan.  $\bar{U}$  is the spatially and temporally averaged axial velocity of the inflow ( $\dot{m}/\rho A$ ), and  $V_{tip}$  is the blade velocity measured at the tip.  $A$  is the annular area:  $\pi/4 [D_S^2 - D_H^2]$ , at the fan plane, where  $D_S = 370 \text{ mm}$  and  $D_H = 240 \text{ mm}$  are the hub and shroud diameters respectively.

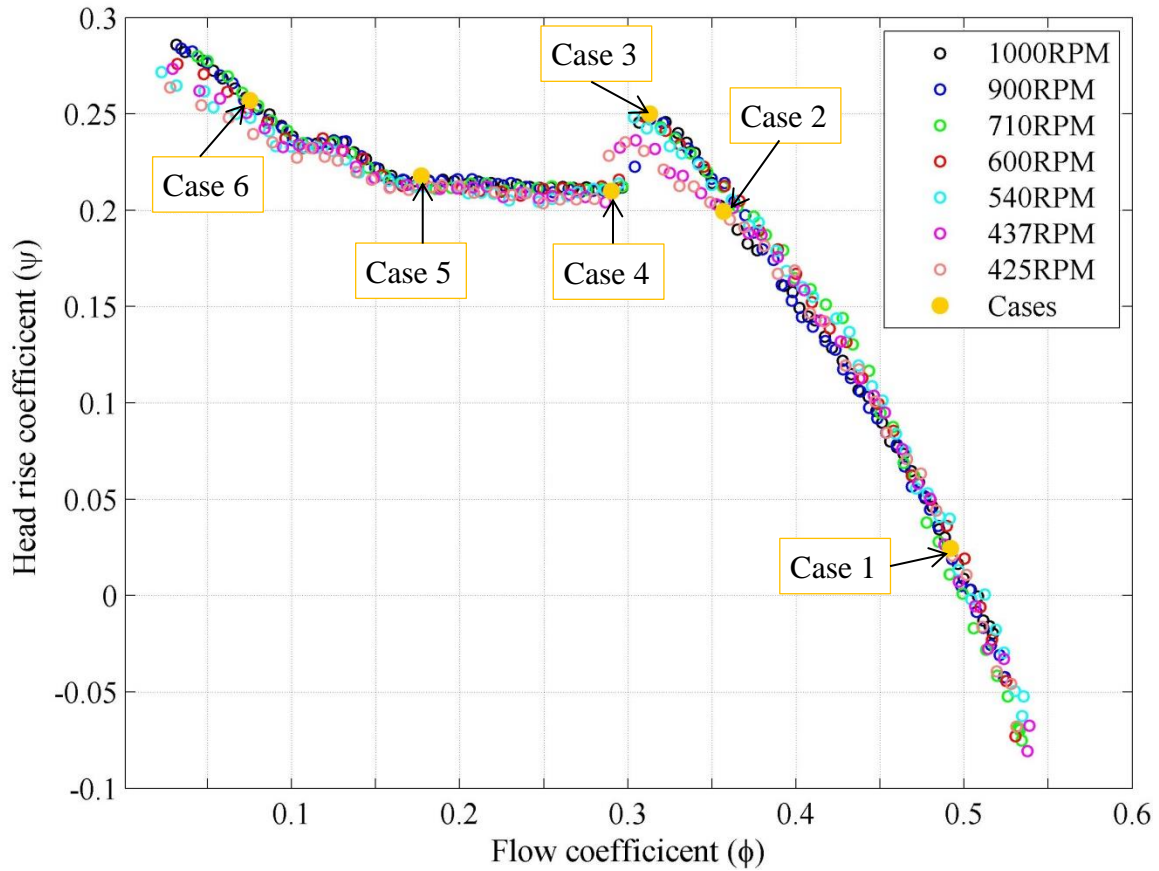


**Figure 3-1 Non-dimensional performance curves - 9 blade Fan.**

Note that Cases selected for future study are shown in the plot

It is instructive to note that the collapse of the non-dimensional pressure rise versus non-dimensional mass flow rate indicates that the integral properties of the flow are essentially independent of Reynolds number (Stephens and Morris, 2011). However, slight discrepancies, especially for lower RPM conditions, can be seen between case 2 and case 3 (shown in Fig. 3.1). It can be interpreted that insensitivity to Reynolds number is a more accurate assumption for higher RPM conditions (i. e., higher Reynolds number).

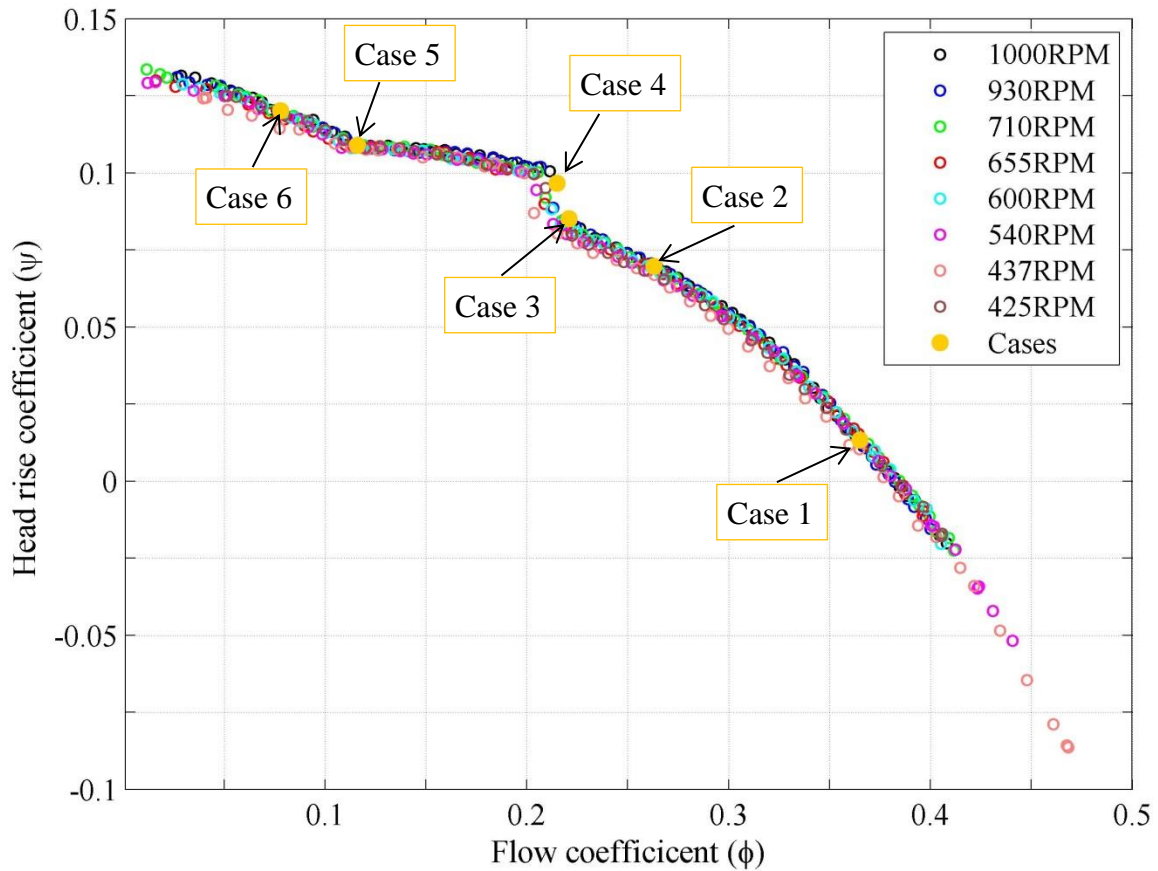


**Figure 3-2 Non-dimensional performance curves - 3 blade Fan.**

Note that Cases selected for future study are shown in the plot

A discontinuous “jump” in the  $\psi(\phi)$  condition is observed for  $\phi \approx 0.31$  in Fig. 3.1. A similar “jump” was observed for the three blade fan, albeit a positive increase in  $\Psi$  as a function of the decreasing  $\phi$  was observed in those results. In both cases (three and nine blade fans), it is initially assumed that the “jump” is associated with a blade-stall (large scale flow separation) condition on the suction surface of the blade. The hot-wire measurements (see section 3.2) will be used to directly assess this assumption.

As noted in Fig. 3.1 and Fig. 3.2, six cases for each blade configuration have been selected. The following descriptive comments refer primarily to the 9-blade configuration. Case 1

represents a very low pressure-rise with a large mass flow rate. Case 2 represents a moderate pressure rise which could represent a typical “system design” condition. Case 3 is the operating condition just before the fan transitions to the stalled condition. It is interesting to note that, Case 3 is quite unstable. It was difficult to sustain this condition for the 95 seconds data acquisition.

Data were collected for each RPM condition at the same nominal  $\psi$  and  $\phi$  values. Therefore, Case 1 through Case 6 are the non-dimensional cases for all of the RPM conditions studied.  $\psi$  and  $\phi$  values of each case for both the three and nine blade configurations are provided in Table 3-1.

**Table 3-1  $\psi$  and  $\phi$  values of Case 1 through Case 6 - 3 and 9 blade fans**

		Case 1	Case 2	Case 3	Case 4	Case 5	Case 6
9 blade fan	$\psi$	0.257	0.218	0.210	0.250	0.199	0.024
	$\phi$	0.492	0.357	0.313	0.290	0.177	0.075
3 blade fan	$\psi$	0.1201	0.109	0.096	0.085	0.069	0.013
	$\phi$	0.365	0.263	0.221	0.215	0.116	.0780

## 3.2 Wake results

Wake measurements were made at the mid-span ( $r/r_{tip} = 0.83$ ) for different RPM conditions to evaluate the effect of the velocity scale (i. e. Reynolds number) on the wake pattern.

Recorded signals of the RPM sensor (synchronized with other measurements) were used to distinguish each fan revolution from which positions of the blades can be obtained for each instant of time. Using the RPM sensor signal, a velocity signal was then divided into subsets that each corresponds to a complete revolution. Ensemble averaging between subsets (i.e. between revolutions) was taken. As an example, at 1000 RPM, phase averaging was performed by collecting data from 1583 revolutions ( $N = 1583$ ). Also, it is noted that each revolution had 4200 discrete velocity values. The maximum number of revolutions ( $N$ ) and the data points in each revolution varies by the fan rotational speed. Obviously, higher RPM conditions have a higher number of revolutions, but fewer data points in each revolution since the measurements have been collected at the same rate (70 KHz) and for the same duration (The number of samples was the same for all data sets).

### 3.2.1 9 blade fan

Figs. 3.3-8 demonstrate the phase averaged velocity normalized by the tip velocity as a function of the spatial phase. It is interesting to note that, the collapse of the normalized data indicates the wake pattern is quite independent of the Reynolds number. The suction and pressure side of the second blade have been shown in each case. Note that, the pressure side is the one the hot-wire sensor first meets. A boundary layer shape can be seen for the pressure side for almost all of the cases. However, it is instructive to note that the measured velocities are the magnitudes of the velocity vectors which incorporate the axial and the tangential components.

It is also quite interesting to look at convergence of the mean data for different cases provided in Appendix B. The statistics naturally converge sooner for an attached flow and later for separated flows in which the flow is highly unsteady and unpredictable.

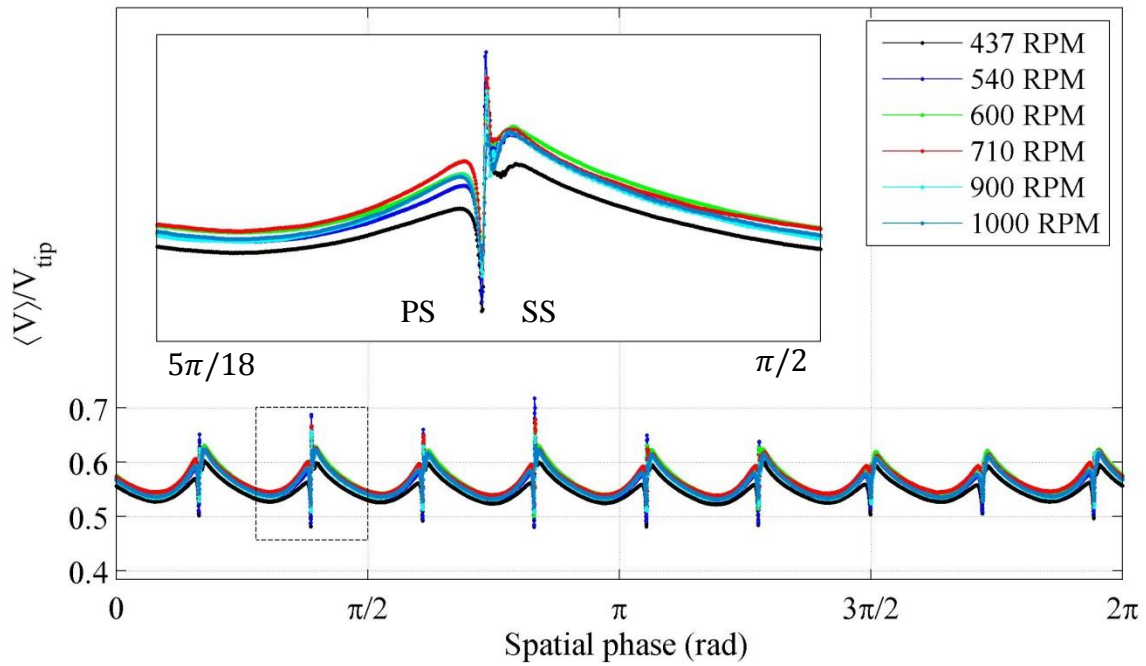


Figure 3-3 Phase averaged mean velocity, Case 1 - 9 blade fan

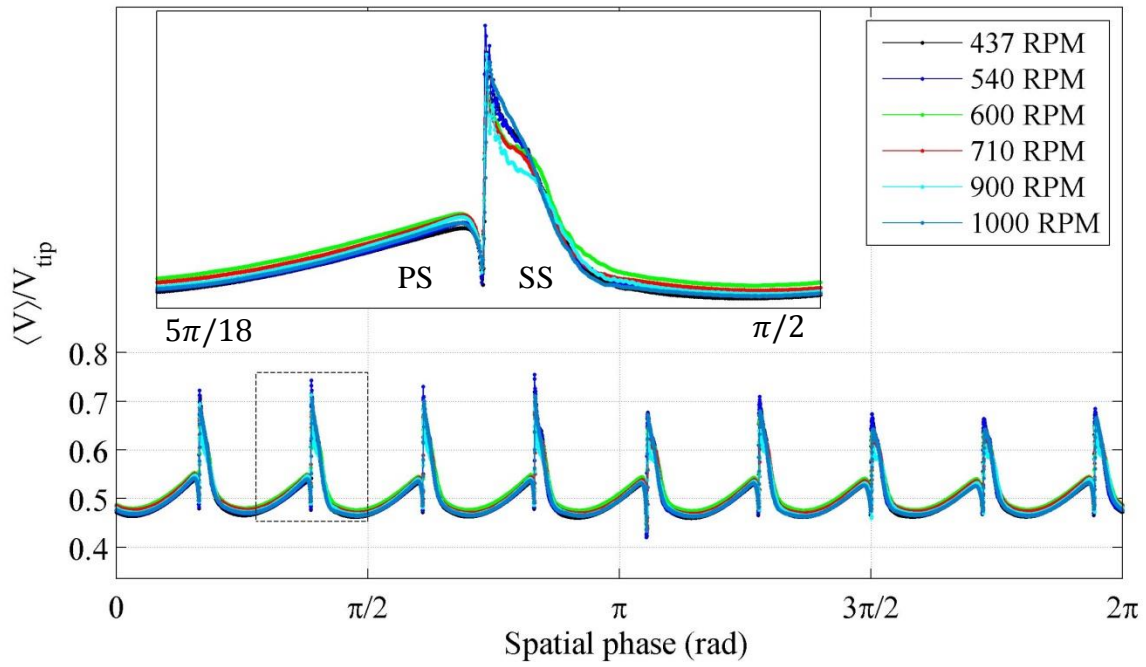


Figure 3-4 Phase averaged mean velocity, Case 2 - 9 blade fan

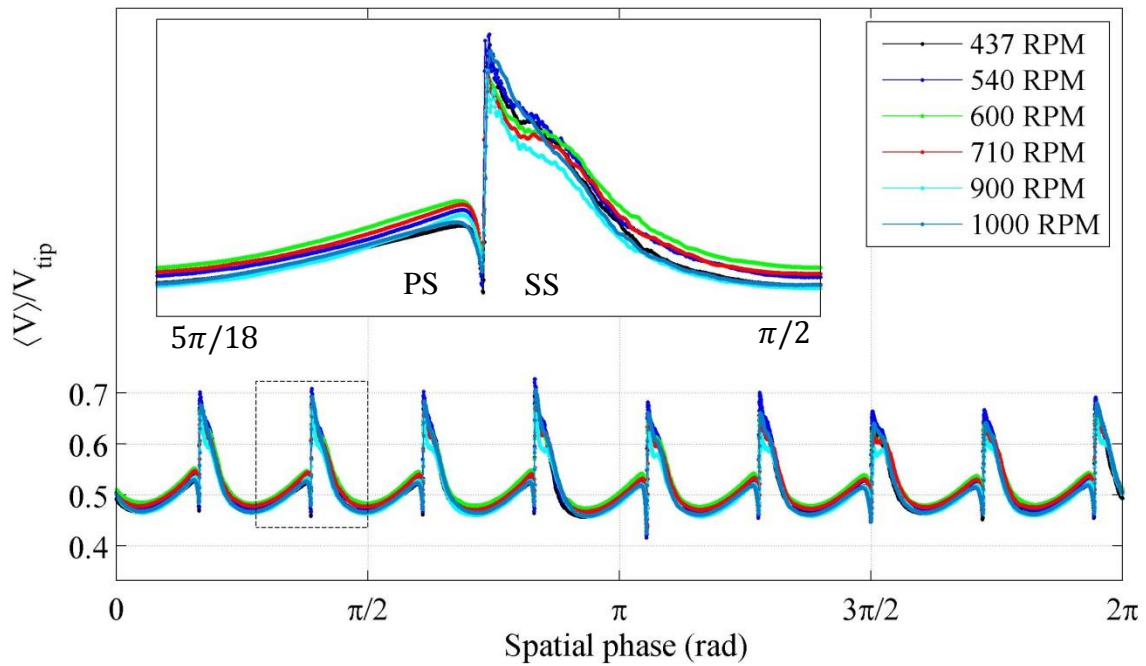


Figure 3-5 Phase averaged mean velocity, Case 3 - 9 blade fan

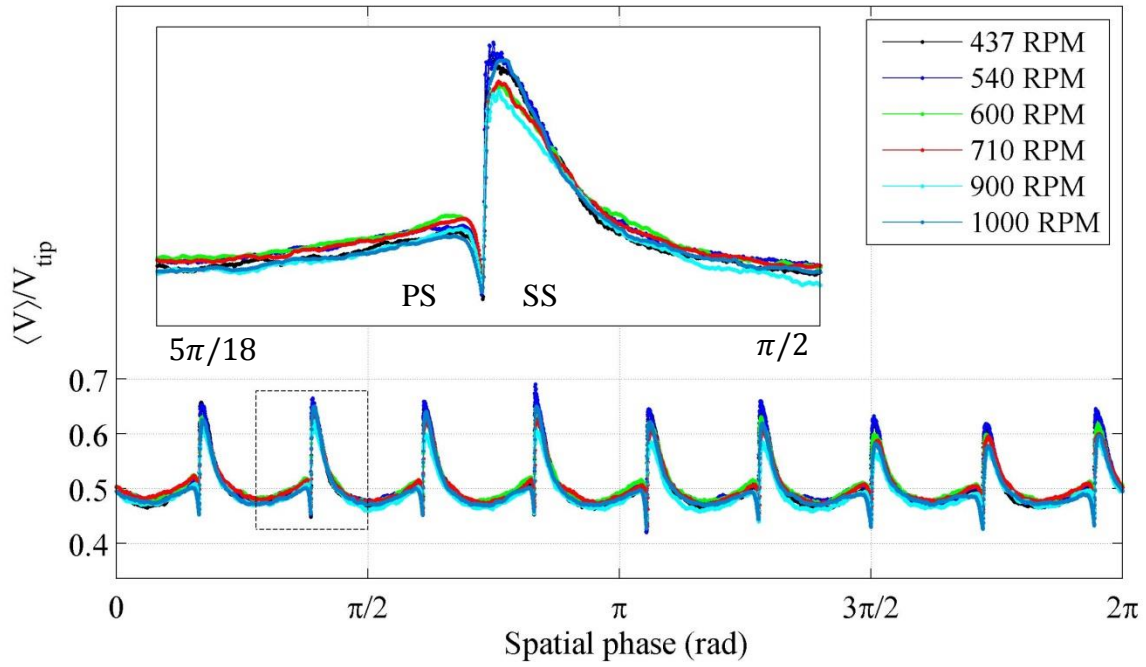


Figure 3-6 Phase averaged mean velocity, Case 4 - 9 blade fan

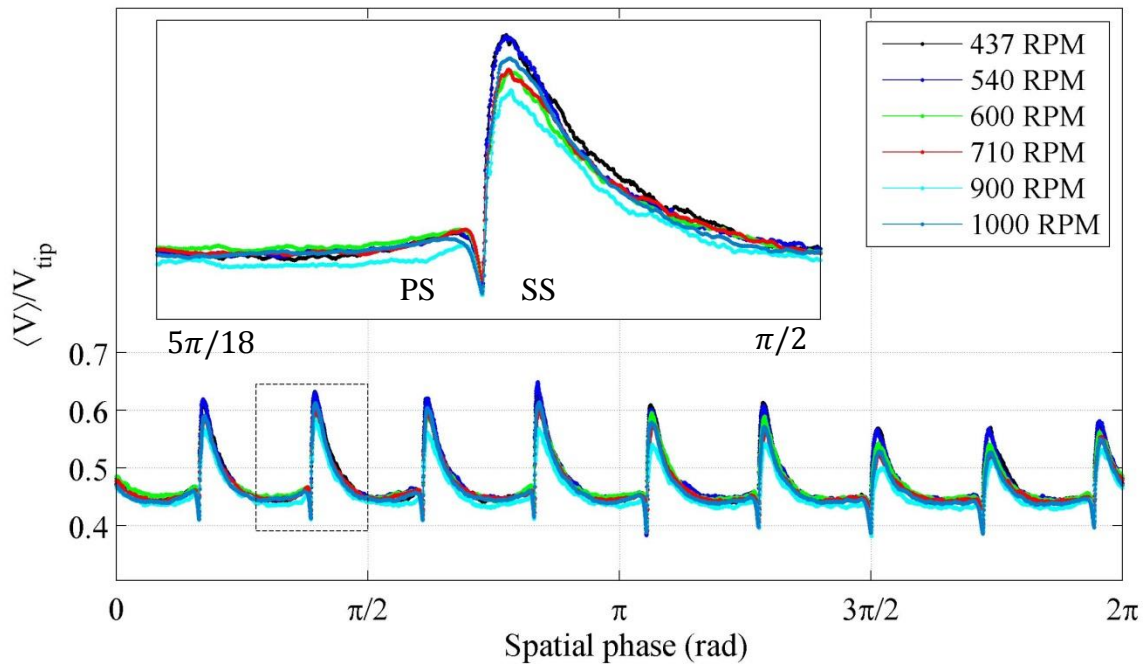
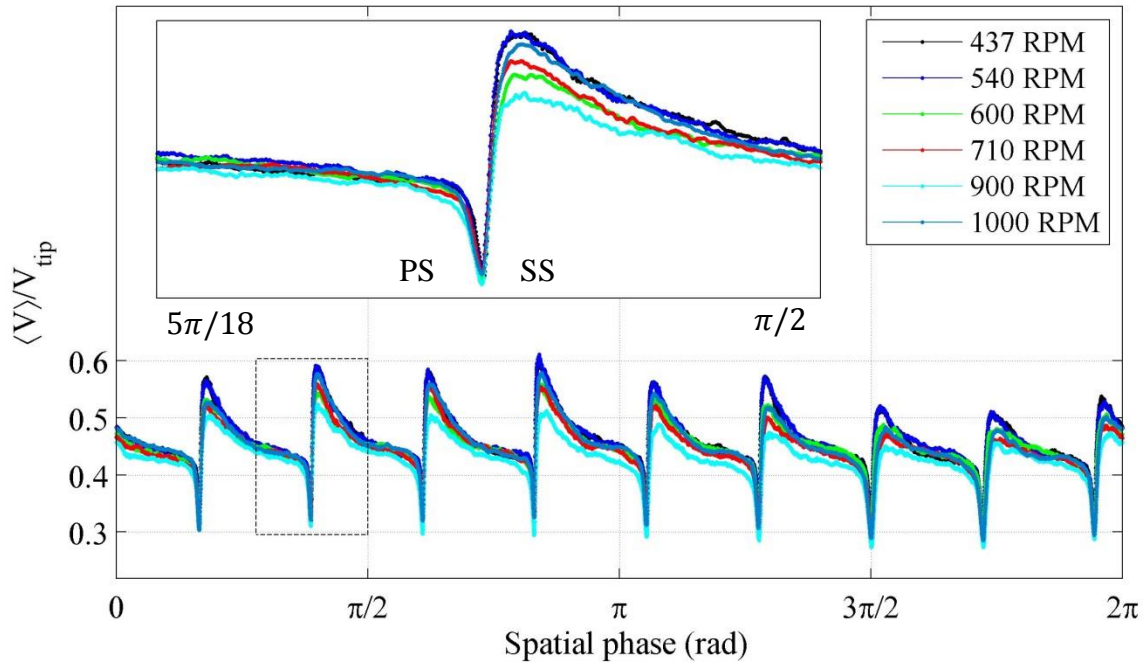


Figure 3-7 Phase averaged mean velocity, Case 5 - 9 blade fan



**Figure 3-8 Phase averaged mean velocity, Case 6 - 9 blade fan**

As noted, Case 1 and Case 2 represent relatively narrow wake regions. The magnitude of the measured velocity in the wake region for each blade is influenced by the distance of the hot-wire from the blades' trailing edge. The blades' trailing edges are not exactly in the same plane (up to 2 mm height differential), and this effect is evident in the velocity measurements.

The time-series hot-wire data have also been processed to represent the turbulence intensity ( $v'_{rms}$ ) distributions in the wake region. The measurement locations were expanded to include different radial locations in the downstream region of the fan at 1000 RPM (the highest investigated RPM condition). Five radial locations were selected starting from hub to tip. The radial locations of the hot-wire probe are provided in Table 3.2. Note that,  $r_{hub}/r_{tip} = 0.65$ .

**Table 3-2 Radial locations for hot-wire anemometry**

	$r/r_{tip}$				
Hot-wire probe radial location	0.707	0.77	0.83	0.89	0.96

Contours of turbulence intensities normalized by  $V_{tip}$  for cases 1-6 are provided in Fig. 3.10:

Case 1 represents a low level of turbulence intensity in the passage ways between the blades, and a very narrow wake (small  $\delta\theta$ ) can be identified where the turbulence intensities are elevated. The elevated levels are understood to be the effect of shearing in the upstream boundary layer that has translated into the wake region. The incidence angle (provided in Fig. 3.9) also supports the idea of the attached flow since it varies between 6 to  $-10$  degrees from hub to tip. It is instructive to note that the elevated intensity levels are present at the outer perimeter which suggests a “tip clearance flow”. Note that these elevated levels of the tip clearance flows are seemingly not attached to the blades.

Case 2 introduces a distinct “wake effect” where the elevated levels are attached to the blades with the strongest presence closer to – but not at – the hub. An elongated (with respect to Case 1) region of the tip clearance flow is evident in Case 2. This is expected since the pressure differential across the fan, which drives the tip flow, has increased considerably from Case 1 to Case 2.

The flow near the tip is suggested to be an attached flow, since it has lower wake thickness and a moderate angle of incidence ( $\approx -3^\circ$ ). Note that, a very thin boundary layer on the pressure side of the blade is suggested by the data ( $< 0.8mm$ ) for almost all of the cases.

Case 3 shows the enhanced tip clearance flow as well as the separated flow regions. A very large wake thickness is apparent which corresponds to a large flow separation flow in the suction side. As the wake region increases, one can postulate that the point of separation is moving toward the leading edge, and the wake area is expanding. The presence of an enhanced tip flow suggests a separation of the boundary layer near the tip.

Case 4 (post stall), with a very similar mass flow rate as that for Case 3 but with a distinct decrease in pressure rise, shows a strong change in the turbulence intensity distribution comparison to that of Case 3. It is noteworthy that the decrease in the  $\psi$  value and the increase in the turbulence intensity suggests that the input power to the fan has shifted from useful “flow work” to dissipative effects. The balance of images in Fig. 3.10 are also compatible with the small changes in characteristic curve values for  $\psi(\phi)$ .

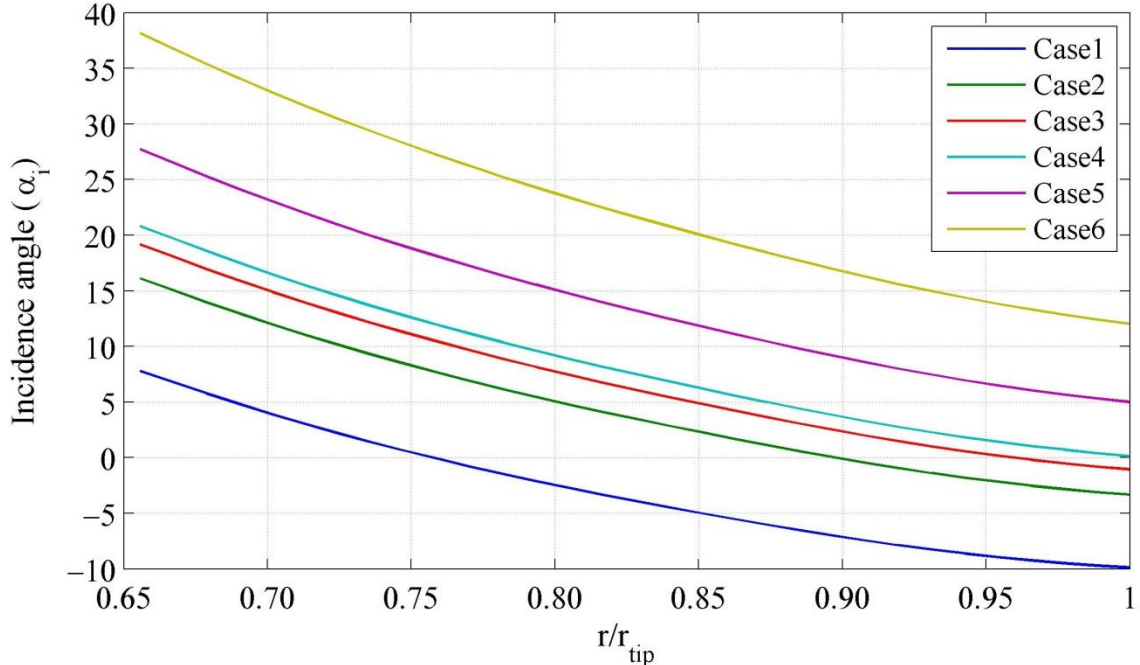


Figure 3-9 Incidence angles for different span locations - 9 blade fan

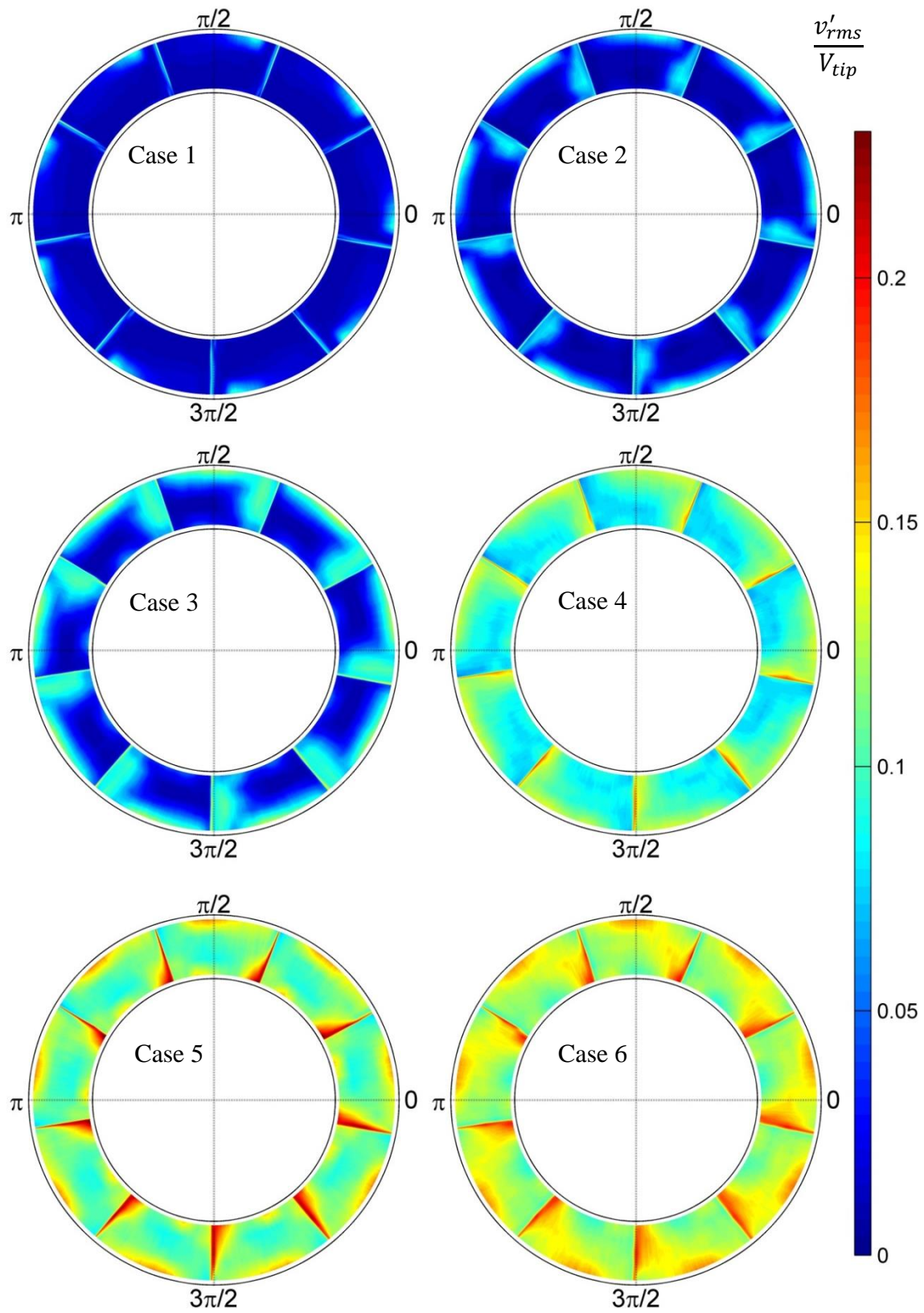


Figure 3-10 Turbulence intensity contours, Case 1 through Case 6 - 9 blade fan

The abrupt pressure drop between case 3 and 4 can be interpreted as follows: once the large separation (seemingly separated from or near-to-the leading edge) occupies the blades' passages, the flow cannot easily pass through the blades' passages. This phenomenon is understood to make an abrupt increase in the suction side pressure and naturally a decrease in fan pressure differential. This phenomenon has a similar behavior to airfoil stall.

Cases 5 and 6 represent a deeply stalled condition in which the blades are considered to be bluff bodies. In this condition the blades are essentially pushing the flow without the benefit of significant lift on the blades. It is inferred that separation from leading edge occurs in these cases.

### **3.2.2 3 blade fan**

Similar measurements have been made for the 3 blade fan. The phase averaged mean velocity data are presented in Figs. 3.12-17 and the corresponding turbulence intensities are shown in Fig. 3.18. It is inferred that the flow separates from the leading edge of the blades for Case 2 through Case 6 given the width of the wake region as evident in both the mean velocity and the turbulence intensity distribution. With these observations, it is suggested that the three blade fan is better understood to represent three stalled RCDBs with no beneficial effects of the blade-to-blade interaction.

Considering the blades as separate entities, it is a further observation that the angle of attack (12 degrees larger than the incidence angle shown in Fig. 3.11) better represent the flow physics. For example, for case 1;  $9 < \alpha_g < 28$ .

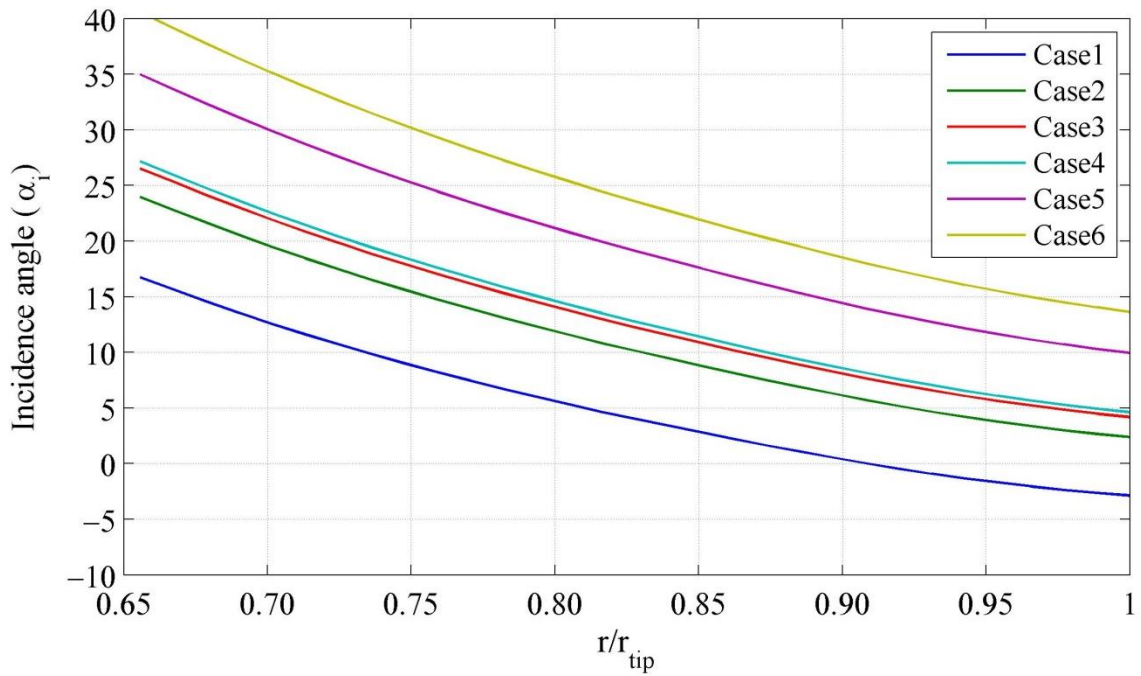


Figure 3-11 Incidence angle - 3 blade fan

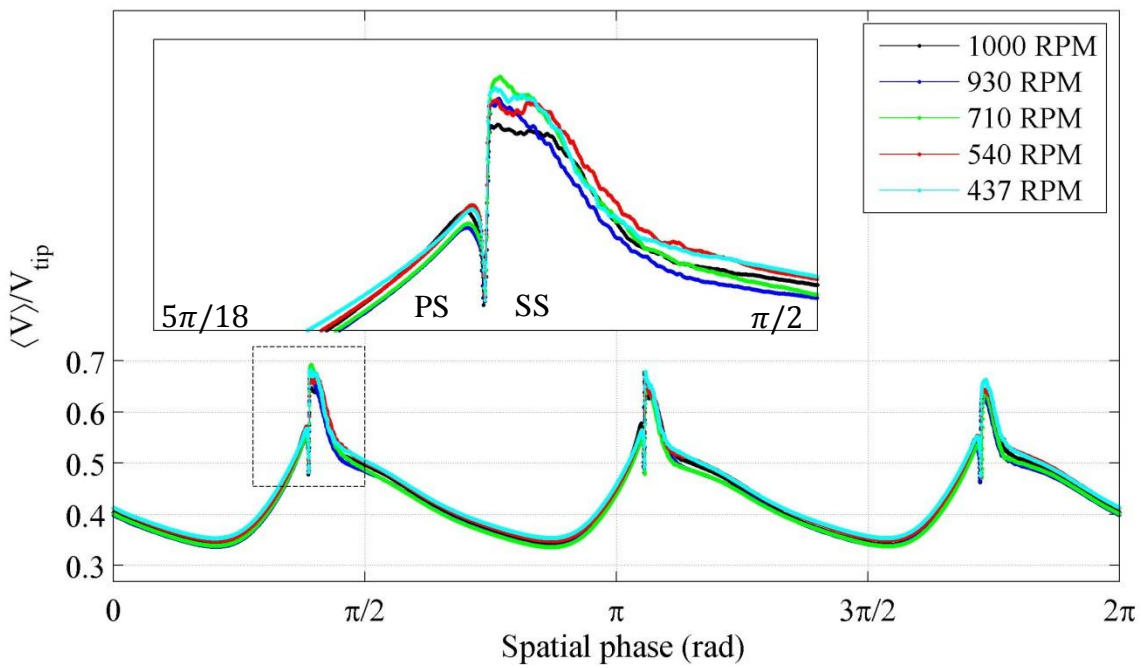


Figure 3-12 Phase averaged mean velocity, Case 1 - 3 blade fan

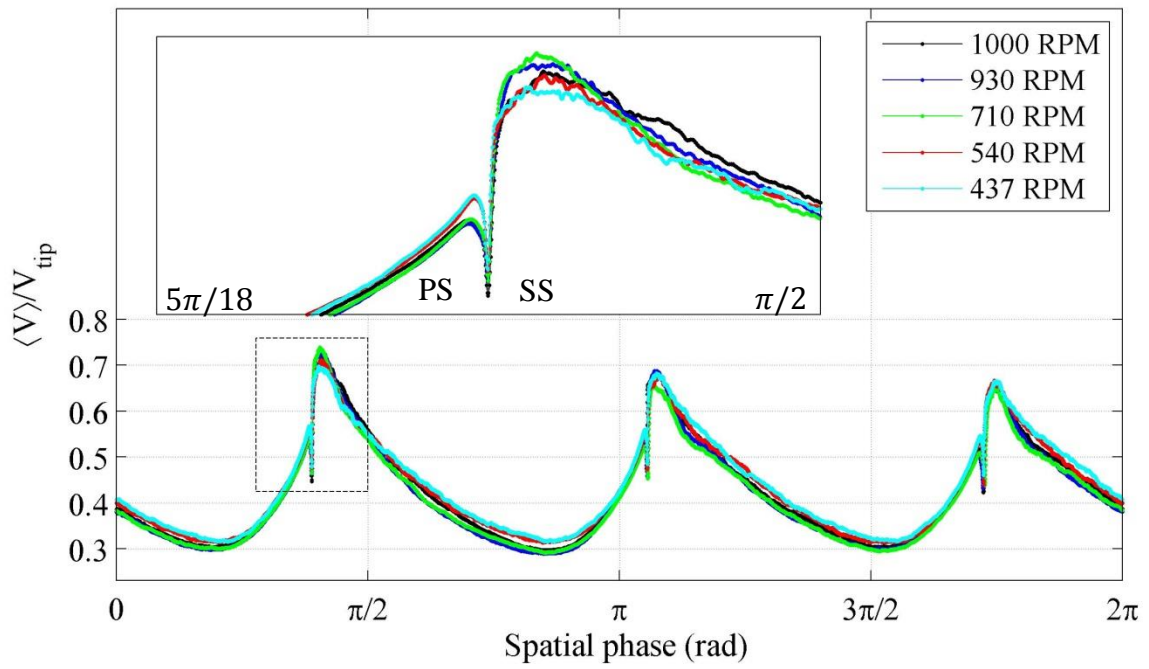


Figure 3-13 Phase averaged mean velocity, Case 2 - 3 blade fan

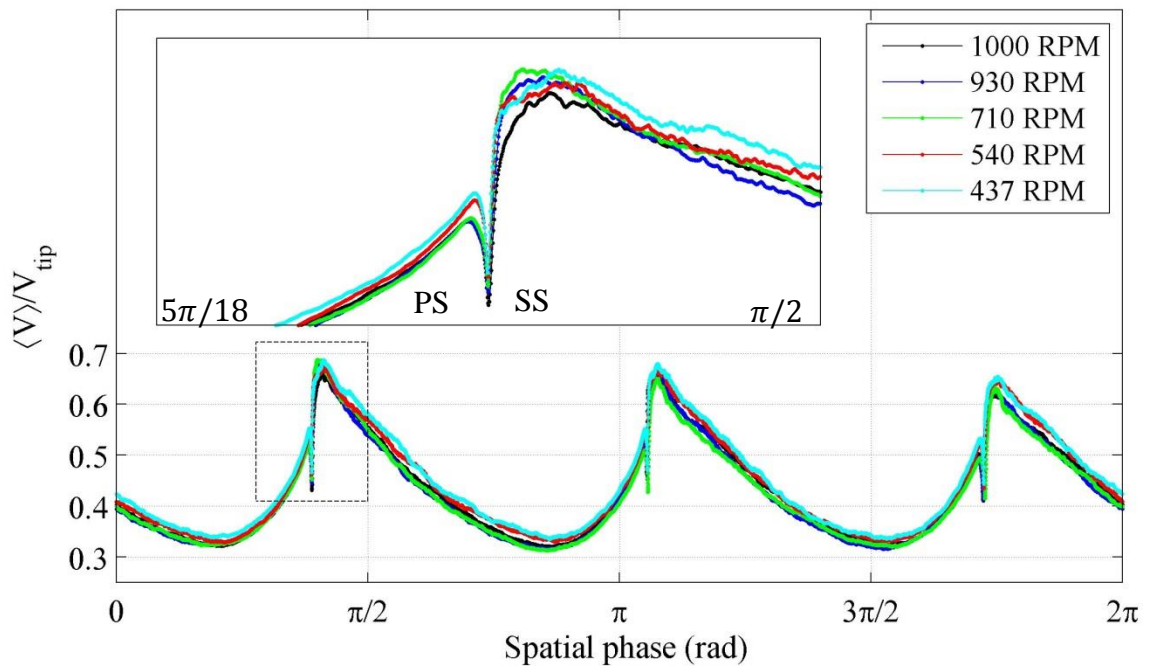


Figure 3-14 Phase averaged mean velocity, Case 3 - 3 blade fan

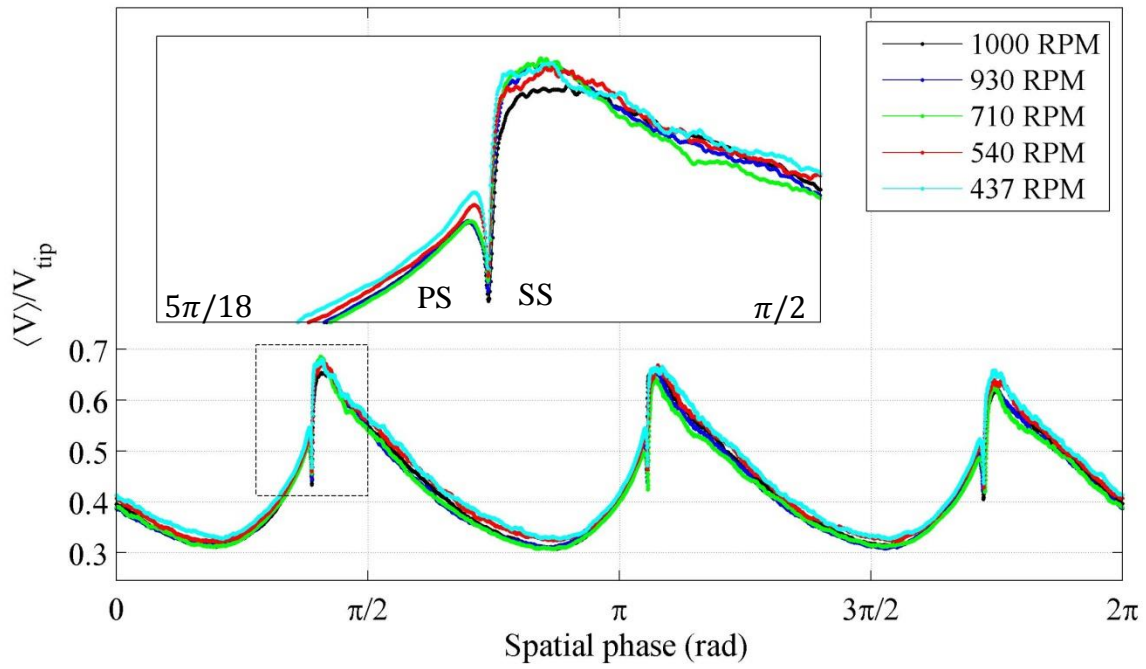


Figure 3-15 Phase averaged mean velocity, Case 4 - 3 blade fan

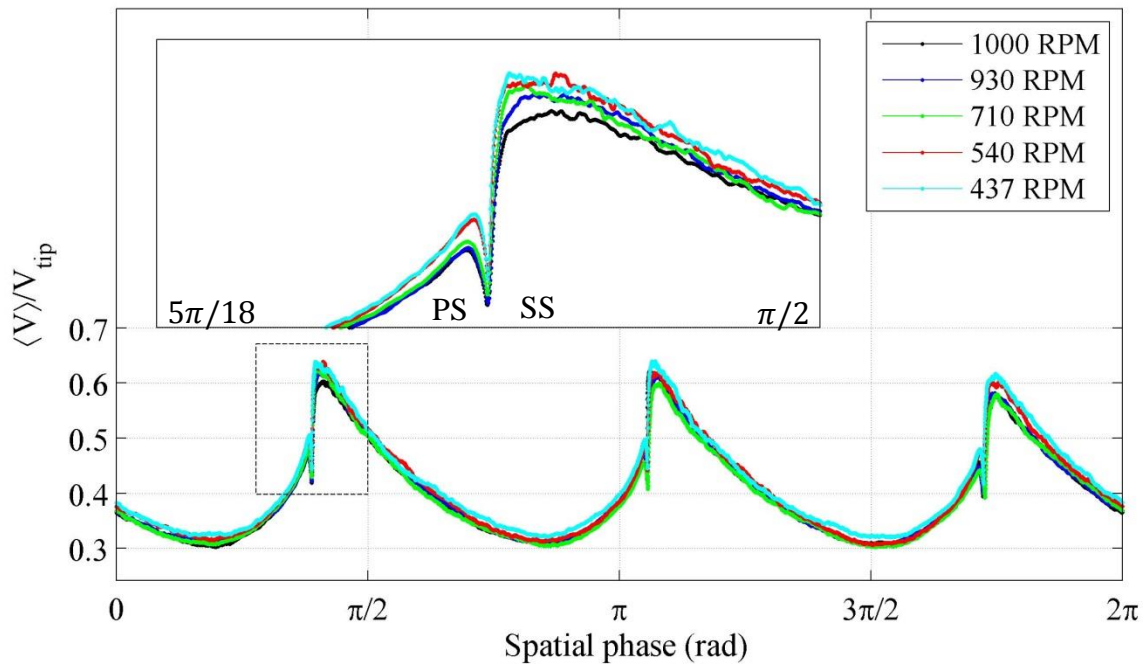
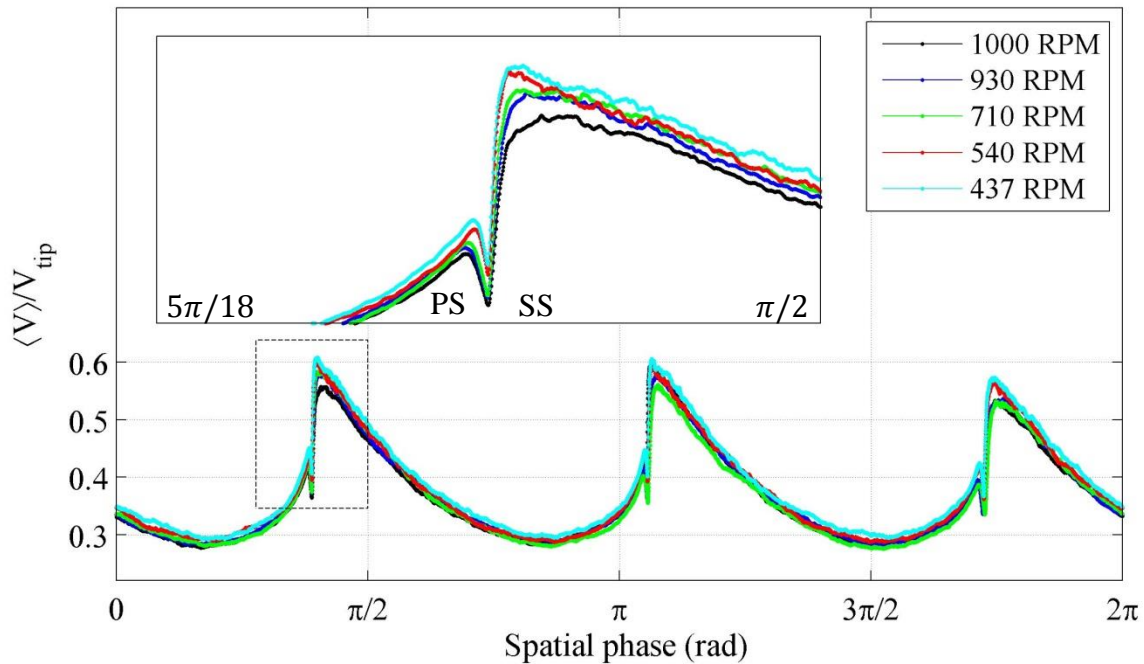


Figure 3-16 Phase averaged mean velocity, Case 5 - 3 blade fan



**Figure 3-17 Phase averaged mean velocity, Case 6 - 3 blade fan**

As anticipated based on the angle of attack, a deeply separated flow was inferred for Case 1 through Case 6. Generally, an angle of attack of  $16^\circ$  leads to boundary layer separation from the suction side for most of airfoils.

Case 1 suggests a separation from the suction side of the blades. Based on the large wake of case 2, one can infer that the flow separates from the leading edge of the blades in this case. Tip flow effect can also be seen similar to the 9 blade fan, but it appears to have more effect on the flow in the blade passages rather than the 9 blade.

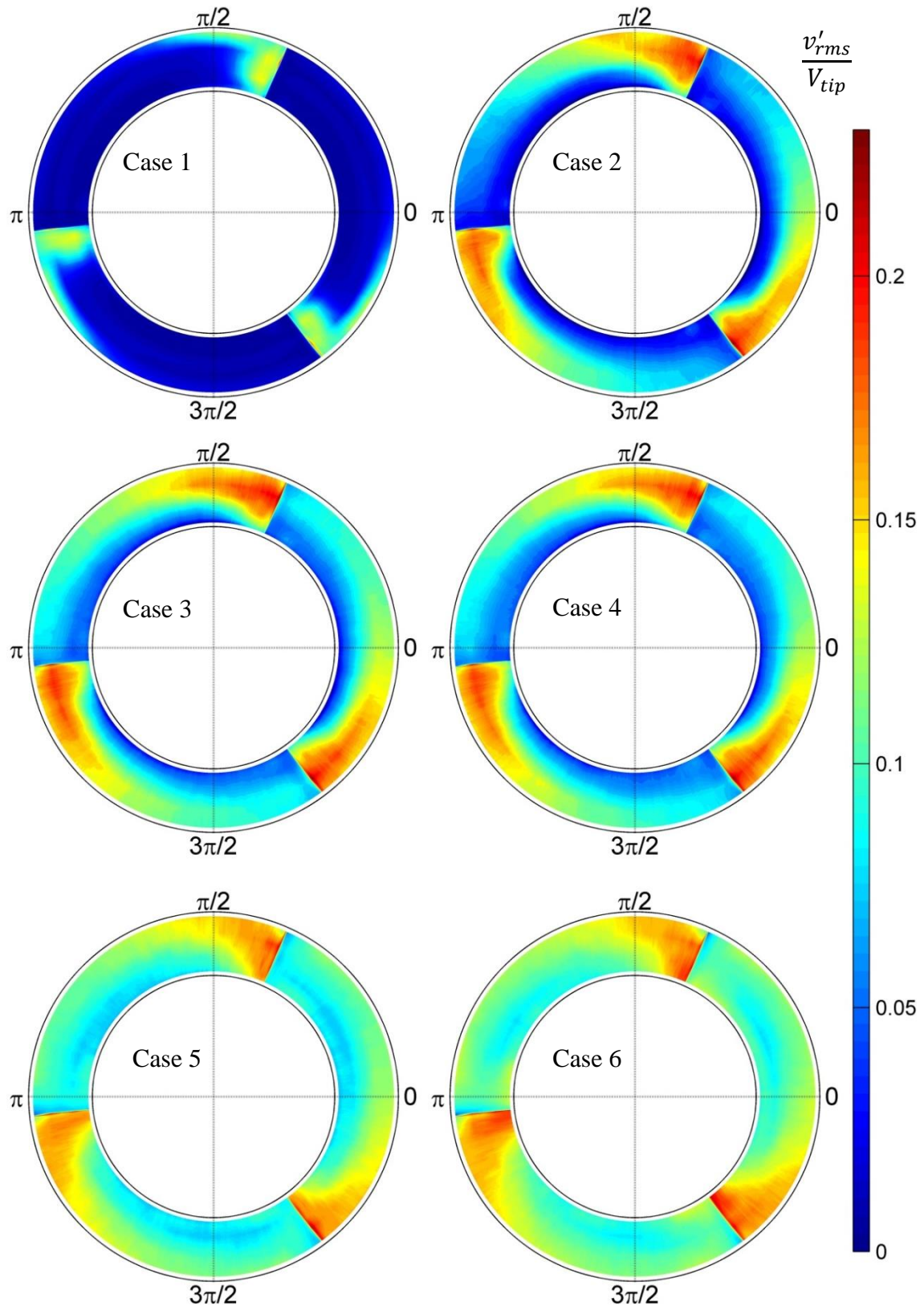


Figure 3-18 Turbulence intensity contours, Case 1 through Case 6 - 3 blade fan

### 3.3 Aeroacoustics results

Aeroacoustics measurements have been acquired for Case 1 through Case 6. The final pressure signal:  $P'(t)$ , obtained from the beamforming technique, has been subdivided into segments for processing by a 50 percent FFT algorithm. The FFT results for the subdivided sections of the  $P'(t)$  signal were then ensemble averaged to produce the spectral representation of the acoustic signature for the given conditions. The experimental data, so processed, are referred to as “Auto-Spectral Density” or ASD. (see Appendix A.1 for its definition)

The number of data points (i.e.  $M$ ) that defines the sub-division process must be rationally selected. The clarity of the spectra depends upon the number of data points ( $M$ ) selected for a given sample time. Specifically, too many points would make a noisy signal, and having too few points may fail to capture the physics of the sound source. The number of data points corresponding to 5 revolutions was selected. Note that, the number  $M$  would change for different rotational velocities.

Acoustic data are presented for the range of 200-8000 Hz. It is instructive to note that most of the ambient noise caused by AC electrical equipment are significant for less than 200 Hz.

#### 3.3.1 9 blade fan

Figs. 3.19-24 demonstrate the auto-spectral density of the radiated noise of the 9 blade fan for different cases. Measurements have been made at each case for different RPM conditions. Thus, the effects of the fan rotational velocity and Reynolds number ( $Re_c = W_\infty C/\nu$ ) can be investigated in these plots. Note that BPF peaks (first one is below 200 Hz) corresponding to 1000 RPM have been shown by vertical lines in Fig. 3.19. They are 300, 450, 600, 750, 900 and 1050 Hz.

The BPF peak magnitudes are diminished for higher integer multiples especially for lower RPM conditions. Also, distinguishing these peaks can be difficult since the first multiples are at frequencies lower than 200 Hz for the lower RPM conditions. For example, BPF for the fifth peak of the 437 RPM condition (which is at 325 Hz) is shown in Fig. 3.19. BPF peaks are also identified for 710 RPM of Case 2 and for 900 RPM of Case 3 in Fig. 3.20 and Fig. 3.21 respectively.

Using Eq. 2.12, sound pressure level (SPL) values for each operating condition have been provided in the legend of each plot. The SPL obtained by Eq. 2.12 represents the range of frequencies for which calibration has been carried out (200-8000 Hz).

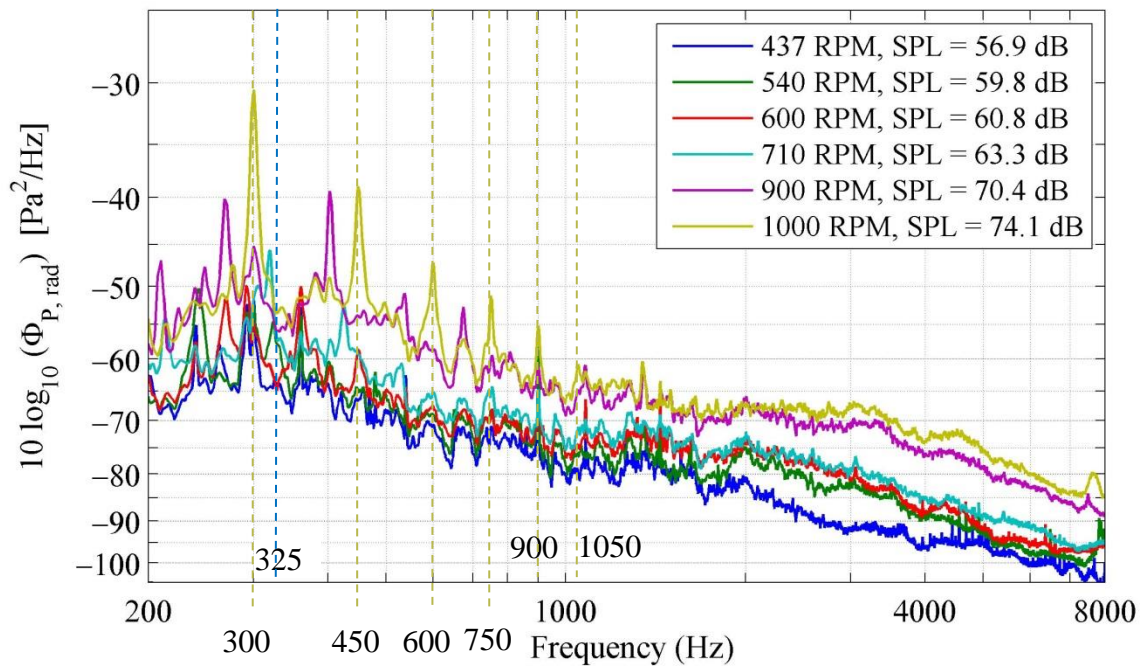


**Figure 3-19 ASDs for Case 1 - 9 blade fan**

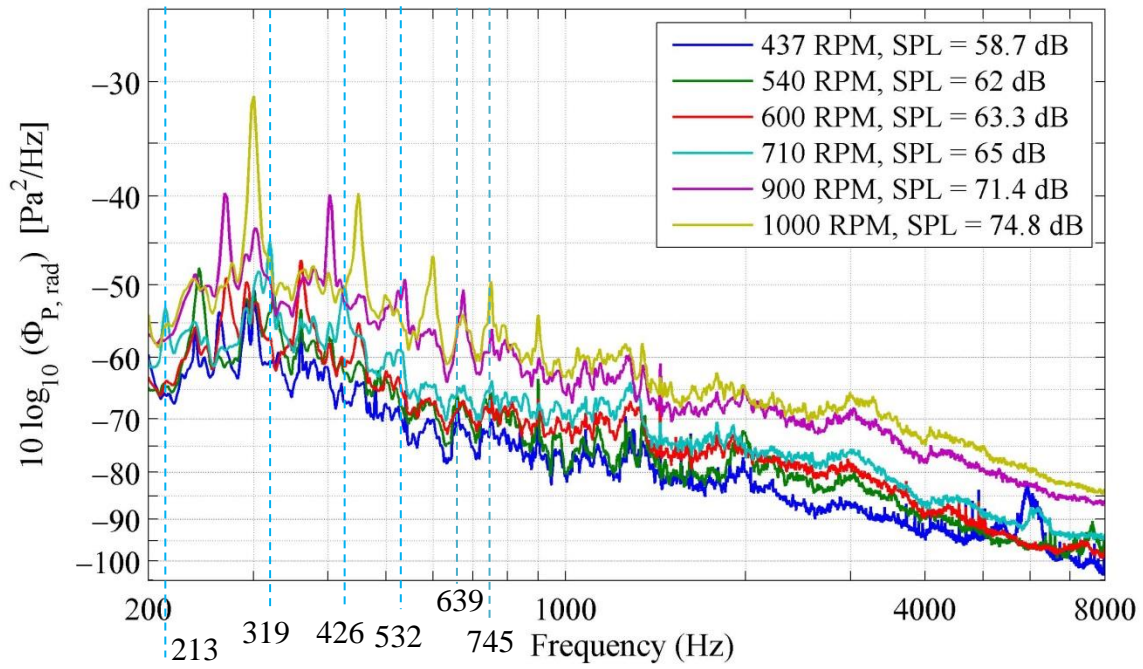


Figure 3-20 ASDs for Case 2 - 9 blade fan

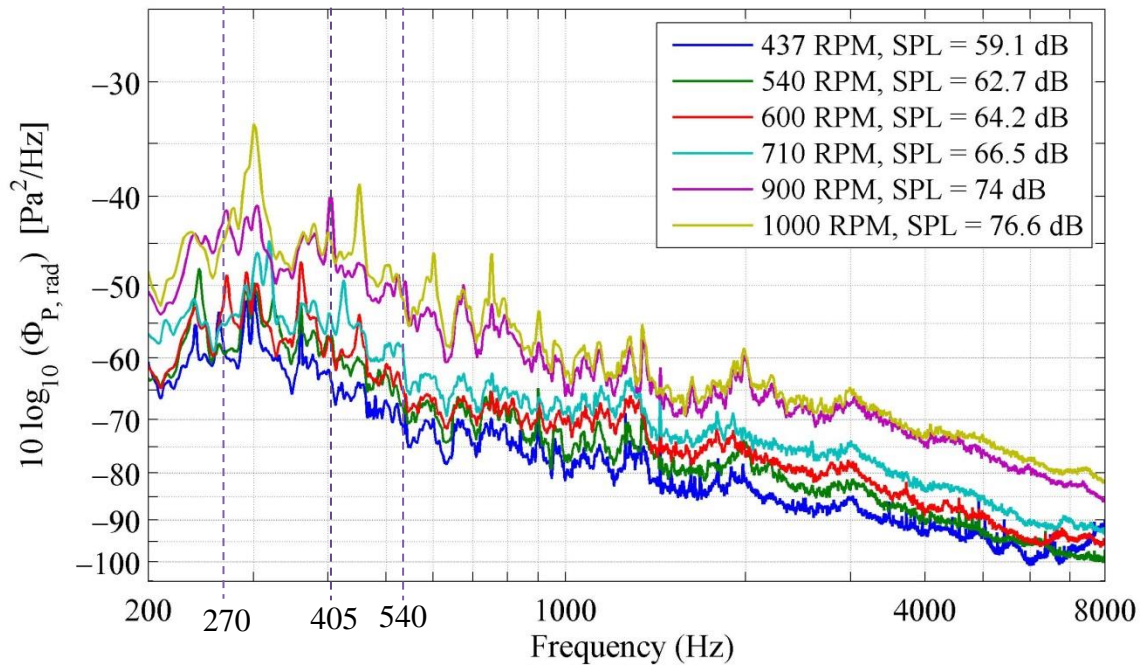


Figure 3-21 ASDs for Case 3 - 9 blade fan

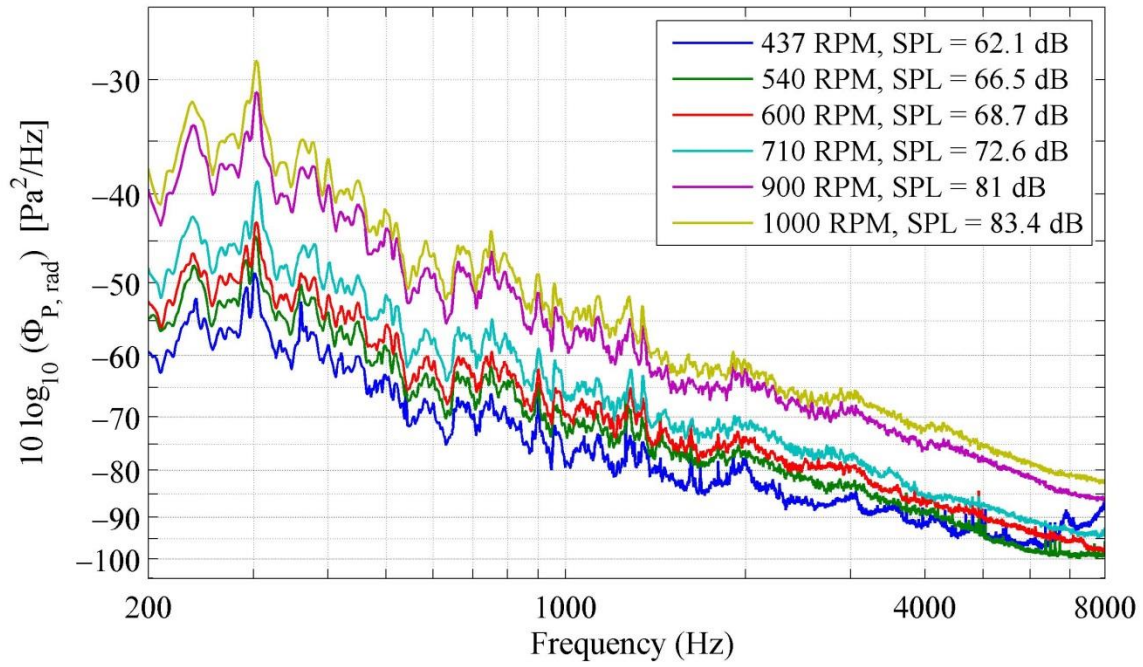


Figure 3-22 ASDs for Case 4 - 9 blade fan

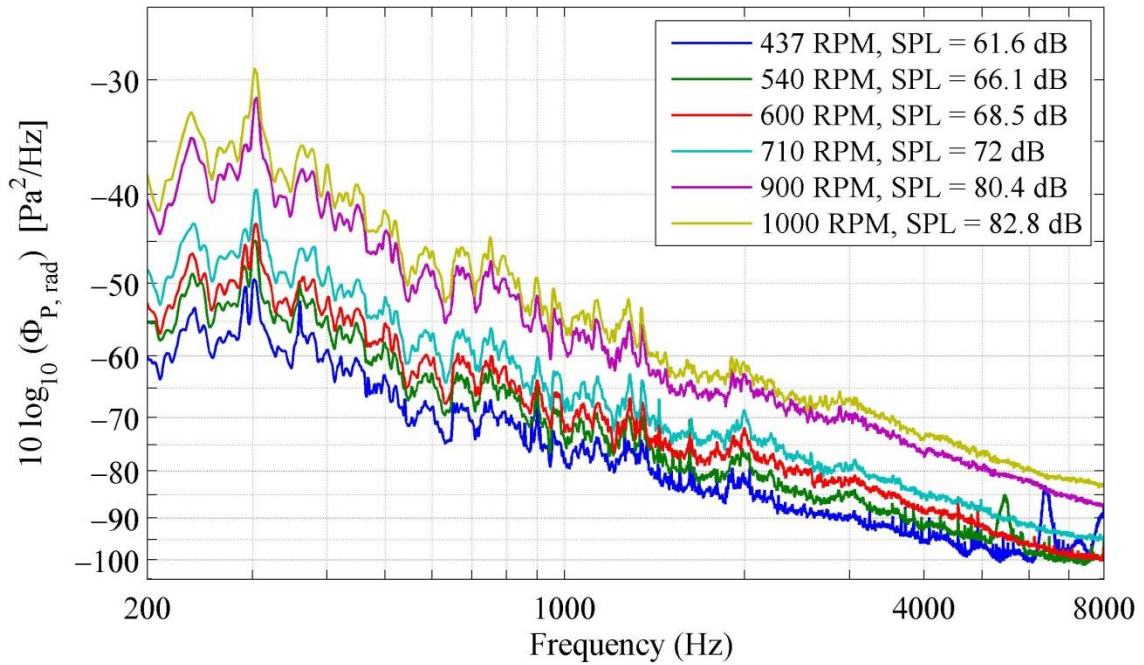
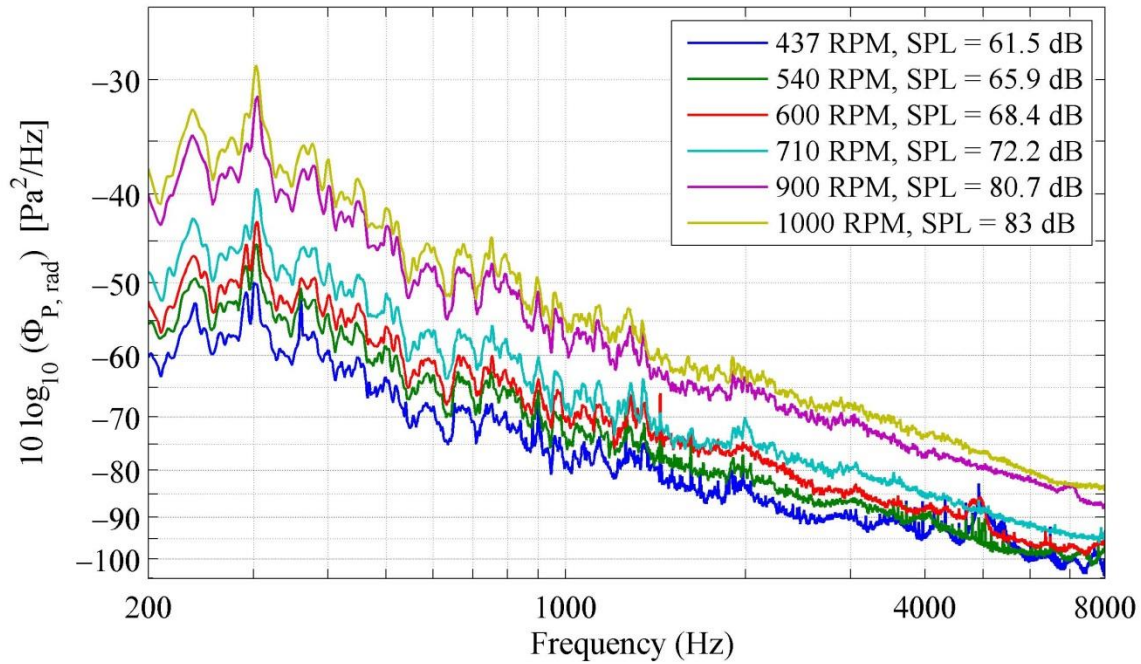


Figure 3-23 ASDs for Case 6 - 9 blade fan



**Figure 3-24 ASDs for Case 5 - 9 blade fan**

As noted, Cases 1, 2 and 3 demonstrated that the peaks in the auto spectral density are displaced to lower frequencies as the RPM condition is decreased. However, Cases 4, 5 and 6 showed that the same pattern but different magnitude for different RPM conditions. Figs 3.25-3.27 show the data from Figs 3.19-21 with normalized abscissas. The abscissas are normalized by the  $V_{tip}$  corresponding to each RPM condition. It is noted that the BPF peaks are aligned in the normalized abscissa as shown by vertical dashed lines in Figs. 3.25-3.27.

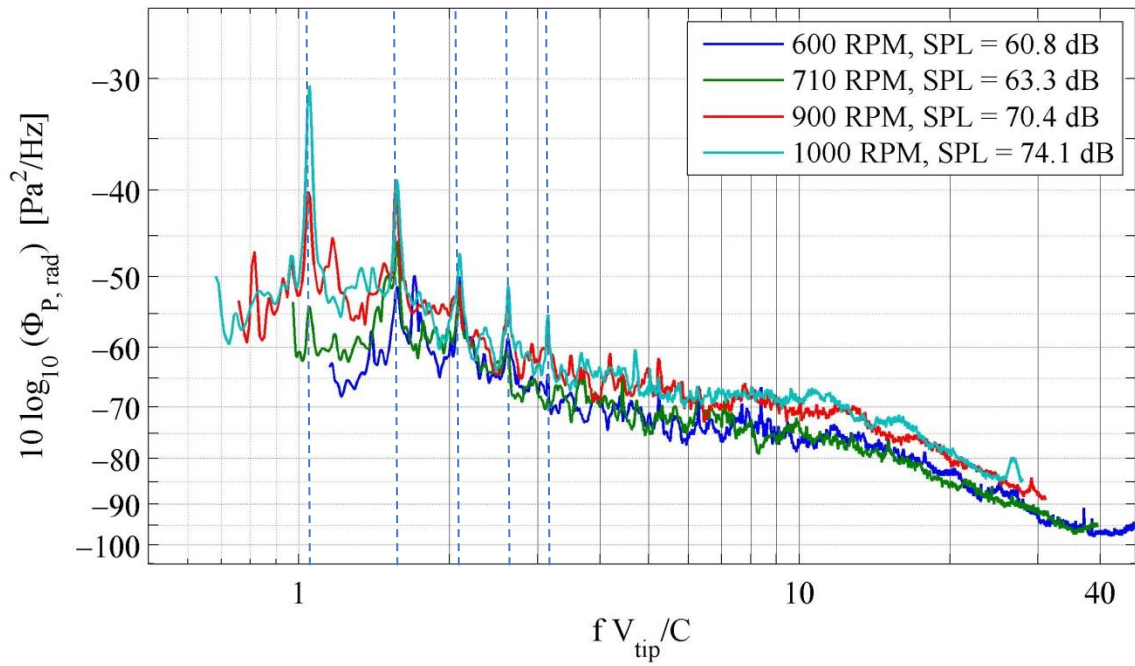


Figure 3-25 ASDs for Case 1 with normalized abscissa - 9 blade fan

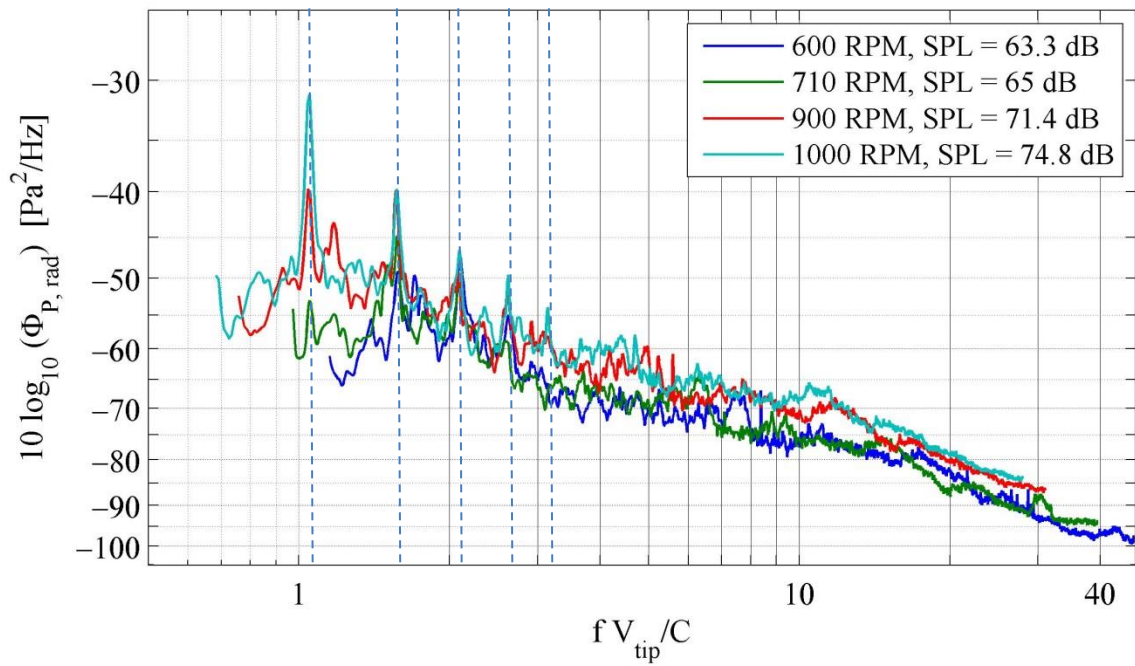
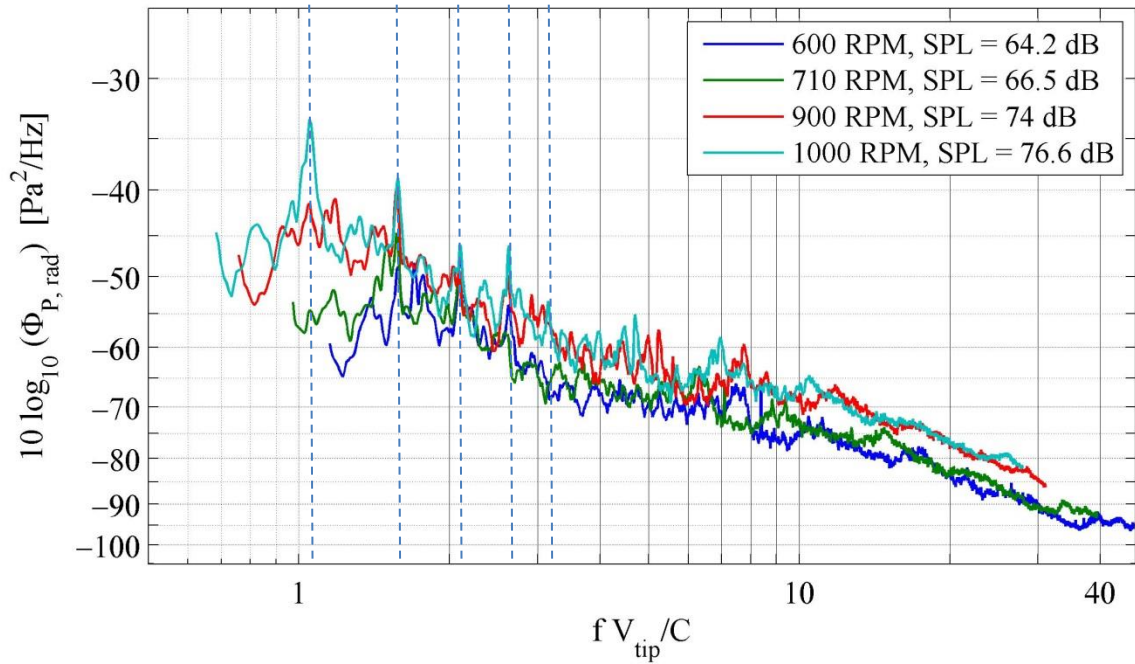
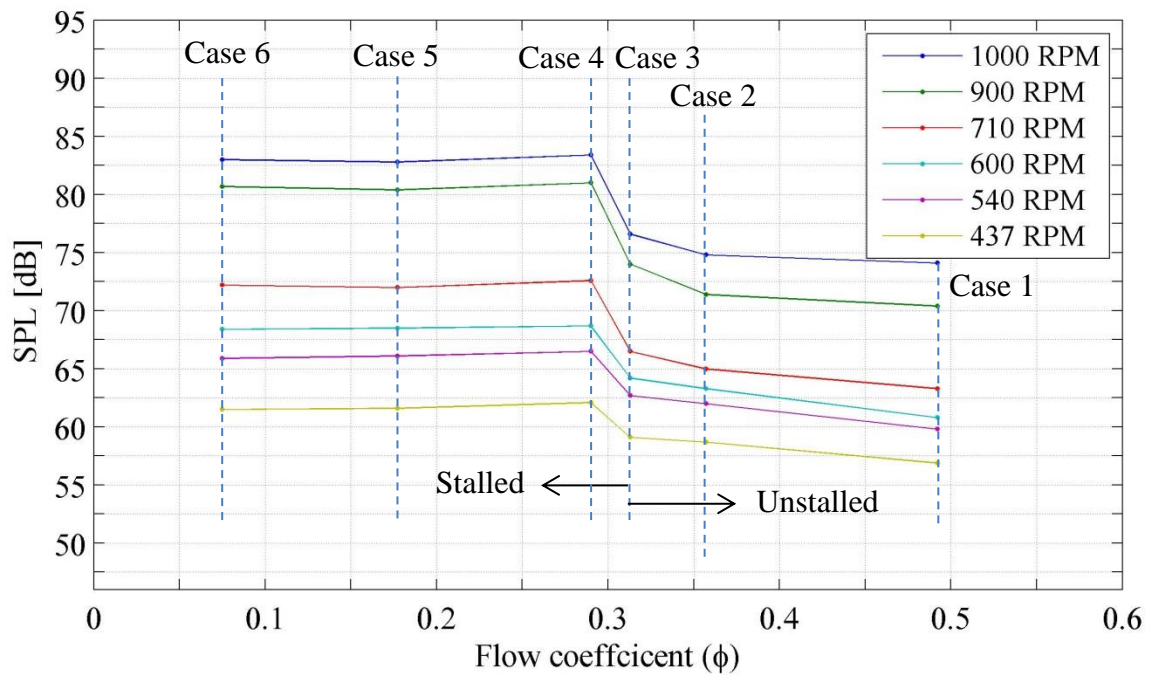


Figure 3-26 ASDs for Case 2 with normalized abscissa - 9 blade fan



**Figure 3-27 ASDs for Case 3 with normalized abscissa - 9 blade fan**

Sound pressure levels as a function of flow coefficient are provided in Fig. 3.28. Noise increase in the stall condition is also evident in this figure. Note that the ordinate is started from background noise which is about 46 dB.



**Figure 3-28 SPLs vs flow coefficient - 9 blade fan.**  
 Note that vertical dashed lines correspond to the defined Cases.

### 3.3.2 3 blade fan

Figs. 3.29-34 demonstrate the auto-spectral density of radiated noise of a 3 blade fan for different cases. Similar to the 9 blade fan, measurements have been made at each case for different RPM conditions. Thus, the effects of the fan rotational velocity and Reynolds number ( $Re_C$ ) can be investigated in these plots

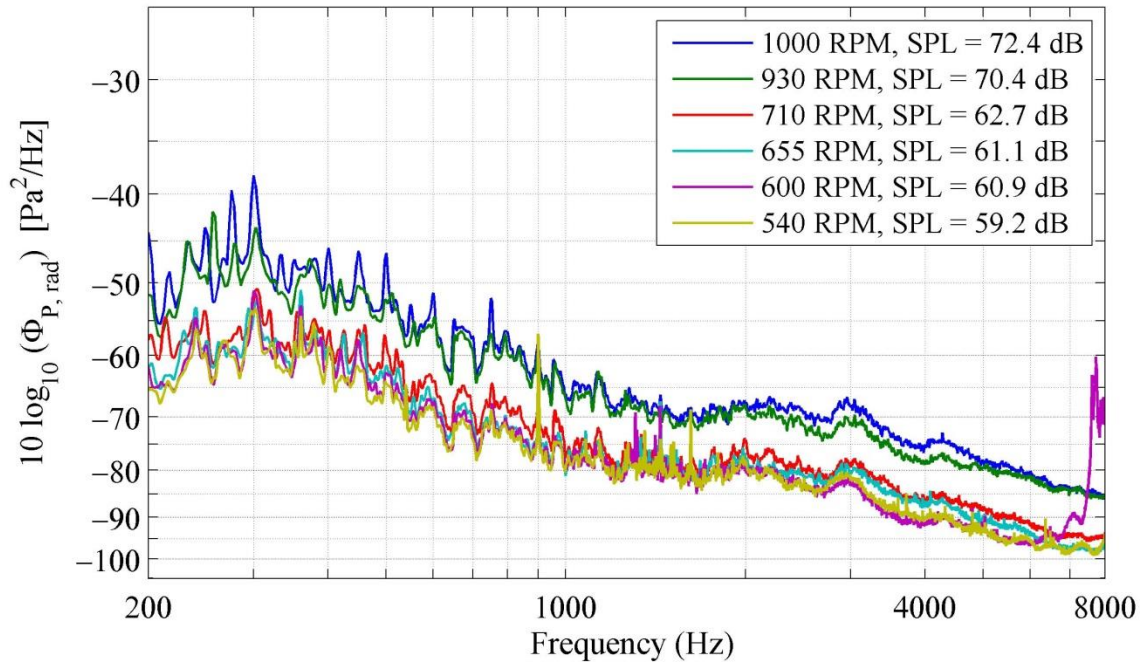


Figure 3-29 ASDs for Case 1 - 3 blade fan

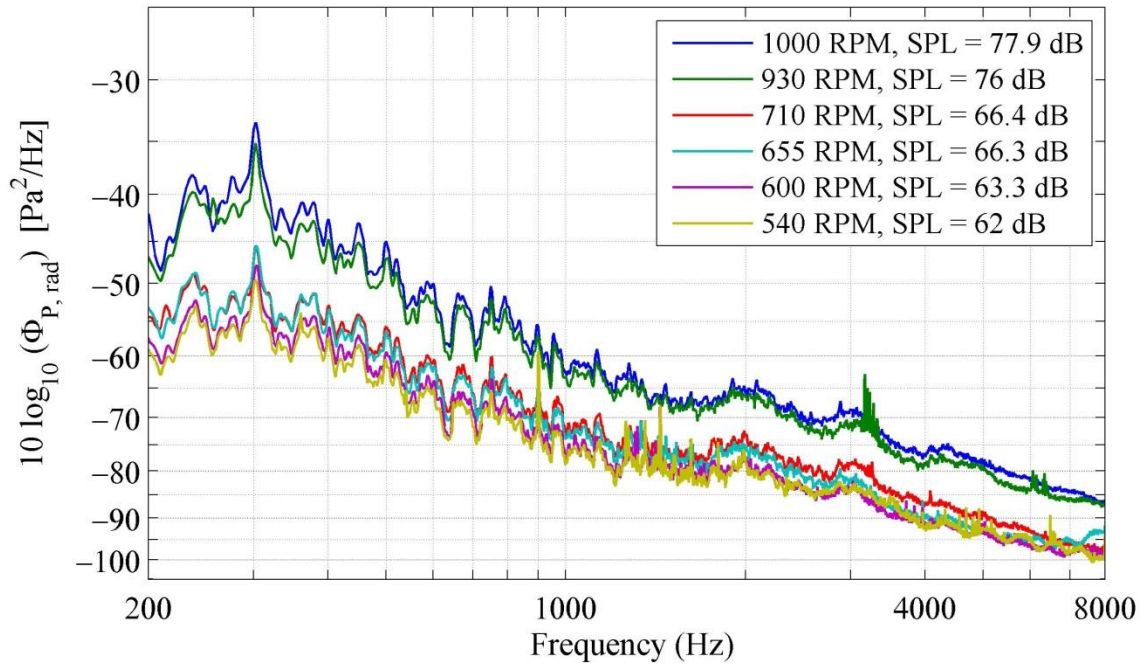


Figure 3-30 ASDs for Case 2 - 3 blade fan

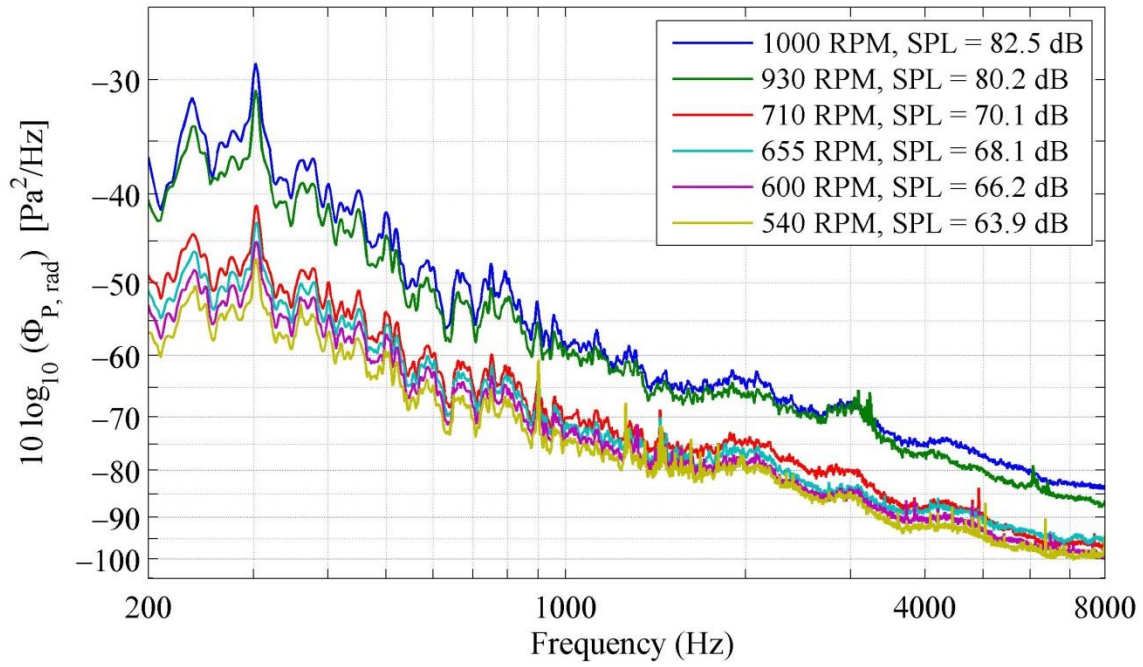


Figure 3-31 ASDs for Case 3 - 3 blade fan

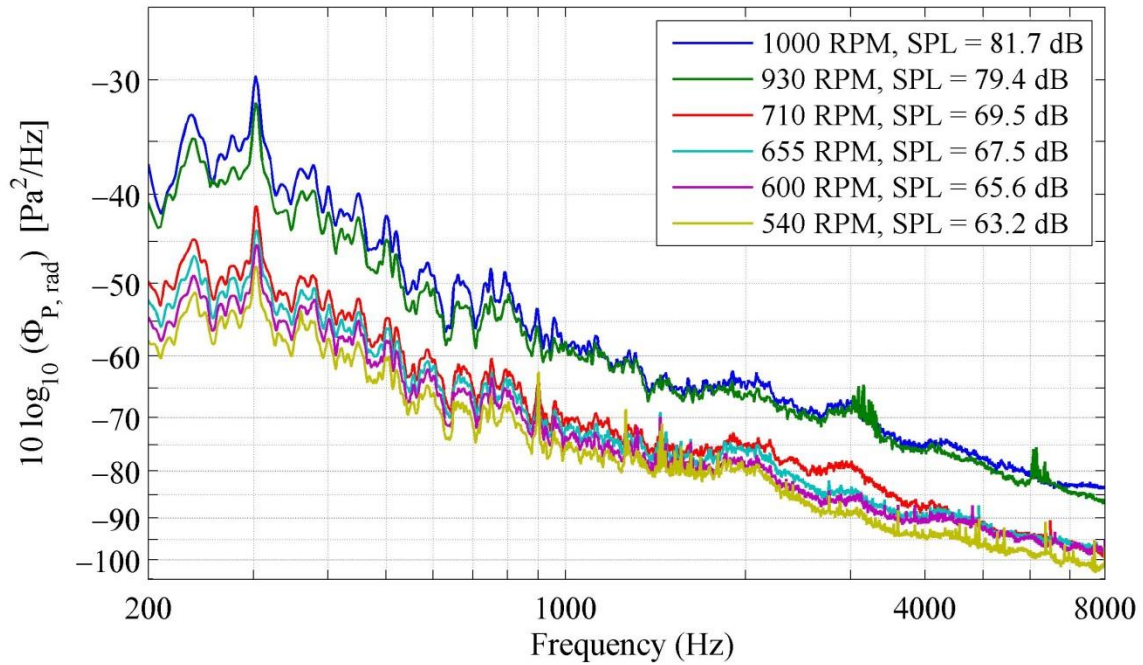


Figure 3-32 ASDs for Case 4 - 3 blade fan

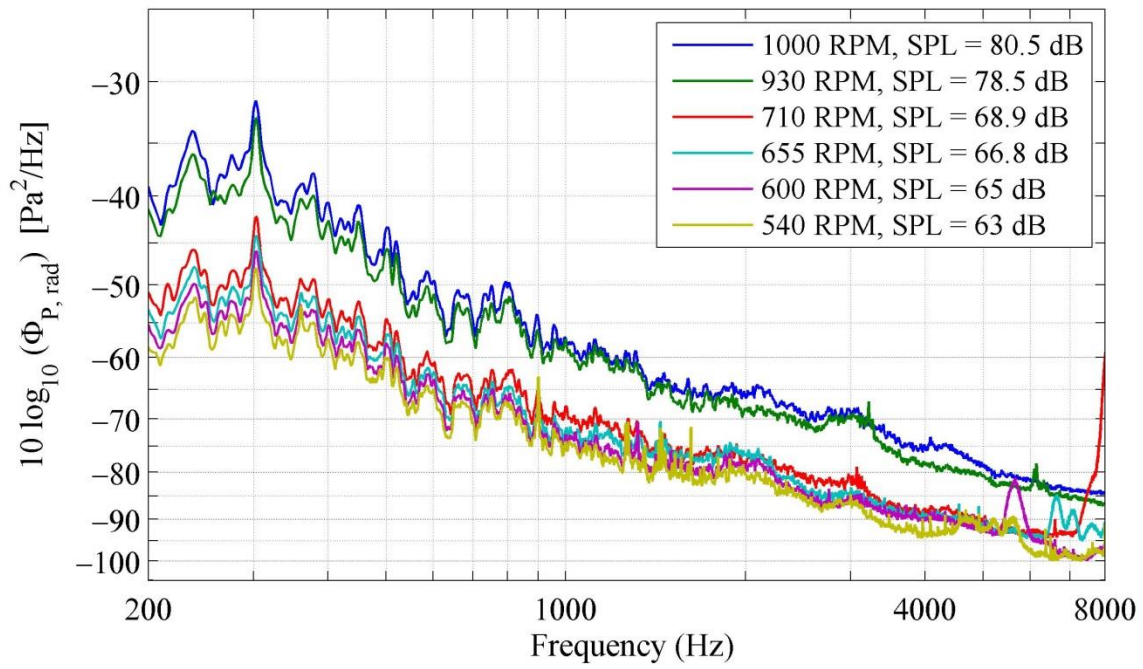


Figure 3-33 ASDs for Case 5 - 3 blade fan

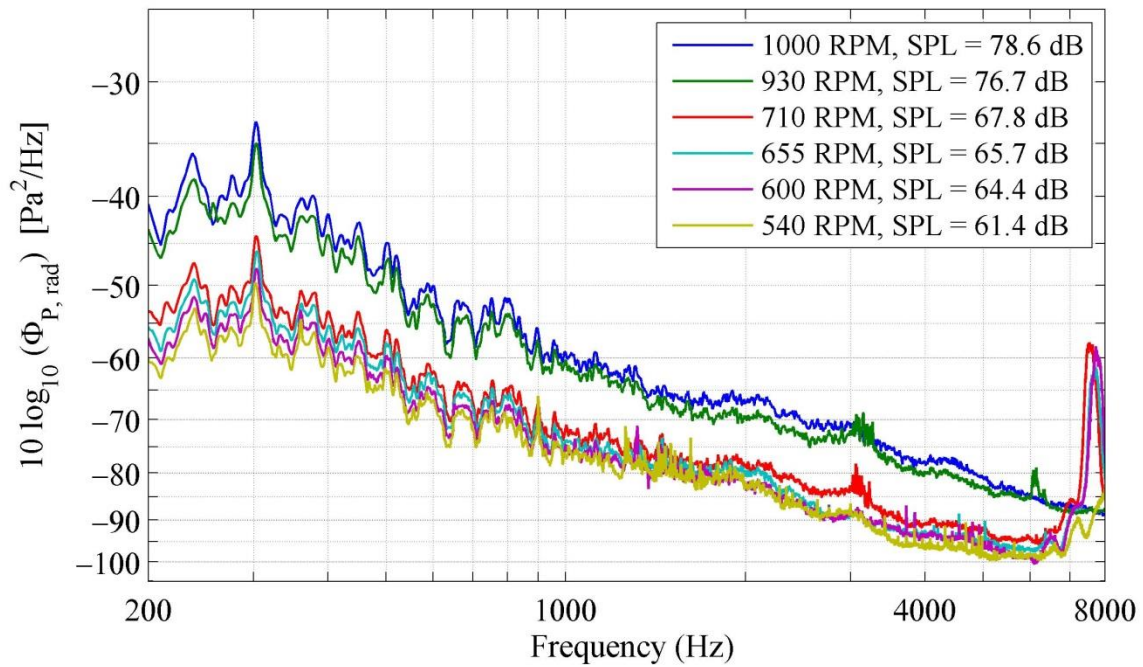


Figure 3-34 ASDs for Case 6 - 3 blade fan

As considered in Chapter 1 (see Table 1-1), since the BPFs are small (less than 50 Hz) for the three blade fan, most of the harmonic integer multiples of BPF are less than 200 Hz. Cases 2-6 indicated the same pattern at a fixed frequency irrespective of the RPM condition which was also seen in the 9 blade auto-spectral densities in Cases 4-6. For example, see the frequency range of 400-500 Hz in Figs. 3.22-24 and 3.30-33.

Sound pressure levels corresponding to different RPM conditions as a function of flow coefficient are presented in Fig. 3.35. It is evident that Case 3 is the noisiest case. Note that, the ordinate has started from the background SPL which is about 46 dB.

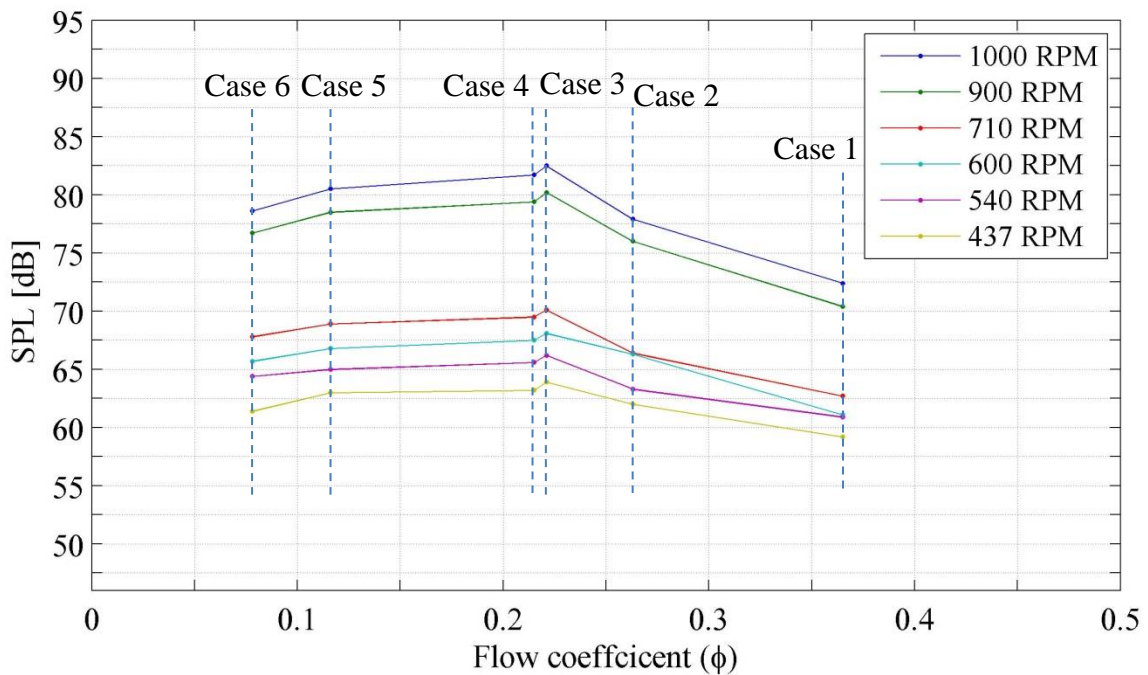


Figure 3-35 SPLs vs flow coefficient - 3 blade fan

### **3.4 Comparison between 9 and 3 blade fans**

Effects of passing through stall for a fixed RPM (i.e. 1000 RPM) has been investigated in Fig. 3.36 and Fig. 3.37 for nine and three blade fans respectively.

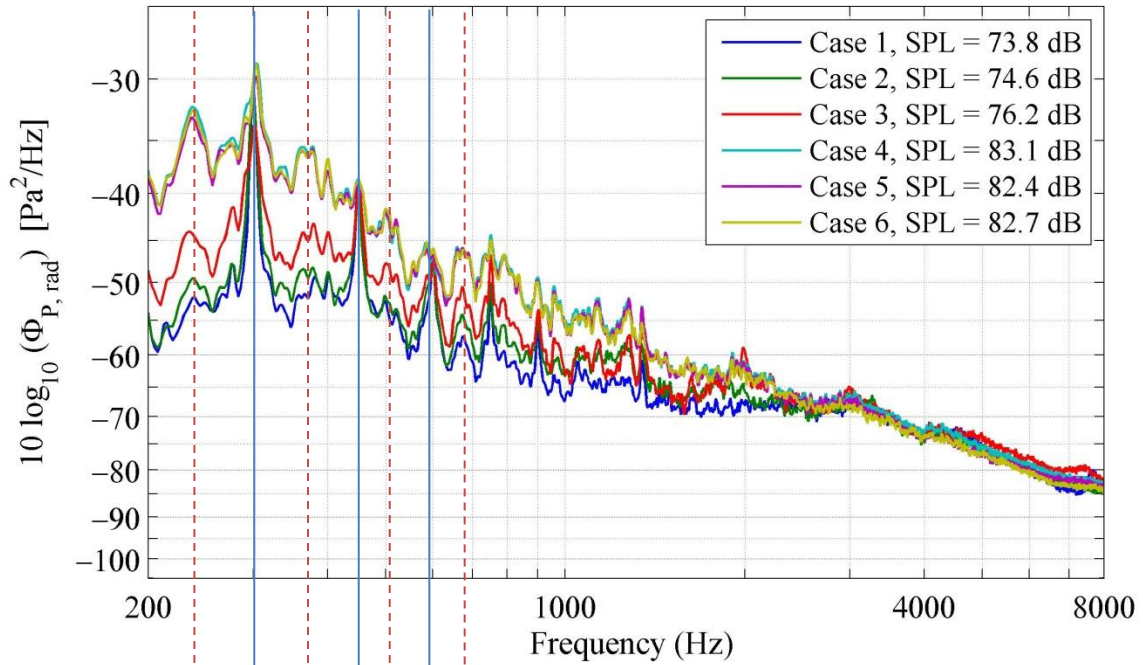


Figure 3-36 ASD for Case 1 through Case 6 at 1000 RPM - 9 blade fan

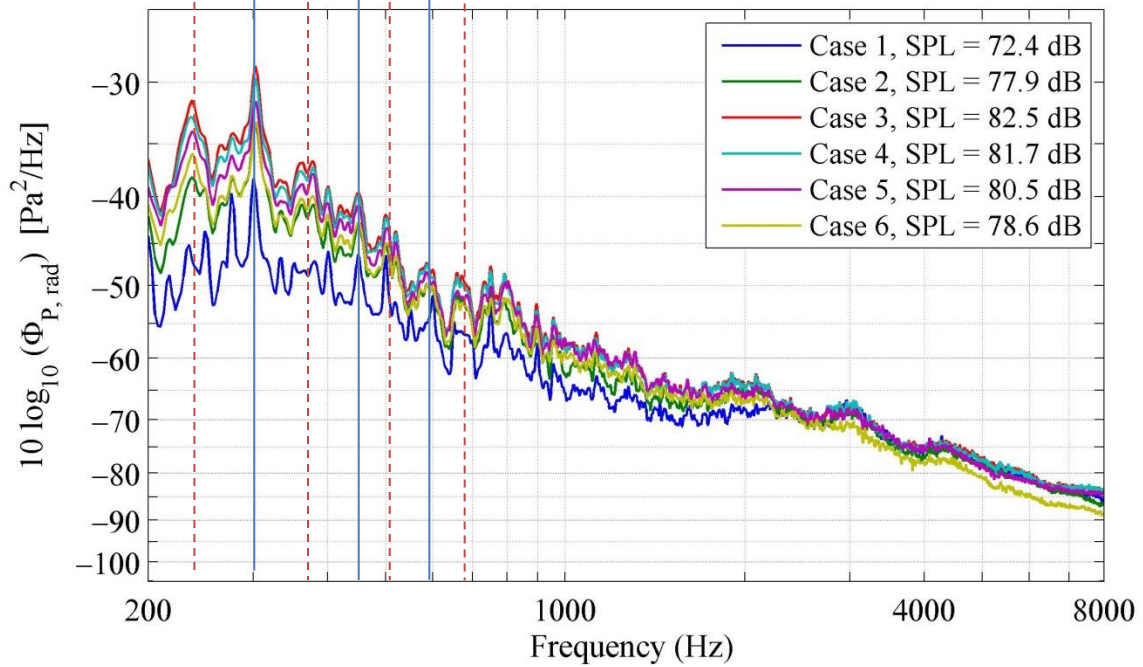


Figure 3-37 ASD for Case 1 through Case 6 at 1000 RPM - 3 blade fan

As indicated in Fig. 3.36, a considerable noise increase (overall 6.9 dB) occurred for the 9 blade fan associated with its passage through stall (passing from Case 3 to Case 4). However, for the 3 blade fan, the classic definition of stall does not apply from Case 3 to Case 4 as discussed in the presentation of the wake data (see Section 3.2.2). It is instructive that all of the largely separated flow (i. e. Cases 4-6 of the 9 blade fan and Cases 2-6 of the 3 blade fan) have the same pattern as shown in Fig. 3.36 and Fig. 3.37. That is, when the blade passes through stall, the non-rotating sound source becomes predominant (i. e. deeply separated flow). It is evident that in both the 3 and 9 blade configurations, the humps occur at the same frequency – shown by vertical red dashed lines.

It is quite instructive that for Cases 1-3 the BPF peaks have nominally the same magnitudes for the 9 blade fan (see 150, 300, 450 Hz – shown by solid blue vertical lines). It can be inferred that the rotating peaks which occur at discrete frequencies are independent of inflow condition. This observation is also in agreement with Cudina (2001) who indicated that the sound produced from aerodynamic loading would be the dominant contribution to the ASD in the stall condition. (The blade aerodynamic loading can be quantitatively evaluated with a stationary airfoil and the same approach velocity). Conversely, in the un-stalled condition, the BPF contributions would be the dominant contributor to the ASD. This observation is also obvious in Fig. 3.36. The humps between the BPF peaks are inferred to represent the non-rotating noise, and it is clear that their amplitudes increase as the blade is loaded (i.e. Case 1 through Case 3) – shown by vertical red dashed lines.

As stated by Quinlan (1998), flow unsteadiness associated with tip clearance flows is the primary source of high frequency noise. Kameier (1992) indicated that tip clearance effects are

independent of the rotor inlet flow conditions. Having examined various tip clearance configurations, he concluded that the inflow condition does not have substantial effect on the radiated sound of axial fans. The presented results for 9 and 3 blade fans in Figs. 3.23 and 3.24 are in agreement with Kameier (1992) and Quinlan (1998). Thus, it is suggested that the fan tip clearance causes the noise for  $f > 2400$  Hz .

### 3.5 Semi-empirical acoustic model results

#### 3.5.1 9 blade fan

In this section, the model proposed by Stephens and Morris (2011) for axial fan self-noise has been followed. Some changes and modifications have been made for the RCDB.

Blake's model was defined for a stationary airfoil exposed to a uniform free stream; however, it can also be used for a rotating airfoil if one applies Blake's model for an infinitesimal strip " $dr$ " at each radial location. The propagated noise is then recovered by an integration of the contributions from each strip. It is instructive to note that surface pressure spectra (proposed by Goody) are different for each radial location. Thus, Blake's equation can be written as:

$$[\Phi_{P_{rad}}(f)]_{non-compact} = \frac{1}{4\pi^2|r_{obs}|^2} \int_{r_{hub}}^{r_{tip}} (\Phi_{PP-SS}(f, r) + \Phi_{PP-PS}(f, r)) \Lambda_3(f) M_c(r) dr$$

$$f > \frac{c_0}{C} \quad (3.3)$$

$$[\Phi_{P_{rad}}(f)]_{compact} = \frac{fC}{16c_0|r_{obs}|^2} \int_{r_{hub}}^{r_{tip}} (\Phi_{PP-SS}(f, r) + \Phi_{PP-PS}(f, r)) \Lambda_3(f, r) M_c(r) dr$$

$$f < \frac{c_0}{C} \quad (3.4)$$

where,  $\Lambda_3(f, r) = W_\infty(r)/2\pi f$ .  $\Phi_{PP-SS}(f, r)$ ,  $\Phi_{PP-PS}(f, r)$  and  $M_c(r)$  are the suction side, pressure side surface pressure spectra, and convective Mach number for each radial location respectively.  $r_{obs}$  is the distance of an observer with respect to the trailing edge. In this study, the radiated pressure has been measured at two different elevations (i.e. lower and upper circle array) and averaged between each pair of microphones. Thus, an average distance between two arrays has been used in the semi-empirical model.

Stephens and Morris (2011) used the wake thickness as an approximation to the boundary layer thickness in their model. They assumed that the wake thickness at each radial location is the circumferential distance between the points where the RMS of velocity fluctuations was corresponding to half of the peak value. They also indicated that they used the same parameters (i.e. wake thickness) for both pressure and suction sides. The latter can be a rough approximation. In this study, two separate approximations have been obtained for suction and pressure side boundary layers. That is, the suction side boundary layer is defined as the circumferential distance between points where the RMS velocity fluctuations peak and half of its value in the suction side are subtracted by half of the trailing edge thickness. Similarly, the pressure side boundary layer is defined using the pressure side of the wake pattern. Note that the trailing edge thickness is about 1.5 mm.

The wake patterns for the second blade have been shown in Figs. 3.38-42. Based on the defined method, wake thickness approximations can be obtained for Cases 1, 2 and 3 in the 9 blade fan as noted in the following figures.

Wake thickness approximations for both suction and pressure side are provided in Table 3-3.

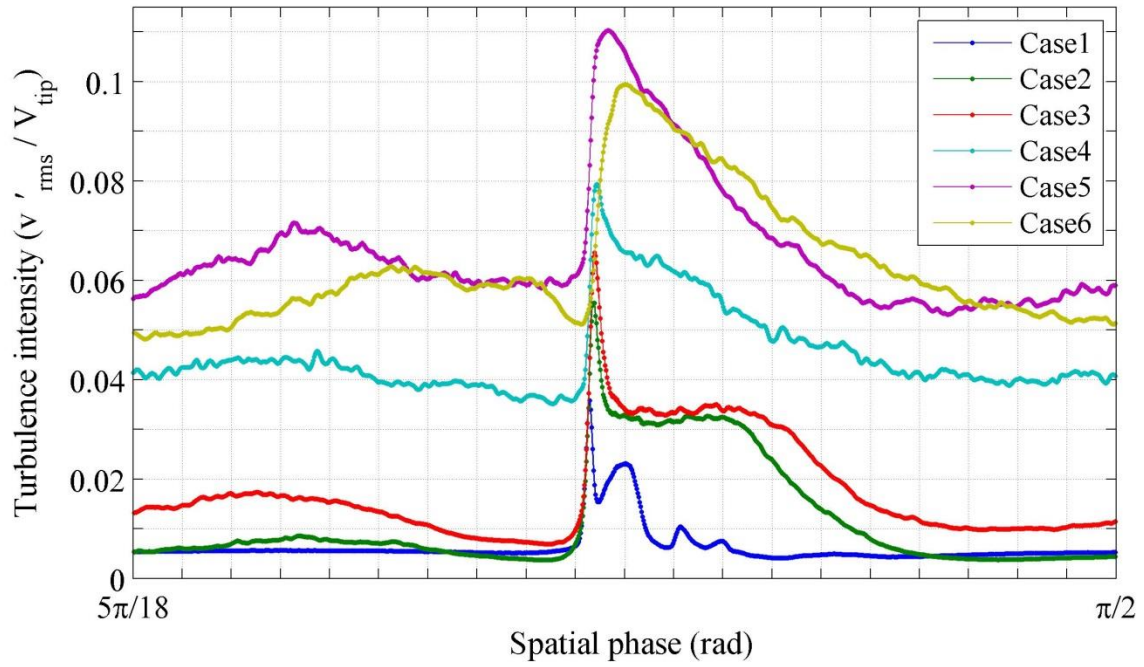


Figure 3-38 Turbulence intensity of the second blade wake region,  $r/r_{tip} = 0.707$  - 9 blade fan

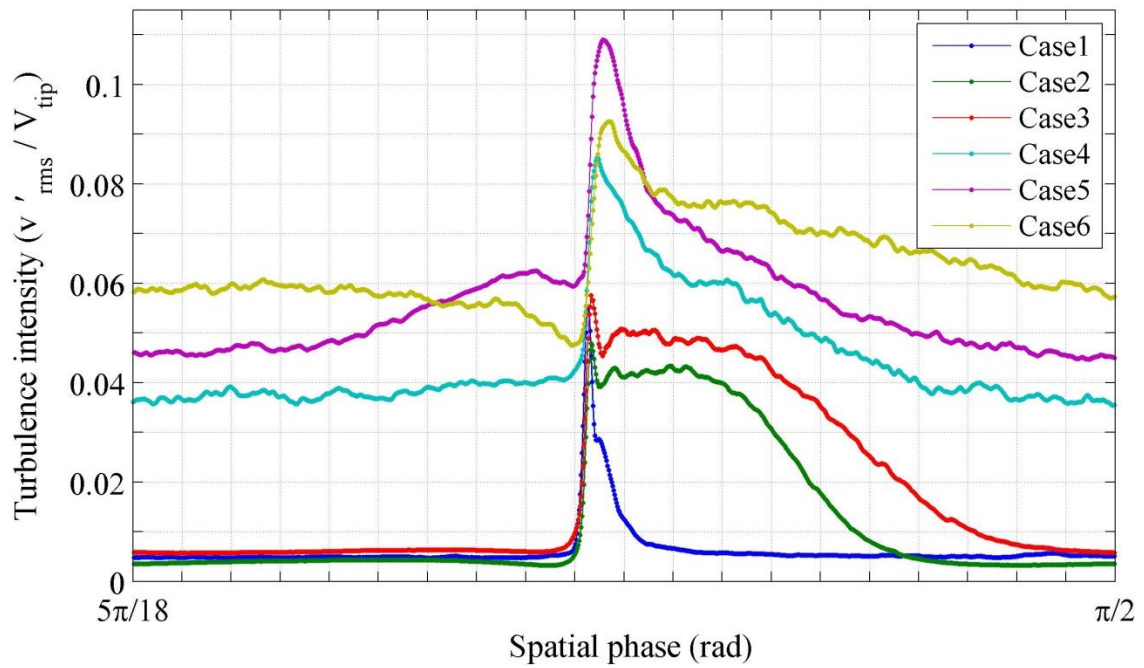


Figure 3-39 Turbulence intensity of the second blade wake region,  $r/r_{tip} = 0.77$  - 9 blade fan

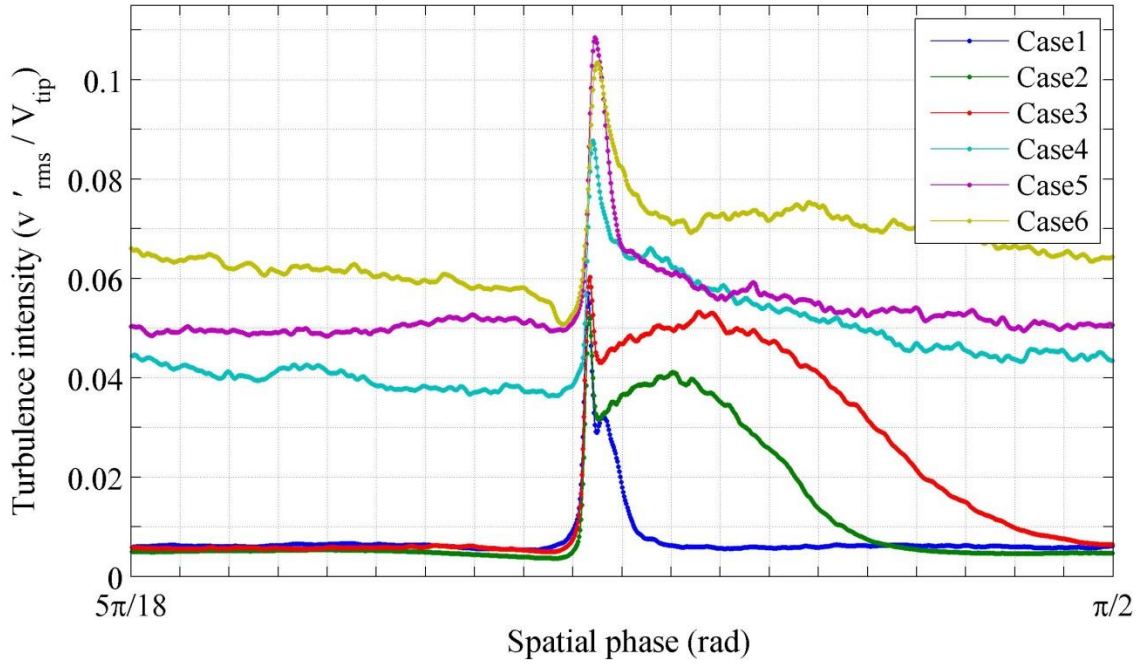


Figure 3-40 Turbulence intensity of the second blade wake region,  $r/r_{tip} = 0.83$  - 9 blade fan

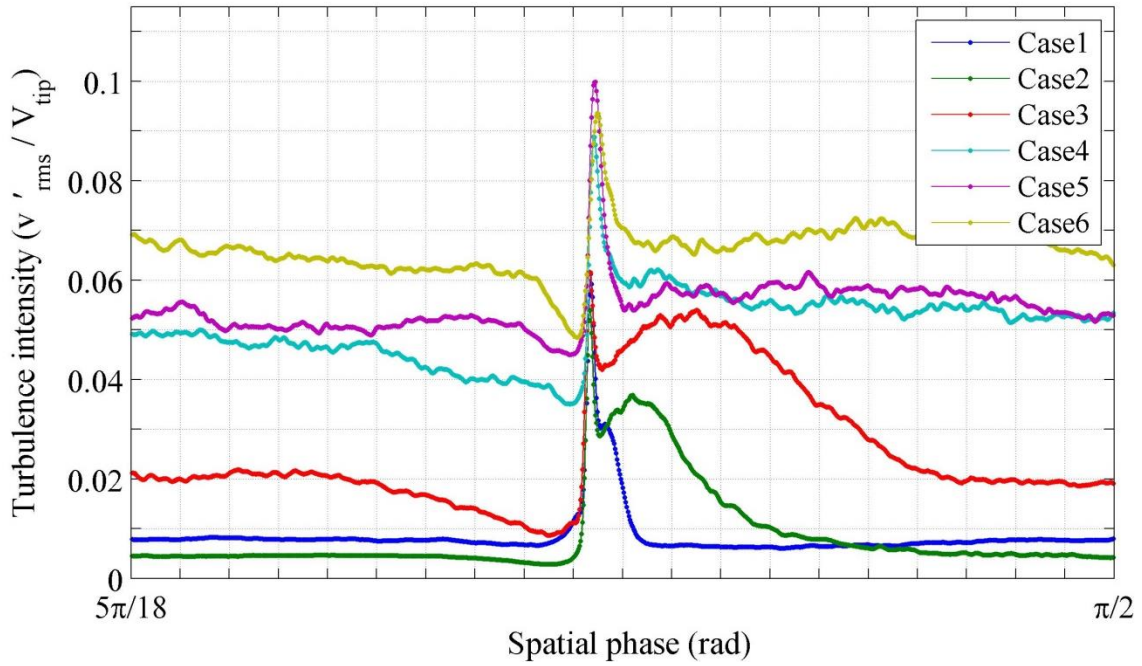


Figure 3-41 Turbulence intensity of the second blade wake region,  $r/r_{tip} = 0.89$  - 9 blade fan

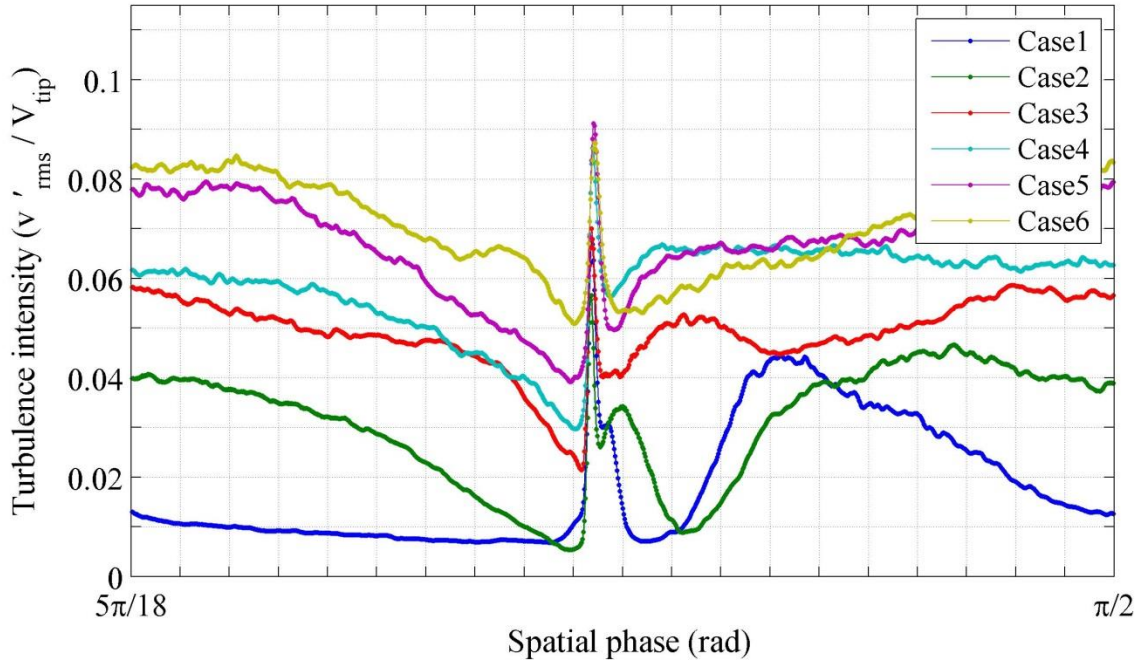


Figure 3-42 Turbulence intensity of the second blade wake region,  $r/r_{tip} = 0.96$  - 9 blade fan

Table 3-3 Wake thickness approximations – 9 blade fan

		$\frac{r}{r_{tip}} = 0.707$		$\frac{r}{r_{tip}} = 0.77$		$\frac{r}{r_{tip}} = 0.83$		$\frac{r}{r_{tip}} = 0.89$		$\frac{r}{r_{tip}} = 0.96$	
		SS	PS	SS	PS	SS	PS	SS	PS	SS	PS
9 blade	Case 1	3.5	0.3	2.6	0.5	4.7	0.5	4.1	0.5	3.8	0.4
	Case 2	35	0.8	42.5	0.5	37.5	0.5	18.1	0.4	0.8	0.4
	Case 3	35.7	0.8	44.3	0.5	60.2	0.5	55.3	0.5	55.3	0.4

As noted in Table 3-3, the approximated pressure side wake thicknesses are much smaller than those of the suction side. It is inferred that the pressure side wake thickness can be an accurate approximation to the pressure side boundary layer. It is also noted that the wake

thickness at the fifth radial location on the suction side has been assumed equivalent to that of the fourth location since the wake thickness could not be obtained, because the disturbed flow of the wake has merged with the disturbed flow of the tip leakage.

Figs. 3.43-45 show the semi-empirical results compared to the corresponding experiments for Cases 1, 2 and 3 of the 9 blade fan.

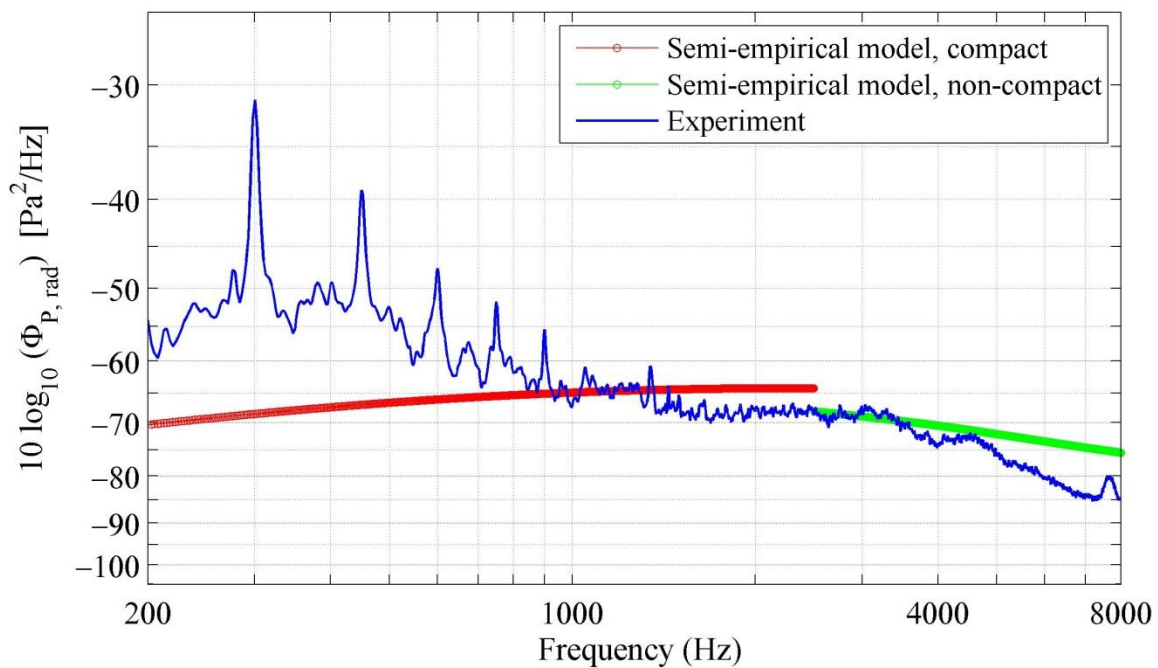


**Figure 3-43 Semi-empirical results vs experiment, Case 1- 9 blade fan**

The non-compact part of the predicted spectrum ( $f > 2500$ ) is in good agreement with the experiment. However, there is a significant discrepancy in the compact part ( $f < 2500$ ). This comparison indicates that the semi-empirical model has an accurate prediction for the non-compact part. 10 dB is the maximum difference seen in the non-compact part.

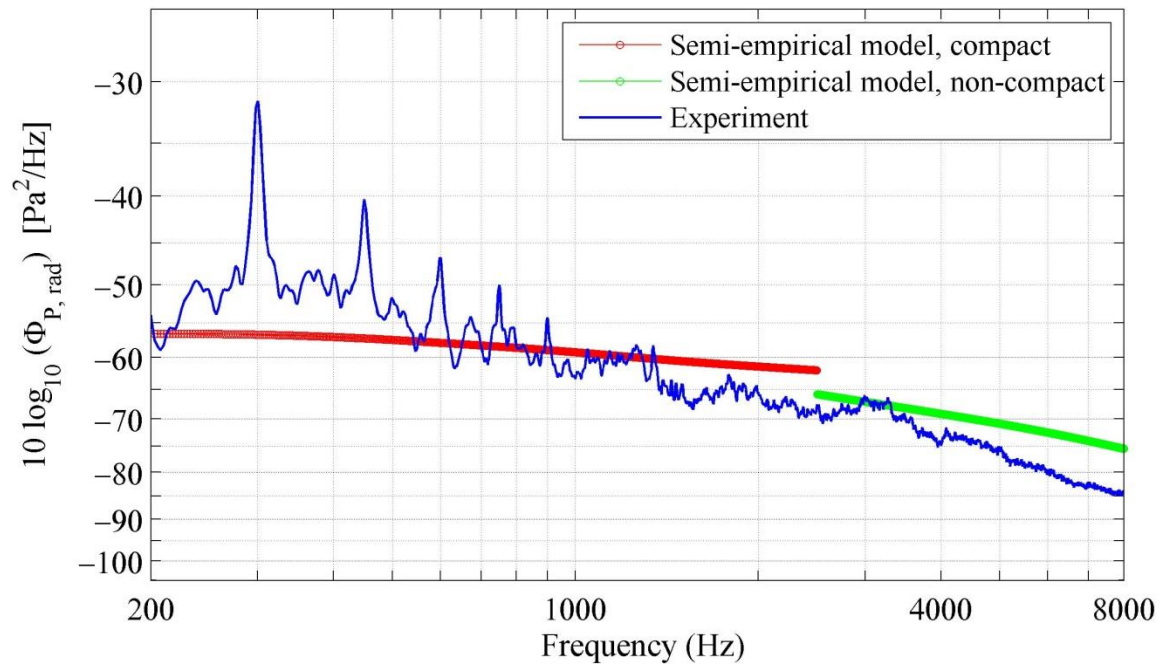


Figure 3-44 Semi-empirical results vs experiment, Case 2 - 9 blade fan

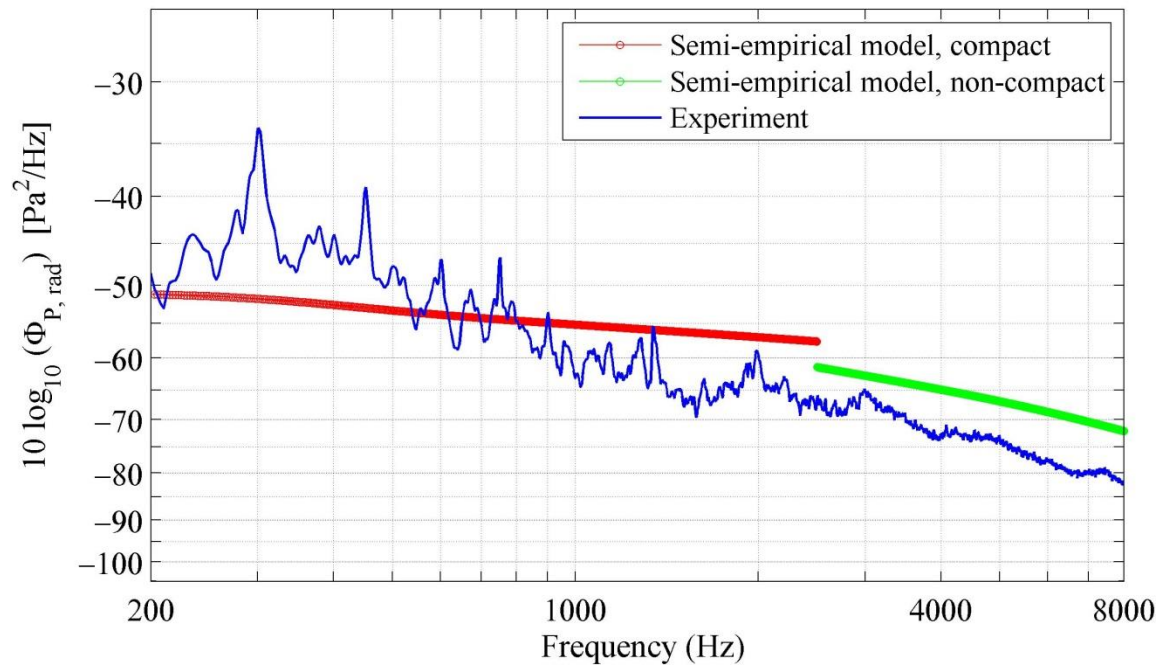


Figure 3-45 Semi-empirical results vs experiment, Case 3 - 9 blade fan

Figs. 3.44 and 3.45 provide a closer prediction for broad band noise spectra for both the compact and non-compact part.

### 3.5.2 3 blade fan

The same predictions have been carried out for Case 1 of the 3 blade fan. Fig. 3.31 indicates the wake turbulence intensity for Case 1. From this figure, wake thickness approximations have been obtained and presented in Table 3-4.

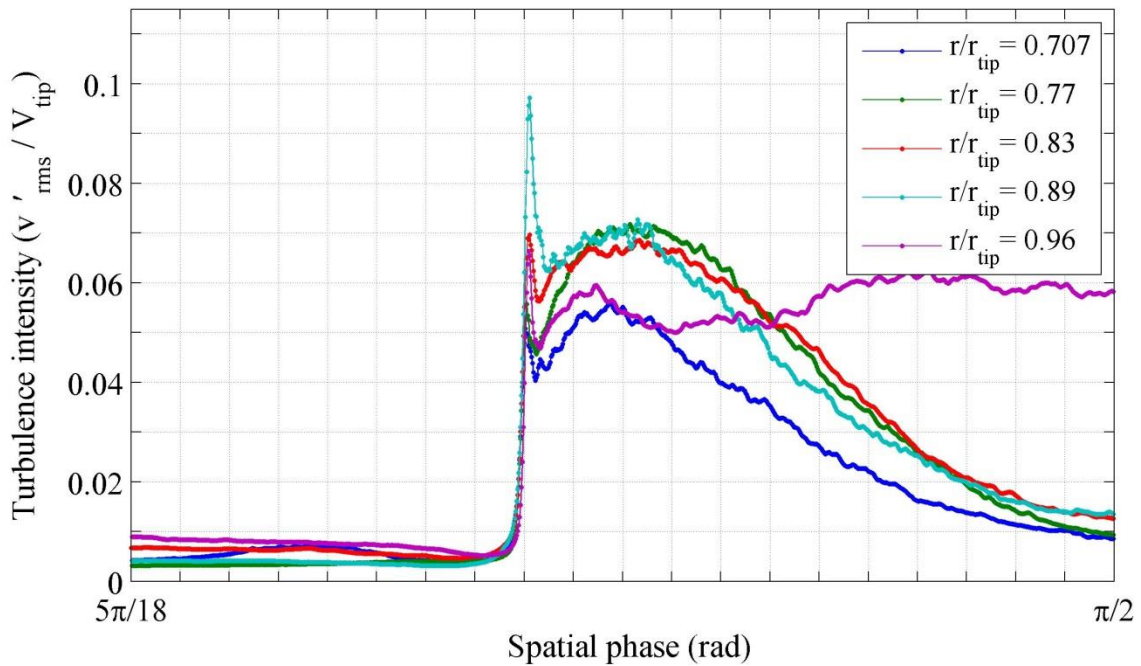
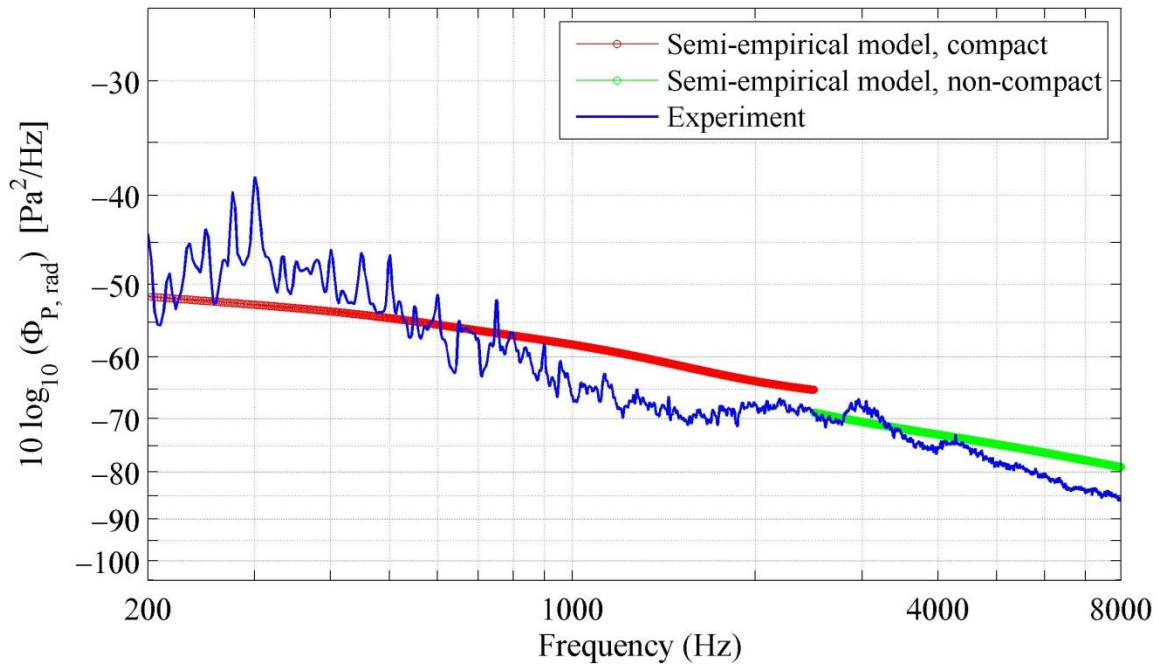


Figure 3-46 Turbulence intensity in the wake region of the first blade, Cases 1 - 3 blade fan

**Table 3-4 Wake thickness approximations - 3 blade fan**

		$\frac{r}{r_{tip}} = 0.707$		$\frac{r}{r_{tip}} = 0.77$		$\frac{r}{r_{tip}} = 0.83$		$\frac{r}{r_{tip}} = 0.89$		$\frac{r}{r_{tip}} = 0.96$	
		SS	PS	SS	PS	SS	PS	SS	PS	SS	PS
3 blade	Case 1	66.9	0.5	81.3	0.8	73.8	1.1	49.0	0.8	49.0	0.4

A comparison of the semi-empirical model and the experimental results for the 3 blade fan is shown in Fig. 3.47.



**Figure 3-47 Semi-empirical results vs experiment, Cases 1- 3 blade fan**

As noted, the semi-empirical model results and the experiment are in good agreement for both the compact and non-compact part.

The semi-empirical model indeed incorporated many approximations and assumptions, however, the results were found to be in reasonable agreement with the experiments as shown in

this study and by Stephens and Morris (2011). Using the semi-empirical model as a reference, one can determine other experimental factors involved in axial fan noise generation that have not been considered in the model.

## 4 SUMMARY AND CONCLUSIONS

Aeroacoustic and wake characteristics of the Rotating Controlled Diffusion Blades (RCDBs) configured as a 3 and a 9 blade fan were explored. Six cases were identified for three blade configuration based on its performance curve and their corresponding flow physics were examined. Also, six cases for nine blade configuration corresponding to six distinct operating conditions: i) an attached flow, ii) a slightly separated flow, iii) a deeply separated flow and three cases in the stall region were selected. For each case, hot-wire anemometry downstream of the fan and aeroacoustic measurements above the fan plane (upstream of the fan) were made. Fundamental flow characteristics in the wake region were examined by obtaining phase averaged mean velocity and turbulence intensity downstream of the fan. Aeroacoustic measurements were obtained using inexpensive Panasonic microphones arranged in two arrays at two different elevations above the mid-span of the blades. Panasonic microphones were properly calibrated versus a “Master” Larson Davis microphone (the reference microphone) in the range of 200-8000 Hz. A beamforming technique was employed to properly measure the radiated acoustic pressure in a non-anechoic environment. The following conclusions are supported by the results presented in the preceding sections:

- a) The 3 blade fan was found to have a separated flow over the entire span of the blades even for almost zero pressure rise. The classic definition of fan stall does not apply for this configuration since the blades are widely separated. Unlike the nine blade configuration, the three blade fan stagger angles are understood to be responsible for these separated conditions.

- b) Axial fan noise can be classified as rotating and non-rotating self-noise. The rotating self-noise is generated by the rotation of the fan blades. The non-rotating self-noise is generated by the aerodynamic loading of the blades.
- c) It was determined that rotating noise (i. e. blade passing frequency noise) is predominant for the higher flow rates when the aerodynamic loading on the blades is not significant (i.e. Case 1 and Case 2 of the 9 blade fan).
- d) In Case 3 of the 9 blade fan, the rotating noise and non-rotating noise (the latter due to the aerodynamic loading condition that can be quantitatively evaluated with a stationary airfoil and the same approach velocity) are almost balanced.
- e) It was observed that the rotational noise does not depend on the inflow conditions (i.e. Reynolds number), and it is almost a function of rotational velocity.
- f) Transition from Case 3 to Case 4 for the 9 blade fan corresponds to a significant noise increase and turbulence intensity elevation. In Case 4, the non-rotating noise dominates the rotating noise, and an abrupt pressure drop across the fan occurs.
- g) It was observed that high frequency noise of the fan ( $f > 2400 \text{ Hz}$ ) is not sensitive to the inflow conditions and, based on the literature review, the tip clearance noise is understood to generate the high frequency noise.
- h) It was observed that stall noise (that is, a non-rotating self-noise) spectra trends are quite similar irrespective to the blade configurations, RPM conditions and inflow conditions.
- i) Semi-empirical acoustic models for TBL-TE noise can be adopted to predict axial fans radiated sound. Hot-wire data can be used as experimental input for these models. Comparisons between experimental results and the semi-empirical model can be an instructive technique to estimate the magnitude of the expected ASD. Using the semi-

empirical models as a reference, an investigator can determine other experimental factors involved in axial fan noise generation that have not been considered in the models.

## APPENDICES

## Appendix A: Signal processing

The formula of this section was taken from Bendat and Piersol (1986). Consider random signals “a” and “b” including “M” data points.

On-sided auto spectral density follows as:

$$\Phi_{aa} = \frac{2 \times f_s}{n_d \times M} \times \sum_{i=1}^{nd} \left| FFT(a) \times w(M) \times \sqrt{\frac{8}{3}} \right|^2 \quad (A.1)$$

where,  $FFT(a)$  is the fast Fourier transform algorithm applied on signal a,  $f_s$  is the sampling frequency,  $n_d$  is the number of blocks data for ensemble averaging,  $w(M)$  is the Hanning tapering, and  $\sqrt{\frac{8}{3}}$  is a scale factor to compensate the loss caused by the Hanning tapering.

On-sided cross spectral density follows as:

$$\Phi_{ab} = \frac{2 \times f_s}{nd \times M} \times \sum_{i=1}^{nd} FFT(a)^* \times w(M) \times \sqrt{\frac{8}{3}} \times FFT(b) \times W(M) \times \sqrt{\frac{8}{3}} \quad A.2$$

where,  $FFT(a)^*$  is the conjugate of the  $FFT(a)$ .

The unbiased cross correlations between random signals “a” and “b” at lag numbers  $N_d = 0, 1, 2, \dots$  with  $N_d < N$  is defined as:

$$R_{ab} \left( \frac{N_d}{f_s} \right) = \frac{1}{N - N_d} \sum_{j=1}^{N-N_d} a_j a_{j+N_d} \quad A.3$$

## Appendix B: Convergence

Convergence evaluations have been carried out for both wake and acoustic data to make certain that the statistics are converged in the 95 seconds duration of data acquisition. As an example, the convergence evaluation for wake data has been presented in Fig. B.1. For the wake data, convergence is defined as:

$$Convergence = \frac{1}{2\pi} \int_{\theta=0}^{\theta=2\pi} \left[ \frac{\sum_{i=1}^N V_i(\theta)}{N} - \langle V(\theta) \rangle \right] d\theta \times 100 \quad B.1$$

where, N is the number of fan revolutions, and  $\theta$  is the spatial phase. The convergence evaluation demonstrates that after N number of revolutions, how close the obtained mean velocity is to the final mean value. As will be noted in Fig. B.1, the statistics have been converged quite sooner in Case1 which represents an attached flow. Obviously, a longer time is needed for a separated flow (i. e., Case 4 and 5) to be converged. It can be noted that after approximately 1000 revolutions, all of the cases have reached to 99% percent of the final mean velocity.

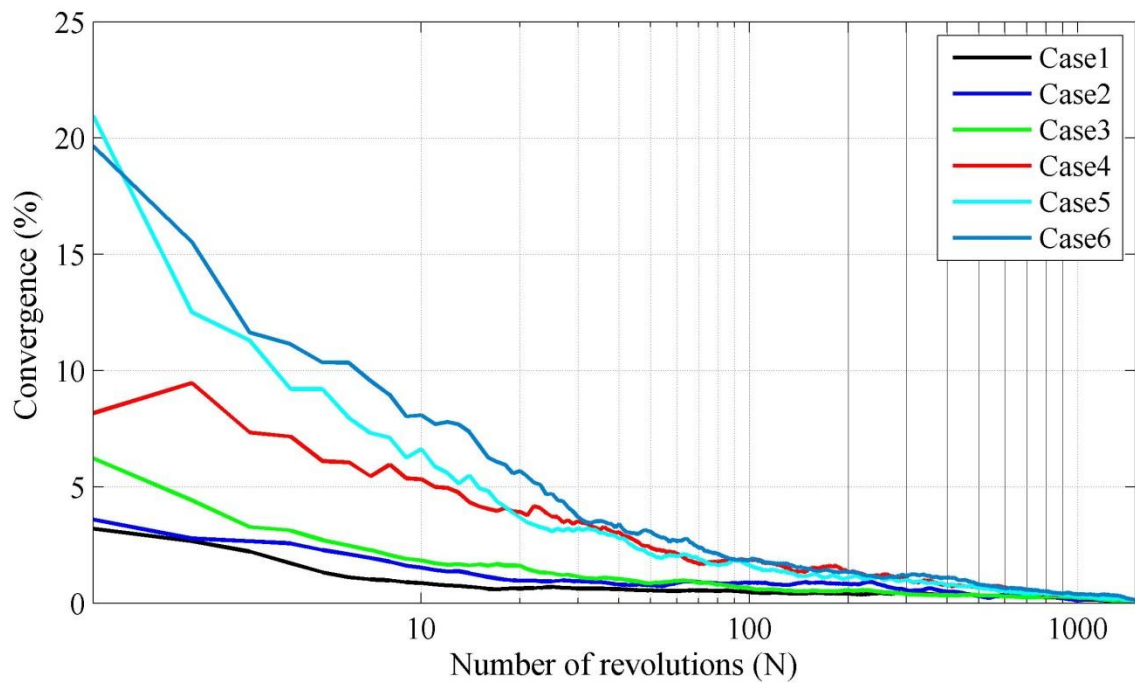


**Figure B-1 Convergence history of  $\langle V(\theta) \rangle$  at 1000 RPM - 9 blade fan**

## Appendix C: Fan “laws”

During data acquisition, the fan rotational velocity can slightly deviate from the target value. This deviation would also affect other corresponding measurements such as pressure rise and mass flow rate across the fan. Jorgensen (1961) has provided fan “laws” that can be used to scale the measured values (shown by index “m”) to the target values (shown by index “t”).

$$\frac{\dot{m}_t}{\dot{m}_m} = \frac{\Omega_t}{\Omega_m} \quad C. 2$$

$$\frac{\Delta P_t}{\Delta P_m} = \left( \frac{\Omega_t}{\Omega_m} \right)^2 \quad C. 3$$

### Appendix D: Ambient noise concern

Six distinct representatives of ambient noise were obtained on six different days. The spectra are presented in Fig. D.1. During these data acquisition sessions, the objective was to acquire data in a relatively quiet environment. Specifically, these periods occurred at nights when the laboratory air conditioning facilities were inactive. The sound pressure levels (SPL) were about 46 dB which still generally indicates a noisy environment. Note that, the AC electrical equipment exhibit discrete peaks at 240, 300 and 360 Hz in auto spectral density, and higher harmonics of 60 Hz will be almost attenuated after 360 Hz.

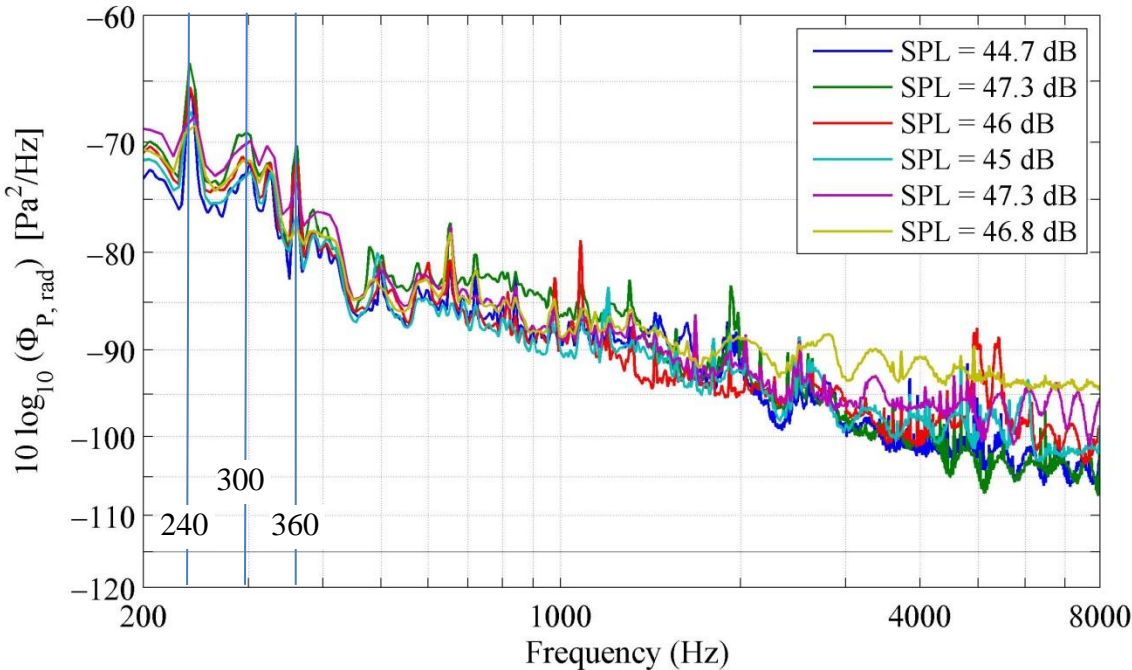


Figure D-1 Lab ambient noise

Recorded noise at low RPM conditions ( $< 600 \text{ RPM}$ ) especially in Case 1 and Case 2 might be affected by ambient noise; however, higher RPM conditions quite stand above the ambient noise, and the background noise effect can be neglected. It is noteworthy to mention that using

the beamforming technique the background noise has been significantly attenuated in the data processing.

## Appendix E: Microphones technical specifications

### E. 1 Larson Davis technical specification

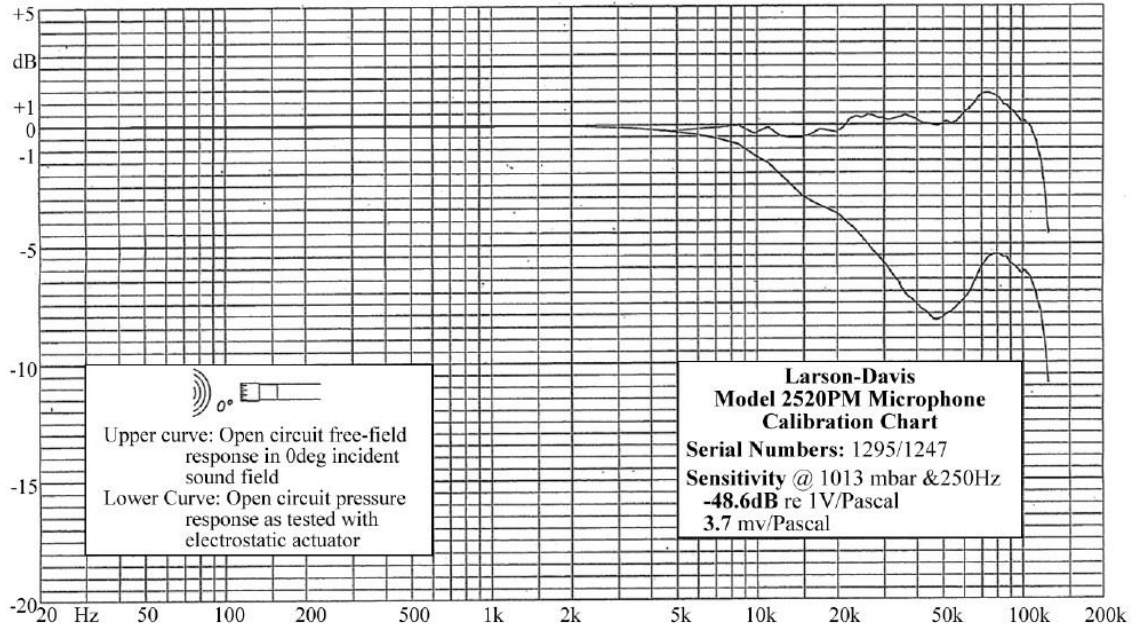


Figure E-1 Larson Davis manufacture specifications

## E. 2 Panasonic microphone technical specification

### Panasonic

### Microphone Cartridges

#### Omnidirectional Back Electret Condenser Microphone Cartridge

Series: **WM-64C/64K**  
**WM-64BC/64BK** (pin type)



#### ■ Features

- Very small, thin type omnidirectional microphone
- Most suited to products having limited space
- Back electret type designed for high resistance to vibrations
- Better shielded, RF noise-resistant type

#### ■ Recommended Applications

- WM-64C (33 pF)— GSM, PDC, etc.
- WM-64K (10 pF)— DEC T, PHS, PC N, PCS, etc.
- WM-64BC (33 pF)— GSM, PDC, etc. (pin type)
- WM-64BK (10 pF)— DEC T, PHS, PC N, PCS, etc. (pin type)

#### ■ Sensitivity

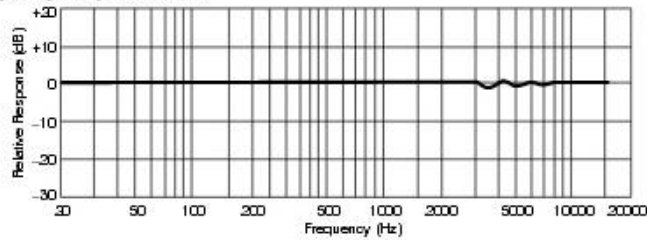
$V_s = 2.0V$   
 $R_L = 2.2k\Omega$

$-45 \pm 4dB$   
 (X:  $-46 \pm 3dB$ )  
 (T:  $-44 \pm 3dB$ )

#### ■ Specifications

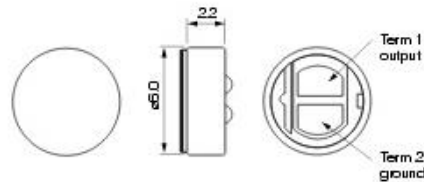
Sensitivity	$-45 \pm 4dB$ (0dB = 1V/Pa, 1kHz)
Impedance	Less than 2.2 k $\Omega$
Directivity	Omnidirectional
Frequency	20–16,000 Hz
Max. operation voltage	10V
Standard operation voltage	2V
Current consumption	Max. 0.5 mA
Sensitivity reduction	Within $-3dB$ at 1.5V
S/N ratio	More than 58 dB

#### ■ Typical Frequency Response Curve

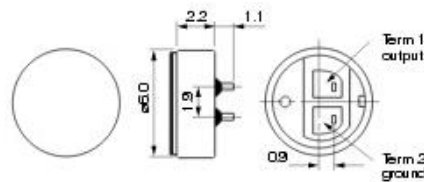


#### ■ Dimensions in mm (not to scale)

WM-64C/64K



WM-64BC/64BK



Design and specifications are subject to change without notice. Ask factory for technical specifications before purchase and/or use. Whenever a doubt about safety arises from this product, please contact us immediately for technical consultation.

Figure E-2 Panasonic manufacture specifications

## REFERENCES

## REFERENCES

- BENDAT, J. S., PIERSOL, A. G. 1986. *Random Data: Analysis and Measurement Procedures*. John Wiley and Sons, Inc., New York.
- BLAKE. W. K. 1986. *Mechanics of Flow-induced Sound and Vibration (two volumes)*. Academic Press Inc., New York, USA.
- BROOKS, T. F. & MARCOLINI, M. A. 1986. Airfoil Tip Vortex Formation Noise. *AIAA*, **24**(2), 246-252.
- BROOKS, T. F., STUART, D., AND MARCOLINI, A. 1989. Airfoil self-noise and prediction. *NASA Reference Publication*, 1218.
- CAWOOD, A. F. 2012. *Surface pressure measurements on a rotating controlled diffusion blade*. Master Thesis. Michigan State University.
- CUDINA, M. 2001. Noise generation in vane axial fans due to rotating stall and surge. *Journal of Mechanical Engineering Science*, **215** (57), 57-64.
- Curle, N. 1955. The influence of solid boundaries upon aerodynamic sound. *Proc. R. Soc. London A* 231, 505-514.
- Ffowcs Williams J. E. & Hawkings D. L. 1969, Sound generation by turbulence and surfaces in arbitrary motion. *Phil. Trans. R. Soc. London A*264. 321–342.
- FINK, M. R. & BAILEY, D. A. 1980. Airframe Noise Reduction Studies and Clean-Airframe Noise Investigation. *NASA*, CR-159311.
- GELDER, T.F., SCHMIDT, J.F., SUDER, K.L., & HATHAWAY, M.D. 1987. Design and performance of controlled-diffusion stator compared with original double circular arc stator. *Tech. rept. NASA*.
- GOODY, M. 2004. Empirical spectral model of surface pressure fluctuations. *AIAA Journal*, **42** (09), 1788-1794.
- GROSVELD, F. W. 1985. Prediction of Broadband Noise From Horizontal Axis Wind Turbines. *AIAA J. Propuls. and Power*, **1**(4). 292-299.
- HUBBARD, H. H, & SHEPHERD, K. P. 1991. Aeroacoustics of large wind turbines. *The Journal of the Acoustical Society of America*, **89**, 2495.

- ILIE, M. 2009. Numerical study of helicopter blade–vortex mechanism of interaction using large-eddy simulation. *Journal of Computers and Structures*, **87**, 758–768.
- JOEGENSEN, R. 1961. *Fan Engineering*, Buffalo Forge Company, Buffalo, New York, USA.
- KAMEIER, F., NAWROT, T., AND NEISE, W. 1992. Experimental Investigation of Tip Clearance Noise in Axial Flow Machines, *AIAA Aeracoustics Conference Aachen*, **14**, 250-259
- KHALIGHI, Y. 2010. *Computational aeroacoustics of complex flows at low Mach number*. PhD Dissertation. Stanford University.
- LEITE, R. P., PAUL, S., GERGES, S. N.Y. 2009. A sound quality-based investigation of the HVAC system noise of an automobile model, *Journal of Applied Acoustics*, **70**, 636-645.
- Lighthill, M. J. 1952. On sound generated aerodynamically. Part I: General theory. *Proc. R. Soc. London A211*, 564–587.
- LISSAMAN, P.B.S. 1983. Low-Reynolds-number airfoils. *Annual Review of Fluid Mechanics*, **15**(1), 223-239.
- LONGHOUSE, R. E. 1976. Vortex shedding noise of flow tip speed, axial flow fans. *Journal of Sound and Vibration*, **53**(1), 25-46.
- MORRIS, S.C., & FOSS, J.F. 2001. An aerodynamic shroud for automotive cooling fans. *Journal of Fluids Engineering*, **123**, 287.
- MORRIS, S. C. & SHANNON, D. W. 2007. Experimental measurements of sound generated by automobile side-view mirrors. *Tech. Rep. UND-SM07-330*. Hessert Laboratory for Aerospace Research, University of Notre Dame.
- NEAL, D. R. 2010. *The Effect of rotation on the flow field over a controlled-diffusion airfoil*. PhD Dissertation. Michigan State University.
- PATERSON, R. W. & AMIET, ROY K. & MUNCH, C. L. 1974 (Jan.- Feb.). Isolated Airfoil-Tip Vortex Interaction Noise, *AIAA Journal*, Paper No. 74-194.
- QUINLAN D. A & BENT P. H. 1998. High frequency noise generation in small axial flow fans. *Journal of Sound and Vibration*, **218**(8), 177–204.

- RUSSELL, D.A., TITLOW, J.P., BEMMEN. 1999. Acoustic monopoles, dipoles and quadrupoles: An experiment revisited. *American Journal of Physics* ,**67** (8).
- SPALART P, R & WATMUFF, J. H. 1993. Experimental and numerical study of a turbulent boundary layer with pressure gradients. *Journal of Fluid Mechanics*, **249**, 337–371.
- STEPHANS D., & MORRIS, S. 2011 Measurements and modeling of the self-noise of a low-speed ducted rotor, *International Journal of Aeroacoustics*, **10** (5&6), 613-633.